Pattern and Polarization Reconfigurable Antennas for Gain Enhancement

The University Of Sheffield.

Beyit Barakali

Department of Electronic and Electrical Engineering

University of Sheffield

This thesis is submitted for the degree of

Doctor of Philosophy

July 2019

I would like to dedicate this thesis to my loving family ...

Declaration

I hereby declare that except where specific reference is made to the work of others, the contents of this dissertation are original and have not been submitted in whole or in part for consideration for any other degree or qualification in this, or any other University. This dissertation is the result of my own work and includes nothing which is the outcome of work done in collaboration, except where specifically indicated in the text. This dissertation contains less than 65,000 words including appendices, bibliography, footnotes, tables and equations and has less than 150 figures.

Beyit Barakali

July 2019

Acknowledgements

I would like to acknowledge EPSRC(Engineering and Physical Sciences Research Council) for funding this project.

I would like to specially thank my supervisor Dr K.L. Ford for his great supervision and valuable insight as well as being supportive when needed.

I would also like to thank my second marker Dr Salam Khamas for his kindly attitude and advices during the course of this project.

And finally I would like to thank to my family and friends for being supportive throughout my PhD and never lost the faith in me.

Abstract

Since the rapid proliferation of the wireless communication systems, the effective use of the allocated spectrum has become vital. The desire for generating equipment that can adopt their characteristics for different and challenging environments where excessive interference and mobile traffic is present has been increased. Pattern reconfigurable antennas have been an ideal candidate with conformal radiating characteristics, low cost and low power consumption features. A pattern reconfigurable dipole antenna placed over a ground plane with parasitic reflectors for continuous beam control has been considered as a starting point of the project where the well known Fabry Pérot resonance modes were utilized. The model was designed to be operating within $1.8GHz$ frequency band of current wireless communication systems. The continuous beam steering over the azimuth plane has been achieved by manipulating the surface currents along the parasitic strips by varying the capacitance between the conducting strips of the elements. Furthermore, a partially reflecting surface formed of periodic dipoles, was allocated on top of a metallic ground and the radiating structure formed of a half wavelength dipole and two parasitic strips for further gain enhancement and pattern reconfigurability. PIN diodes have been biased to switch between "ON" and "OFF" states and achieve beam switching from a high gain boresight direction to endfire radiation along the azimuth. Latterly the dual polarised version of the model was evaluated for an extra step of freedom where the operating frequency has been increased up to $3.6GHz$ which will be within the predicted frequency bands of next generation communication systems. Two orthogonally positioned dipole antennas with single parasitic elements have been used as the radiating structure. A total of four PIN diodes have been initialized for achieving pattern reconfiguration in both polarizations where the beam is switched from boresight to endfire directions. The evaluation process of three different models supported with, current curves and polar plots have been extensively studied in the thesis. Prototypes have been generated for each model and tested in a fully anechoic chamber for the proof and validation of the theory and simulation results.

Publications

- High-gain pattern reconfigurable micro-strip dipole antenna with a gain enhancing partially reflecting surface (IET Microwaves, Antennas and Propagation, 15 August 2018, Vol.12(10), pp.1679-1683 [Peer Reviewed Journal]) Co-Authors: Kenneth L Ford, Salam Khamas
- A Pattern Reconfigurable Microstrip Dipole Antenna with PRS Gain Enhancement (2017 11th European Conference on Antennas and Propagation (EUCAP), Paris, 2017, pp. 3131-3134) Co-Authors: Kenneth L Ford, Salam Khamas

Table of contents

List of figures

List of tables

Nomenclature

Abbreviations

AUT	Antenna Under Test
LHS	Left hand side
MNZ	MU-near-zero
PEC	Perfectly electrical conductor
PRS	Partially reflecting surface
RHS	Right hand side
SIW	Substrate integrated waveguide
SRR	Split ring resonator
VNA	Vector Network Analyzer

List of Symbols

α	Angle of incidence
B_C	Susceptance
δ	Loss tangent

D	Directivity (dBi)
e_0	Total efficiency
e_c	Conduction efficiency
e_{cd}	Antenna radiation efficiency
e_d	Dielectric efficiency
ε_r	Relative Permittivity
e_r	Reflection efficiency
t_s	Substrate thickness
Γ	Reflection coefficient
h_c	Distance from the antenna
h_c	Cavity height
λ	Free space wavelength
N	An integer number
ω	Angular frequency
P_s	Parasitic strip separation
P_{in}	Input Power (W)
P_{rad}	Total radiated power (W)
ϕ_{GND}	Reflection phase of the ground plane
ψ	Reflection phase of the PRS

P_x	Unit cell periodicity x-direction
P_z	Unit cell periodicity z-direction
ρ	PRS reflection coefficient amplitute
Θ_1	Phase difference between direct and the first reflected wave within the cavity
U	Radiation Intensity ($W/unitsolidangle$)
$Wrad$	Radiation density (W/m^2)
X_L	Reactance
Z_{in}	Input impedance
Z_0	Characteristic impedance of free space
Z_0	Characteristic impedance
Z_d	Characteristic impedance of spacer material (FR4)

Chapter 1

Introduction

An age of wireless communication systems that have been predicted by many officials/authors with a consequence of rapid increase in the use of mobile communication networks over the few decades, where the proliferation of smart devices and applications have increased extensively brought up the future to our doorsteps [1, 2]. With the broad use of IoT (Internet of Things) the spectrum which is widely used by many applications has further congested with the rise of new technologies such as ultra high definition (UHD) realistic images and holograms containing huge bulks of data [2]. Therefore the capacity requirements for a channel should be enhanced in order to maintain the load effectively meanwhile improving the overall system performance and consuming low levels of energy. One of the approaches mentioned in [3], is to use ultra dense networks with large number of transmitter and receiver antennas in order to generate a high capacity infrastructure. The use of reconfigurable antennas with adaptive characteristics such as radiation pattern, polarization and frequency will have a substantial benefit on improving the performance of network systems. However compared to the conventional antennas with fixed purposes and applications, reconfigurable antennas can be implemented to create an intelligent system where the antennas can adapt their parameters for multiple purposes. With the use of pattern and polarization reconfigurable antennas, the beam direction and relative polarization can be varied, depending on the traffic within the electromagnetic spectrum. This will provide another degree of freedom to the

antenna in establishing a communication within the ultra dense network which can improve the use of spectrum, channel capacity and the range of coverage [4]. The implementation of reconfigurable antennas will lead to a decrease in the cost of developing an infrastructure with low complexity systems and low power consumption along with reducing the channel interference.

A high gain pattern and polarization reconfigurable antenna with a planar and low complexity structure is conducted in this project. The structure of interest can be implemented in the ultra dense networks to communicate with the neighbouring antennas placed on the sides of buildings/lamb-posts as illustrated in Figure 1.1. The ability to reconfigure the radiation pattern towards the boresight and enfire directions enables the communication with the adjacent antennas placed on the lamb posts as well as the base transceiver station located on the tall building. Most commonly used conventional approaches to achieve the beam steering

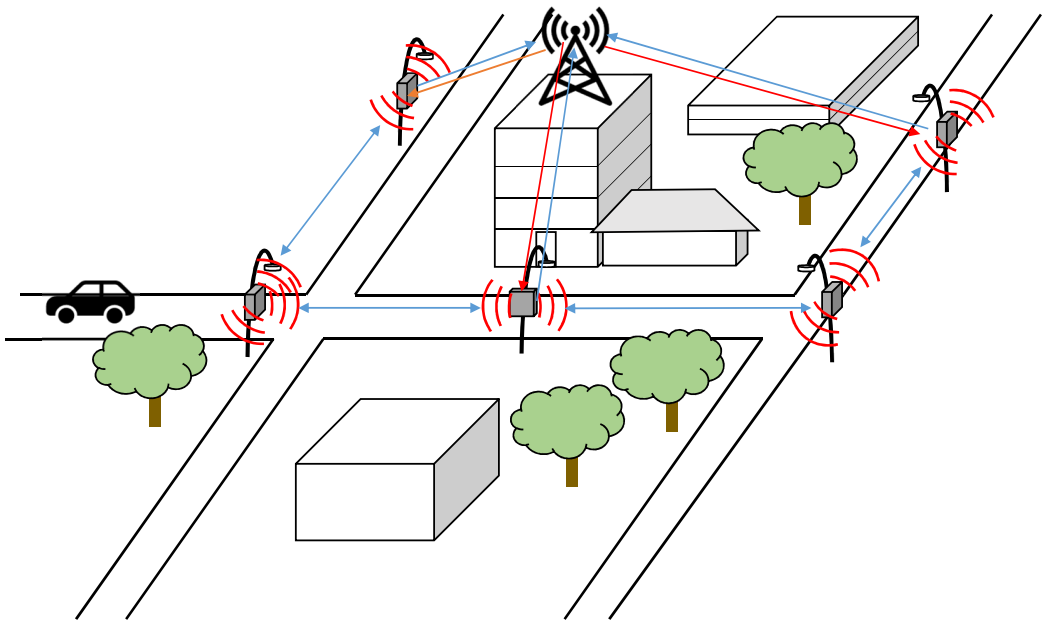

Fig. 1.1 A diagram illustrating the boresight to endfire switching antennas implemented on the lamp posts

property includes large amount of active components as well as phase shifters with circuitry which are high in complexity. Increasing the complexity of a system has a proportional effect on the manufacturing cost and power consumption under operation. The existence of radio frequency within the systems would result in faults of components which can be a time consuming process to detect and maintain resulting with inconvenience. Therefore the project has been based on a target of achieving pattern and polarization reconfigurability with minimum amount of active components and circuitry to prevent complications with comparably better results which will be extensively explained throughout the technical chapters 4, 5 and 6. Since the low complexity has been set as a keystone planar dipole antennas have been considered placed over a ground plane for boresight gain enhancement. The reconfigurability of the model has been introduced with the implementation of parasitic strips where the current flow have been altered affecting the overall radiation pattern of the structure. As a starting point, the capacitance has been varied for a smooth transition between main beam directions as well as using PIN diodes the beam has been switched from boresight to endfire directions. For further gain enhancement Fabry Pérot topology has been implemented forming a cavity within the ground plane and specially designed partially reflecting surface. The single and dual polarized version has been evaluated with dipole and square patch unit cells forming the periodic surface. Compared to the conventional methods the presented work in this project can be an important candidate for achieving an efficient low cost low complexity model without the need of phase shifters and complicated circuitry to achieve the desired specifications.

1.1 Aims and Objectives

This subsection will be providing the scope of the thesis;

- Investigating the possibilities of attaining a low complexity high gain planar antenna with parasitic strips that can be reconfigured for beam scanning.
- Generating a highly directive antenna and investigating low complexity metasurfaces and reconfigurable elements to achieve reconfigurable radiation patterns mainly concentrating on the Fabry Pérot topology.
- A dual polarized version of the high gain model with pattern switching will be considered to achieve a degree of freedom with less interference and further gain enhancement.
- The theoretical design, simulation and validated chamber measurements for the manufactured prototypes will be considered within this work.

1.2 Areas of Novality

- The research involves investigation of reconfigurable antennas where a high gain is targeted with the system to be used in next generation cellular communication systems. The idea of generating simple and generic model where it can be easily modified to be used at different frequencies for the applications requiring high gain and the ability of controlling the beam direction.
- Through the research, a pattern reconfigurable antenna containing a low complexity metasurface and reconfigurable elements are investigated where the gain maximization is mainly achieved with fabry-perot topology. With the aid of parasitic reconfigurable elements the beam is directed towards the intended direction. Theoretical design, and simulation results are validated with the measurement results carried out in the anechoic chamber. Furthermore dual polarized version of the antenna is manufactured

operating at a higher frequency which would be compatible for the next generation 5G frequency band (3.4-3.6GHz) is simulated measured where promising results are attained.

- The novelty is in the combination of low complexity reconfigurable parasitic strips in combination with Fabry-Perot reflectors.

1.3 Thesis Overview

Chapter 2 will be containing the literature review where a flow chart has been included in order to generate a clear understanding of the research area and topics concentrating on the relative fields showing the gap where the project is directed. A general reconfigurable antenna theory and properties such as pattern, frequency and polarization have been considered qualitatively with various methods and approaches. The gain enhancement section is included where various examples of beam steering techniques have been considered as well as the intended section of Fabry Pérot cavity type antennas. A variety of single and superstrate models have been investigated. The anti-resonance condition has also been reviewed where the techniques have been implemented to achieve high gain pattern reconfiguration. The height of the cavity has an important role on defining the resonance and anti-resonance modes where it has been evaluated that with a cavity height of $\lambda/2$, the reflecting surface is close to the radiating structure and the effect of the parasitic strips for pattern reconfiguration are suppressed hence no effect is seen.

Chapter 3, will introduce the basics of antennas and the radiating properties which will be adopted throughout the thesis including radiation pattern, gain, polarization, S11 etc. The equipment which are used in the measurements of the manufactured prototypes including vector network analyzers as well as the anechoic chamber and applied settings are also involved in this chapter. The initial software design and applied settings in order to achieve precise results with CST Microwave Studio® is included in this chapter where a previously proposed model is regenerated for the validation of the results.

Chapter 4, will be representing a methodology and a design progress of a low complexity planar dipole antenna with reconfigurable reflectors to achieve high gain and continuous beam steering along the azimuth plane as well as elevation plane pattern reconfigurability has been considered as well. The stages for generating better understanding over the current distribution along the radiating and parasitic elements and the effect on the radiation pattern have been illustrated extensively. The simulation results will be validated with the manufactured prototype where results will be represented at an operating frequency of $1.85GHz$.

Chapter 5, will present the evolved structure where the design and implementation of the partially reflecting surface has been included. The relative reflection and transmission coefficients have been configured to achieve the gain enhancement property where the height of the cavity formed is crucial. PIN diodes have been implemented for switching the lengths of parasitic strips for either directing the beam or not having any contribution to the radiation pattern due to the smaller lengths of strips relative to the operating frequency.

Chapter 6 will be the final technical chapter where dual polarized structure is studied with the evolved source of a cross dipole and feeding mechanism with a square patch unit cell partially reflecting surface which is used to generate a cavity for further gain enhancement. The operational frequency has been increased to $3.6GHz$ considering the predicted next generation communication systems frequency bands. The generation of the partially reflecting surface as well as cavity height adoption for gain enhancement and pattern reconfiguration has been qualitatively studied. The simulation and measured results achieved from the fully anechoic chamber have been illustrated for both polarizations including co and cross-polarization plots.

Finally a conclusion and future work have been conducted with respect to the achievements from each technical chapter. Comparison between the previously proposed models and conducted studies have been made to prove the novality of the proposed designs. The references and appendices are included at the end of the thesis.

Chapter 2

Literature Review

An extensive review towards the related field of interest have been conducted and presented in this chapter. Different methods and topologies which are previously discovered by authors will be included which would provide a path of discovering a field to identify the research area which will be covered throughout the thesis. A flow chart has been included in order to generate a clearer presentation of the conducted research.

2.1 Reconfigurable Antennas

Antennas are considered as an one of the most important and proliferating components which are mainly used in wireless communication and radar systems with a definition of; a device (wire or a metallic rod) that is capable of radiating and receiving electromagnetic waves [5]. With the developing wireless communication systems there has been an intensive research developing around several antenna models. The common types of antennas which are commonly in use include log periodic antennas, monopole/dipole,slot/horn antennas, helical and loop antennas as well as micro-strip and reflector antennas which contain different characteristic and parameters suitable for specific applications or purposes [4]. Arranging or changing the basic fundamental characteristics and parameters of any antenna design

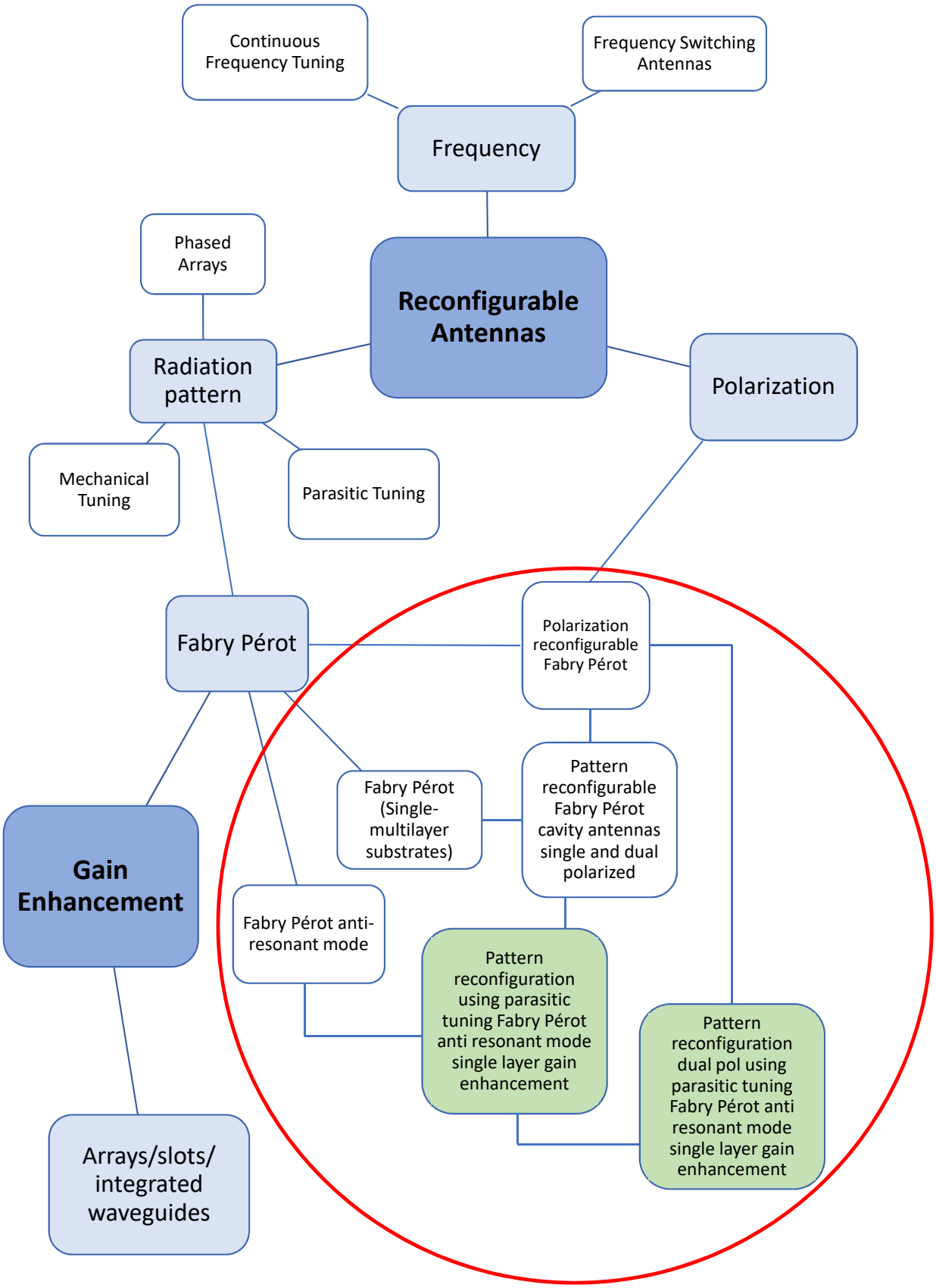

Fig. 2.1 A flow chart representing the relative research areas and the paths followed to direct the project

in order to accomplish a task or a purpose is called configuring. For example, designing an antenna for a specific task or an application, its parameters are configured to generate results satisfying the specifications. As it is mentioned in [6], requesting any change in the characteristic of an antenna will result in developing a new antenna. This will be achieved either regarding to the basic fundamental and theory of the available antenna types or by reconfiguring the antenna that already exists. There are various ways of reconfiguring an antenna where the topology of modifying the currents flowing on the antenna is targeted to adapt the behaviour corresponding to the changes of system specifications and the working environment [4, 6]. This concept is achieved either mechanically where some parts of an antenna are physically moving or electrically where the control over the currents are achieved. Regarding the rapid evolution of electrical devices and components, the techniques used to reconfigure an antenna (ability to adjust the characteristics) have developed proportionally. There are several techniques that have been used which are mainly consisting phase shifters, diodes, tuneable and active materials as well as radio frequency electromechanical systems (MEMS) [2, 4, 6]. Arrays are another widely researched conventional area that can be used as reconfigurable antennas. Compared to a single antenna, array antennas have complicated circuitry where the inter element signal phases are manipulated to achieve beam forming and steering however the basic characteristics of operation has not been changed for the structure [4]. One of the initial studies about controlling the nulls of the radiation pattern reaches back to 1930s where a two element array was used in order to distinguish the direction of the received signal and the beam was controlled with the aid of a variable phase changer allocated in the transmission line of one of the antennas [6, 7]. There are three main parameters which is important in establishing a communication between antennas and by altering these characteristics (parameters), it is possible to have a single antenna communicating with several without the need of designing and implementing a new antenna. The reconfigurable parameters are [2, 4, 6];

1. Radiation Pattern
2. Polarization
3. Operating Frequency

Comprehensive research being carried out about reconfiguring the parameters listed above. In the following section, reconfiguration of these parameters with various antenna model and designs to adopt for different specifications and applications with various techniques will be reviewed. A flow chart representing the path of the research can be found in Figure 2.1 generating a better and clearer vision of the field, previously conducted studies and the targeted area with this thesis.

2.2 Radiation Pattern Reconfigurable Antennas

Presently there has been great attention growing on pattern reconfigurable antennas due to the proliferation of wireless technologies. Since they have the ability to change their lobe and null positions, pattern reconfigurable antennas can be useful to modify the coverage. As shown in Figure 2.2 this is achieved with directing the beam towards the areas where high concentration of users are present. Furthermore being able to adjust the direction of the beam towards the intended direction will lead to a reduction in the system energy consumption as stated in [8]. The main challenge is to generate a system or a model with a good functionality

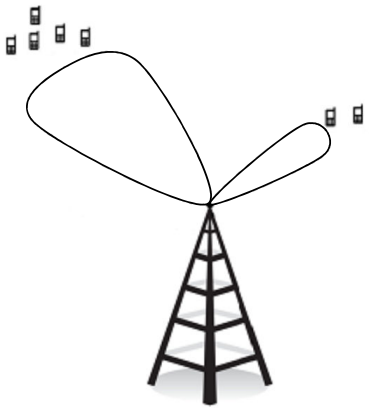

Fig. 2.2 Beam reconfiguration towards the intended areas.

as well as low complexity in order to be cost effective. Pattern reconfigurable antennas can also help to improve system gain as well as steer the beam away from the electronic jamming by changing the direction of the beam which is predetermined by the user depending on the mobile traffic as stated in [9]. A conventional way of beam steering was the use of phased arrays having a complex, high cost and bulky structures, limiting the operation of antennas in various applications [8, 10]. Therefore, reconfigurable antennas with planar structures and lower cost compared to phased arrays are demanding for many applications in communication systems [2, 8].

As it is stated in the work of Bernhard [4], current distribution on antennas' structure has a direct impact on the radiation pattern and this can be supported with the work of Balanis. According to Balanis [5], a simple centre fed finite dipole can be divided into infinitesimal lengths of $\Delta z'$ dipoles and increasing the amount of subdivisions length of a dipole becomes dz'. At each of these incremental lengths there is a relative current with a magnitude and phase that contributes with the generated radiation pattern at the far-field. Far-field known as the plane field is the region where the distance from an antenna does not have an effect on the angular field distribution as quoted in [5]. The inner boundary of a far-field region is accepted from a radial distance of $R = 2D^2/\lambda$ where D is the largest dimension of the antenna and far-field is beyond the distance R. A point on the (E-field) radiation pattern of an antenna, oriented along z-axis, could be generated with the equation 2.1 [5];

$$dE_\theta \simeq j\eta k l_e \frac{(x', y', z')e^{-jkr}}{4\pi r} \sin\theta dz' \tag{2.1}$$

where η and k represents the characteristic impedance of free space 377Ω and the propagation constant $2\pi/\lambda$. Electric field pattern of an antenna can be generated with the summation of all calculated values of E_θ where I_e which corresponds to the current magnitude and e^{-jkr} being the phase of the current at each infinitesimal length. Relative studies about the current distribution and the affects on the radiation pattern of the constructed model/design, it can be concluded that in order to construct an antenna with a pattern reconfigurability property,

it is crucial for the antenna engineer and/or a designer to determine the current allocation along the structure including magnitude and phase to achieve a specific pattern [4]. In order to achieve pattern reconfiguration current characteristics of the structure can be adjusted or rearranged. Since no official technique or common approaches have been invested to guide the researchers, design of pattern reconfigurable structures has become a challenging process. Another important drawback making things more challenging is, the unexpected occurrence of frequency reconfiguration due to the changes in the structure of the antenna where only pattern configuration is desired [10]. However it can be resolved by minimising the contribution to the resonating part of the structure where reflector antennas as well as the use of mutually coupled parasitics can be a possible field to discover. Various techniques have been used towards achieving pattern reconfiguration in the literature where the approaches of using varactors, PIN diodes and switches are essential components for electrical changes where the currents along various paths are controlled to attain pattern reconfigurability which is studied by various authors [9, 11]. On the other hand the use of MEMS and mechanically changing the structure of the antenna to achieve pattern reconfiguration as well as the concept of using arrays has also been investigated widely. The following sections of the literature will be concentrating on the specific methods used to achieve pattern reconfiguration.

2.2.1 Mechanical tuning

In this section of the literature, antennas with the ability to alter the radiation characteristics mechanically to achieve pattern reconfiguration will be examined. It has been almost two decades since Clarricoats and Zhou proposed a pattern reconfigurable mesh reflector antenna where the configuration of the antenna has been altered with the aid of individual stepping motors [12] where the computer controlled motors have been used and the structure has been evolved to an electrically controlled reliable system [13]. The use of linear actuators controlled electrically in order to adapt the shape of an flexible subreflector to attain radiation pattern reconfiguration has been presented in [14] where the satellite signal coverage for intended geagraphical are crucial. Yoon et al. [14] has proposed a reconfigurable dual-offset

contour beam reflector antenna based on the theory of Cassegrain dual-reflector antenna. The structure consist of two reflectors where the main paraboloid reflector is set to attain a specific radiation pattern, the hyperboloid smaller reflector has been placed at a focal distance where the footprint can be adjusted on earth by altering the shape of the subreflector using up to 40 electrically controlled actuators [14]. Within the same year Sievenpiper et al. [15] proposed a leaky wave antenna with a beam steering property where a tunable impedance ground plane has been utilized. As it can be visualised in Figure 2.3, structure of the reflectors consist of two matching pairs of surfaces. Bottom part of the structure is a typical High Impedance Surface (HIS) formed of metallic sheet printed on $FR-4$ substrate with a ground plane. This surface is then covered with an array of tiny, coupled resonant cavities with the aid of conventional multi-layer printing techniques [15]. The mechanically movable surface positioned on top represents the tunable impedance surface with a similar high impedance surface (HIS) positioned at the bottom to obtain an exact overlapping and covered with Kapton polymide for insulation. According to the direction of the movement which is parallel to the electric field, the overlapping area of the metallic sheets vary enabling

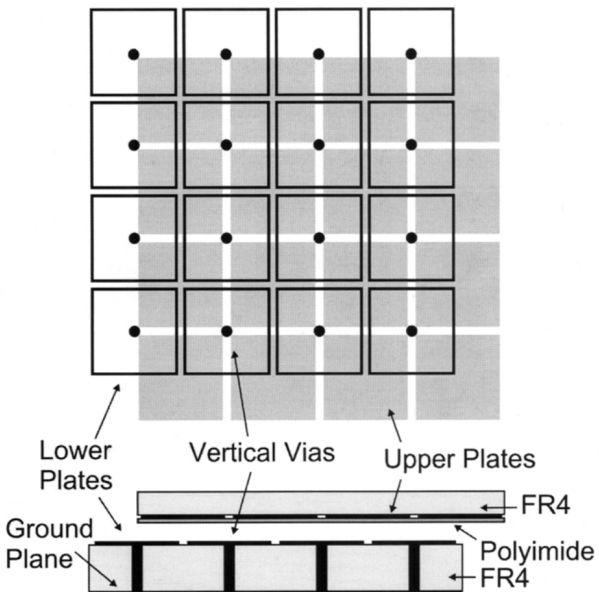

Fig. 2.3 Beam steering leaky wave antenna design using tunable ground plane with the side and top view [15]

the change in capacitance between the two plates [15]. Kapton Polyimide is an insulator placed in between the boards in order to create a parallel plate capacitor when both parts are integrated with each other. Moving the surface over HIS, changes the capacitance on the surface which has a great impact on the resonance frequency of the cavities alongside with a specific angle of movement, a linear phase gradient could be obtained that acts as a virtual tilted reflector where up to $\pm 40^{\circ}$ of beam steering could be achieved at the frequency of $3.1 GHz$ [15]. Microelectromechanical system (MEMS) devices have been of interest with the demand on increasing operating frequency where millimetrewaves or sub-millimetrewaves are considered. Relating to the decreasing size of the antennas with the increasing frequency, the MEMS have been more favourable with their quick response times and small sizes as well as being more effective in power consumption. A planar microelectromechanically pattern reconfigured Vee antenna has been investigated by Chiao et al. [16] where the operating frequency of $17.5 GHz$ has been discovered and a prototype operating at $3 GHz$ has been tested. The structure consisting two radiating arms are constructed on a dielectric material and controlled with the aid of pull and push motions of the microactuators and hence the main lobe direction can be adjusted along the E-plane. There is a demand for $70V - 120V$ biasing pulse voltages for the actuators to operate and achieve beam steering towards the directions of $\pm 30^{\circ}$, 48° and -45° as stated in [16]. More recently Raj et al. [17] have also proposed a pattern reconfigurable planar antenna formed of a patched array where two parasitic patches are located at each side of the driven element resonating at $12.5 GHz$. MEMS switches have been integrated on the transmission lines to control the connection of the microstrip stub lines to the parasitic patches behaving as reactive loading which will interfere with the phase of standing wave pattern and hence radiation pattern reconfiguration has been achieved [17]. With a biasing voltage of $20V$ the actuators are triggered and the beam is directed towards boresight where $\theta = 0^{\circ}$ with "OFF" and $\pm\theta = 30^{\circ}$ "ON-OFF" state MEMS. Corresponding radiation pattern gains for the "ON-OFF" and "OFF" states MEMS are $6.3 dBi$ and $7.4 dBi$ respectively.

2.2.2 Array tuning

The use of arrays have been a conventional way of achieving pattern reconfigurations where bulky structures with complex circuitry including phase shifters have been widely used and investigated by many authors. Associating more than one radiating element and allocating them with different reflection phases, enables the user to adjust and modify the total radiation pattern direction. One of the approaches to achieve pattern reconfiguration was using an array of monopoles printed on a dielectric substrate with a ground plane at the rear side having the ability to reconfigure symmetrically [19]. The monopoles have been reconfigured by changing the radiating structures with the aid of PIN diodes when a $5V$ biasing voltage is applied where a total of four modes are introduced corresponding to the "ON" and "OFF" state variations of four PIN diodes. At a frequency of $2.1GHz$, the monopole array achieves the beam control by varying the surface current distribution with different structures enabling several directions of beam steering. A maximum gain of $5.6dBi$ was achieved with a beam direction of 300° and 60° respectively with two modes. Furthermore the other modes generate

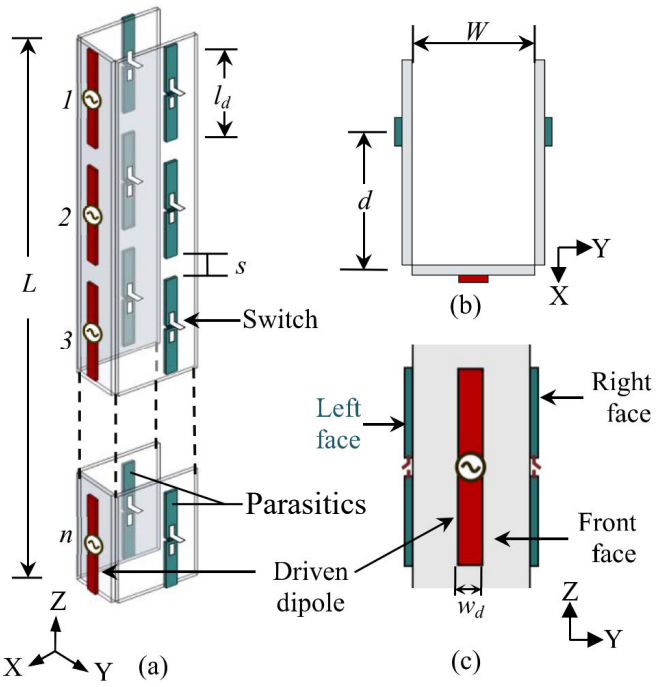

Fig. 2.4 (a) Proposed array geometry, (b) top view, (c) front view of a single subarray. l_d is the dipole length. W_d is the dipole width and s is inter element spacing [18]

a 3.3dBi of gain with a steering angle of 30°, 90° and 270° [19]. As stated previously one of the most popular and conventional beam steering technique can be stated as the use of arrays where an approach of using an array of four dipoles and eight parasitic elements to achieve high gain pattern reconfiguration is presented in [18]. The collinear array geometry enables the structure to be high gain which is directly proportional to the number of elements forming the array. Increasing the number of inter elements would enhance the gain proportionally. However the parasitic set of reflectors which are controlled with RF switches, are manipulated to behave like a reflector as illustrated in Figure 2.4 and hence reflect the beam towards the opposite direction. At the resonant frequency of 5GHz, the beam is steered between $\Phi = 0°$, $\Phi = 70°$ and $\Phi = 290°$ respectively. As discussed in [18], the peak gain towards the specified angles are noted to be approximately 10dBi which could be increased with the element number. Similarly in the publication of Row and Tsai [20], an antenna array has been deployed to achieve multiple beam directions. With the aid of 4 slotted patches which are fed with specifically designed T-junction power dividers, the radiation pattern behaviour of the structure has been varied where a unidirectional pattern is achieved. The feeding mechanism of the structure has been included in Figure 2.5 where the maximum gain of 7.1dBi is attained towards $\Phi = 0°$, $\Phi = 90°$, $\Phi = 180°$ and $\Phi = 270°$ respectively.

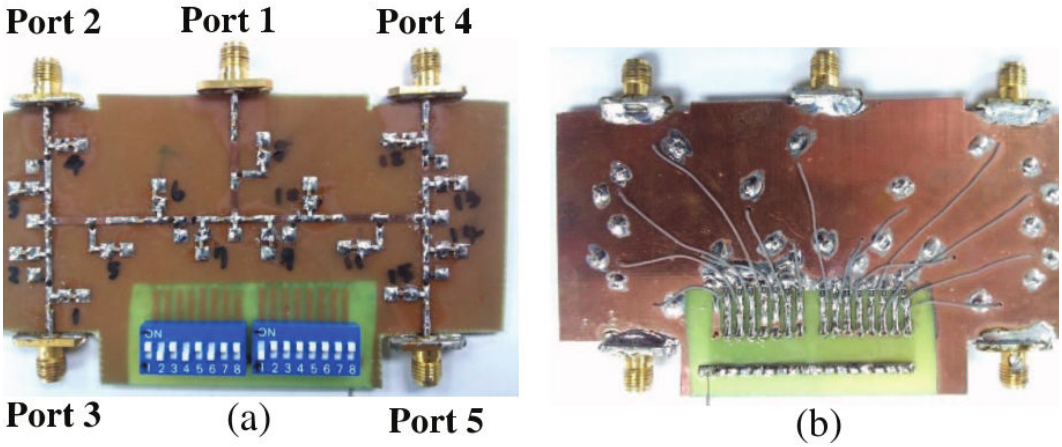

Fig. 2.5 (a) Front view and (b) rear view of the power divider circuitry [20]

More recently a phased array structure of annular ring patch antenna has been proposed [21]. The annular ring structures are fed independently forming an array where the reconfigurability of each antenna is controlled with the aid of PIN diodes creating a path for the current to flow and feed either the left or right hand side of the ring patch by mutual coupling which is placed at the front side of the dielectric substrate with a relative permittivity of $\varepsilon_r = 4.4$. The array is formed of eight ring patches that are fed with an eight-port power divider where the beam can be controlled with eight-way 64-bit digital phase shifters within a range of $\pm 78^\circ$ along the E-plane [21]. The maximum realized gain through the angles of $0^\circ, 20^\circ, 45^\circ, 68^\circ$ and 78° is $12.73 dBi$ where a minimum of $10.16 dBi$ is attained with the beam angle of 78° however the complex system and circuitry including the feeding mechanisms as well as the phase shifters can be the drawbacks for such systems.

2.2.3 Parasitic tuning

Recently, many authors have been going through the path of generating pattern reconfiguration using electrically tuned or switched parasitic elements. A well-known conventional structure with parasitic elements has been used as a base model for many designers to reconfigure patterns. Their conformal profile, smaller size and simpler structures are demanding features for various applications compared to previously investigated methods as reviewed in the literature. This approach has enabled the antenna researchers to obtain pattern reconfiguration without altering the resonant frequency of the antenna [4]. Principally, parasitic elements placed close to the driven element get exposed to electromagnetic field generated by the driven element. As stated in [4] a mutual coupling is generated due to the allocation of the elements which are closely packed where the driven element is used as the feeder, coupling with the parasitics. The change in mutual coupling between these elements change the current distribution on the parasitic elements as well as the driven one. Therefore, arranging the parasitic elements to act as reflectors or directors, pattern reconfiguration can be achieved i.e. the direction of the main lobe where maximum gain is obtained can be tuned [2, 4]. Regarding to the literature, miscellaneous ways of achieving pattern reconfiguration has

been investigated by various authors. The history of using parasitic elements in order to steer the beam goes back to the publication of Harrington in 1978 [22]. Six parasitic dipoles which are loaded with reactive impedances (X_i), have been equally spaced on a circle with the same radius to the centre fed dipole as illustrated in Figure 2.6 [22]. Varying the impedances on each of these elements individually changes the behaviour of current distribution on the specific element in such way that magnitude and phase of the current changes. As previously discussed and explained with Equation 2.1, the current variations along the elements with incremental lengths have direct contribution to the radiated field at the far field region proving the topology of Harrington where pattern reconfiguration along the azimuth plane has been achieved [22].

The approach of Harrington has been implemented into variable models represented with [23] where monopoles are used both as the radiating and parasitic element closely aligned around the radiating element. Altering the currents on the parasitic elements, it has been proven that over 360°, the beam is switched in equally spaced five directions with a maximum gain of $4dBi$ at the operating frequency of 0.9 and $1.9GHz$. An evolved version of the proposed model in [23] with enhanced gain of $8dBi$ towards the intended direction at a frequency of $2.4GHz$ is presented in [24]. A similar approach, of using parasitic arrays, has been published

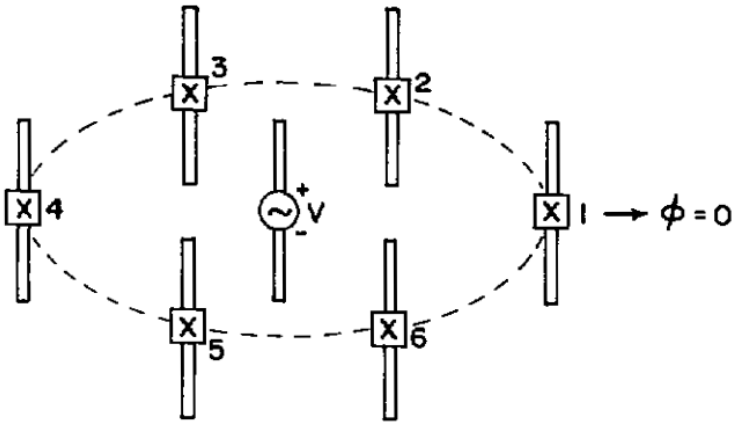

Fig. 2.6 Reactively controlled parasitic array by Harrington [22]

by Ohira et al. [25]. where a portable DOA (direction of arrival) finder was proposed in where the device was used to recognise the arriving waves within 300° angle.

An on-going evolution of the Harrington's approach where low profile and conformal structures are desired in many applications, has moved towards microstrip-based reconfigurable antennas [4, 9]. In 2004 Zhang et al. [26], has generated a reconfigurable microstrip parasitic array with three elements consisting a driven element in the middle and two parasitic elements quarter of a guided wavelength away from the actual feeder operating at the frequency of $3.65GHz$. Parasitic elements have been designed to be shorter than the driven element where additional bits at each side were connected with the aid of switches to achieve longer parasitics compared to the feeder. With the "ON" and "OFF" state of switches, extra bit of copper has been added to the parasitics and regarding to the conventional Yagi-Uda antenna basics, parasitics behave as directors when short and as a reflector when the length is longer than the radiating element. As proposed in [26], an SMA has been implemented as the feeder where the input impedance can be adjusted with changing the position of the SMA along the radiating dipole. With different modes where each parasitic element has been configured to behave as a director or a reflector, the radiation pattern of the antenna has been switched along the H-plane between the angles of $-35°$, $0°$ and $35°$. A similar configuration has been deployed in the publication of [27] as illustrated in Figure 2.7 where the model has been evolved for a better control over the radiation pattern. Three different variations of parasitic length adjustments have been proposed [27]. The feeding mechanism has been kept the same as previous model, however the overall lengths of parasitic strips which are formed of two parts are adjusted to be shorter than the radiating dipole. These two strips are either connected with switches, capacitive loads and lastly capacitive and inductive loads are used to alter the current flow [27]. For all modes the pattern is reconfigured along the H-plane at the frequency of $\approx 3.6GHz$. With the "ON" state switches parasitic strips behave as directors and a maximum beam switching is attained at an angle of $\pm 25°$. However the currents induced on the parasitic strips with shorter lengths at the specific resonant frequency is low therefore the contribution to the radiation pattern is minimal therefore for the "OFF" state, the radiation pattern is towards the boresight $\theta = 0°$. The second topology was to capacitively load the

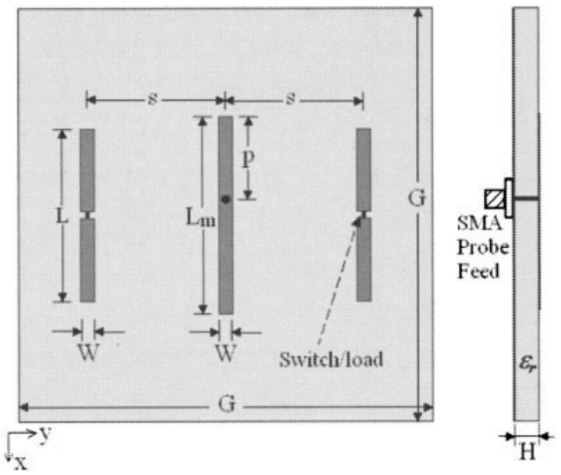

Fig. 2.7 Pattern reconfigurable microstrip parasitic array by Zhang et al. [27]

parasitic strips to control the current flow to achieve a smooth scanning. The capacitances have been varied from $0.25pF$ to $3.9pF$ which can be achievable with a varactor diode and $\theta = 0^\circ$ to $\pm\theta = 27^\circ$ degree of smooth beam steering is achieved. Lastly the combination of inductors and capacitors are used where the parasitics behave as reflectors and the beam is tilted towards the opposite side with smooth transition between $\pm\theta = 32^\circ$ and $\pm\theta = 54^\circ$ with variable capacitance. However the gain of the proposed models are not considered but is an essential property to be studied for current and next generation communication systems.

An array of parasitic patches has been studied by Preston et al. [28] formed of a radiating patch and two parasitics closely aligned together with decreasing patch sizes to direct the beam when operated. The current distribution along the patches are adjusted by shorting the maximum current position where the patch behave as a reflector othervise the patches act as directors [28]. The proposed model can operate at a resonant frequency of $1.5GHz$ and is capable of reconfiguring the radiation pattern towards the angles of $\theta = -34.8^\circ$ and $\theta = 39.6^\circ$ respectively. The gain for such models towards the peak steering angles are noted as $2.4dBi$. Over the last decade two papers have been published by Yang et al. about pattern reconfigurable Yagi patch antenna operating in the X band as well as an enhanced gain in contrast to [28] and frequency reconfiguration has also been achieved [29, 30]. The proposed model illustrated in Figure 2.8 consisting a driven element with two parasitic elements

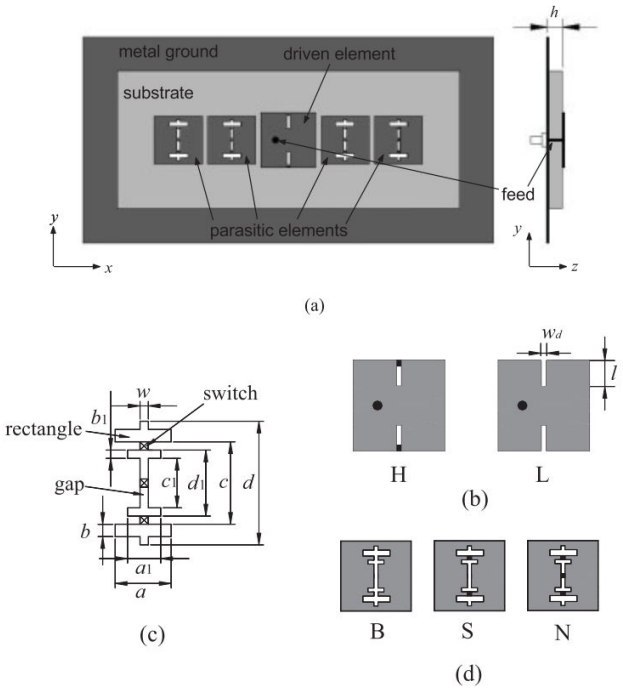

Fig. 2.8 Frequency and pattern reconfigurable yagi patch antenna with slits on parasitic and driven element Yang et al. [29]

located at either sides of the driven one. All elements contained in the structure are in the form of patches where dimensions of the parasitic elements are shorter compared to the driven element regarding to the Yagi-Uda basics. The pattern and frequency reconfiguration is attained with manipulating the currents on the radiating element and parasitic patches. Slits are etched on the patch array in a particular way to gain a control over the currents providing a frequency reconfiguration when adjusted on the radiating element. The parasitic patches and the slit configurations are illustrated in Figure 2.8 including the switch positions and configurations for different modes. Altering the switch modes as "ON" and "OFF", different modes can be attained where the lengths of these slots are varied in order to achieve more inductive or capacitive patches. Increasing the length of a slot which is shown as "B", increases the inductance on the patch where it resonates almost at the same frequency as the driven element forming a delayed current on the patch that acts as a reflector. On the other hand "S" and "N" modes lead to capacitive behaviour because of their lengths being

short compared to the driven element, therefore the parasitic patches act as directors. In the end varying the length of slots, changes the direction of the radiation pattern and beam switching is achieved on two frequency bands due to the slits on the driven patch as stated in [29, 30]. Regarding to the adjustments, the pattern is reconfigured to $\theta = -7^{\circ}$, $\theta = 33.5^{\circ}$ and $\theta = -40^{\circ}$ with the gains of $6.3dBi$ and $8.8dBi$ respectively.

2.3 Polarization Reconfigurable Antennas

The communication in a wireless sense can be achieved only when polarizations of both transmitter and receiver antennas are identical. Therefore, in order to achieve a reliable high quality link where the interference with adjacent signals within the spectrum are minimised, polarization reconfigurable antennas can be an effective candidate [4]. The polarization reconfigurability can be achievable within linear polarizations (Horizontal/Vertical), circular polarizations (Right-handed/Left-handed) and also linear to circular polarization. Structural changes as well as the use of switches for using different feeding mechanisms have been studied in general to achieve polarization reconfiguration. A variety of slot coupled structures for polarization diversity have been studied by various authors where different feeding mechanisms are implemented to switch between the slots to be excited. Some related studies have been reported in this section. In [31], two slot fed patch antennas have been introduced. A single port feeding line was implemented to excite the two diagonal slots which are short circuited with PIN diodes to achieve either sense of circular polarization. A probe fed microstip patch antenna with two orthogonally etched slots are introduced in [32, 33]. The surface currents on the patch antenna along the slots are controlled with the aid of PIN diodes where biasing circuits have been implemented to achieve "ON" and "OFF" states of diodes. The "ON" state PIN diodes enable the surface currents in the particular direction to flow through the slot forming two smaller sized slots. With the combination of "ON-OFF" states for the diodes the polarization has been switched between right-handed circular polarization (RHCP) and left-handed polarization (LHCP) [32, 33]. A different approach of attaining linear polarization, RHCP and LHCP is proposed in [34] where a microstrip patch antenna

has been used a source with a quarter of a wavelength long transformer in order to achieve an impedance matching to 50Ω. Each corner of the patch antenna has been truncated and PIN diodes are implemented for each triangularly shaped edges to gain a control over the structure. With different states of the PIN diodes polarization reconfigurability has been achieved. More recently an approach of using an array of bow-tie shaped dipoles to achieve dual polarization is presented in the [35]. The printed dipoles have been placed vertically on a ground plane where the feeding baluns have been etched on the rear sides of the dielectric substrate. The array is controlled with the aid of two ports feeding system where vertical and horizontal polarizations have been attained with a gain enhancement as a result of the array form. Similarly the use of cross dipole model of square patches to achieve polarization reconfiguration was proposed in [36]. Two feeding mechanisms have been implemented to excite the orthogonally placed dipoles which are placed vertically above a ground plane. With the use of differently oriented dipoles which are fed one at a time, dual polarization has been achieved.

2.4 Frequency Reconfigurable Antennas

A frequency reconfigurable antenna has the capability of tuning the operating frequency so that communication in various bands can be accomplished [2]. As it is mentioned in the publication of Jennifer T. Bernhard [4], frequency reconfiguration can be obtained in two ways. One of them is, switched tunable antennas using a switching system that enables the antenna to operate at specific frequencies. On the other hand, instead of having frequency jumps between desired bands, smoother frequency changes can be achieved by continuous-frequency tunable antennas [4]. Most of these antennas are operated in resonance as stated in [4]. Therefore altering the electrical length of such antennas changes the resonant frequency i.e. the operating frequency of the antenna. The first resonant frequency of a simple dipole can be obtained with a length of $\lambda/2$ (half wavelength). According to the statement above it can be concluded that, increasing the length of a dipole will shift the resonance to a lower frequency where decreasing will lead to operation in higher frequencies [4].

2.4.1 Frequency switching and continuous frequency tuning

In this section of the literature several examples of resonant frequency switching approaches with the aid of PIN diodes or RF-MEMS will be investigated which are commonly used to change the length of the antenna so that hopping between several frequency-bands have been attained [37, 38]. Since the technology used to control the switching is with active components, in order to operate or change between modes there will be the need of biasing voltages which may interfere with the current distribution generated with the radiating element and hence an effect to the radiation pattern or the resonant frequency can be seen. Therefore Freemen et al. [39] has proposed a monopole design where optical switches depending on light intensities were introduced, minimizing the electromagnetic effect of wires and biasing on the frequency and radiation pattern characteristics of the antenna. A similar way of achieving frequency reconfiguration has been presented in the work of Panagamuwa et al. [11] where photoconducting silicon switches controlled by the lasers with the aid of fibre optic cables have been used to adjust the arm length of a printed dipole as shown in Figure 2.9a. As it can be observed from Figure 2.9b, with the "ON" state switches (short circuit) antenna operates in lower frequencies. At the "OFF" state, switches behave as insulators where no current flow is permitted beyond the switches (open circuit) therefore the antenna radiates at its shorter length, which means at a higher frequency [11].

As mentioned before numerous ways of frequency reconfiguration is studied by many authors. However instead of switching between several frequencies discreetly, a smoother transition between the frequencies are targeted by several authors including Hum et al. [40]. A differentially fed patch antenna has been deployed where the implementation of varactor diodes have been essential for achieving smooth frequency tuning with their spectacular current control ability. Two patches have been capacitively loaded with varactors and controlled separately to attain the control over the currents on both patches and hence achieve a frequency tuning over a $2GHz$ frequency range [40]. Similarly the use of varactor diodes are presented in publications [41, 42]. The positions of variable capacitors (varactor diodes) placed on the slot antennas have a significant impact on both of the resonant frequencies

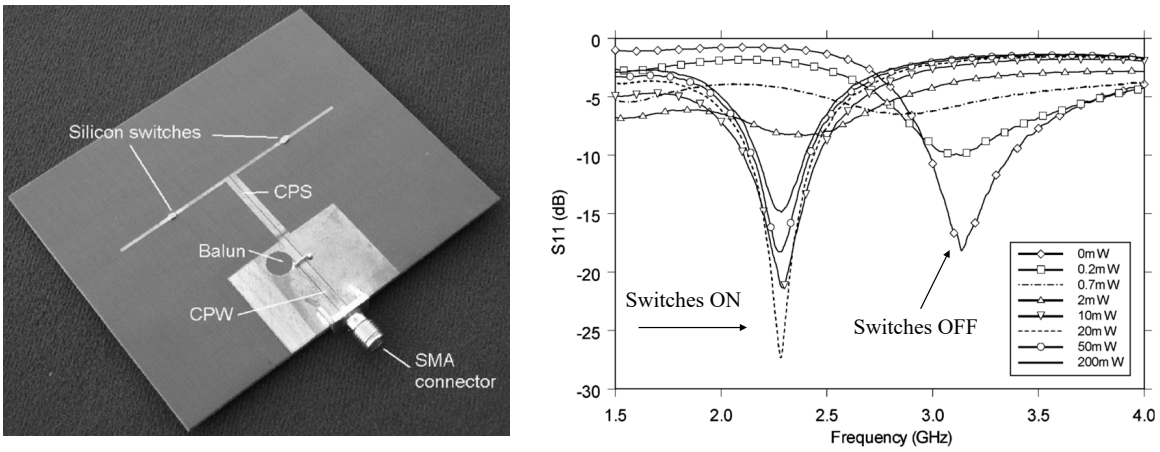

(a) Antenna configuration (b) Return-loss with increasing optical illumination

Fig. 2.9 Frequency reconfigurable antenna using photoconducting switches [11]

(dual band) of the antenna where each band can be tuned individually. Capacitively loading the slots, it is observed that for both bands resonant frequencies shift down and hence attain a smooth frequency tuning [4, 41].

2.5 Gain Enhancement

This section will be concentrating on the gain enhancement methods including arrays, slots, integrating waveguides as well as the partially reflecting surfaces. The Fabry Pérot topology and the integration of single and multilayer reflecting surfaces for gain enhancement along with the pattern reconfiguration will be extensively reviewed in this section. Antenna gain has been crucial for recent and future communication systems due to the demand for higher frequency bands where the spectrum is suitable for huge bulks of data transferring. Increasing the frequency up to the millimetre wave regions the signal is dispersed rather than being in a wave form therefore antennas with high gains are more favourable to establish a communication. A substrate integrated waveguide (SIW) leaky wave antenna array has been proposed in [43]. An array of slots have been powered with cascaded (SIW) power divider and slot lengths are varied for gain enhancement. The complexity of manufacturing

and feeding mechanism can be stated as drawbacks for such design however a maximum gain of $18.4dBi$ has been attained. An approach of using arrays to achieve gain enhancement is presented in [44]. The design is formed of a rounded bow-tie resonators fed by a balun and the gain is enhanced with the aid of vertically placed array of double sided split ring resonators (SRR) behaving as MU-near-zero (MNZ). The integration of resonators behaving as (MNZ) have enhanced the gain of a conventional bow-tie antenna by approximately $6dBi$ in broad range of a bandwidth 34.5% [44]. More recently a slot antenna array has been introduced in [45]. A double sided EBG structure and grounded slabs forming a checkerboard surface (CS) was assembled closely to the feeding slot array with an antenna spacing of 0.83λ resonating at the frequency of $5.9GHz$. Comparing the proposed model with the original slot array, a gain enhancement of $2.1dB$ has been attained. Another way of using an array of antennas for gain enhancement has been introduced recently in [46]. Circularly polarized cross dipoles with ellipse shapes and with feeding harpoon-shaped patches have been placed within a loop cavity is presented. Then a $2x2$ array was created and a phase shifting network has been adopted where the gain is highly dependent to the loop cavity parameters as stated in [46]. A wideband behaviour has been attained with axial ratio bandwidth of 85.7% and $13.91dBi$ circular polarization gain towards the boresight direction where $\theta = 0^{\circ}$.

2.5.1 Fabry Pérot topology for gain enhancement

The history of using partially reflecting surfaces for enhancing gain towards the boresight direction goes back to the publication of [47] where the Fabry Pérot resonance condition was first applied. A single source has been used to feed the cavity of height usually $\lambda/2$, formed of a partially reflecting surface (PRS) and a metallic sheet of a ground plane and hence in phase reflections are generated to attain gain enhancements which will be explained in detail in the upcoming chapters. This technique has been widely investigated by various authors where a waveguide aperture have been used as a source in [48] and a dipole PRS is placed a distance of $\lambda/2$ away from the source. A peak gain of $21.9dBi$ has been attained with the traditional Fabry Pérot resonant condition [48]. A similar feeding mechanism is presented

in [49] where a slot has been used to deliver the energy to the cavity from the waveguide aperture. However multiple substrates with different unit cell configurations formed of square patches are combined in order to achieve a high gain and a broad bandwidth at the resonant frequency of $14.5GHz$. The three substrate model which are placed $\lambda/2$ distance away from each other with different patch sizes generates a peak gain of $\approx 19.5dBi$ and 15% bandwidth have been presented [49]. A rectangular microstrip patch fed Fabry Pérot cavity antenna is illustrated in [50]. The planar partially reflecting surface has been modified to be highly directive with inductive and capacitive grids which are implemented on both sides of the *Rogers*5880 dielectric substrate. The peak gain of $16dBi$ has been attained with a $3dB$ gain bandwidth of 11.23% [52]. Although a single source feeding the cavity have been explained above, an array of patches were used as a source of the multilayer EBG with variable spaces between the substrates for array thinning and gain enhancing capability [53]. The $2x2$ array enables a dual polarization depending on the allocation of radiating patches where up to $19dBi$ gain with $30dB$ isolation have been presented. A combination of a PRS and an AMC surface as perfect magnetic conductor (PMC) is introduced in [51]. A radiating patch antenna has been used a source which is placed on a PMC ground plane and it has been proved that the resonance is achieved with a shorter cavity height of $\lambda/4$ instead of the traditional $\lambda/2$ wavelength as illustrated in Figure 2.10. The new structure with a PMC ground plane has

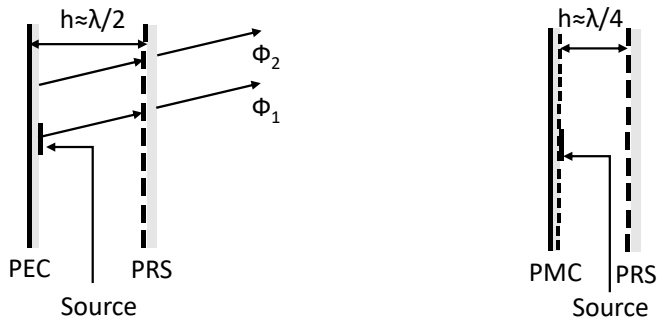

(a) Resonant cavity formed by PEC and PRS (b) Resonant cavity formed by PMC and PRS

Fig. 2.10 Fabry Pérot resonance with PEC/PMC and PRS with $\lambda/2$ and $\lambda/4$ cavity heights regenerated from [51]

reduced the profile of the antenna since the cavity height has been reduced however the highly resonant cavity still produces around $19dB$ of gain towards the boresight direction $\theta = 0^\circ$ at the resonant frequency of $14GHz$. Latterly, a new approach for achieving a low profile high gain antennas with the use of passive periodic structures is presented in [54]. The same technique of using partially reflecting surfaces and artificial magnetic conductor combination has been used in a conformal structure to reduce the profile. The antenna size have been reduced from $\lambda/2$ to much smaller size of less than $\lambda/6$ wavelength [54]. A metallic cylindrical ground plane is surrounded with an EBG superstrate and a cavity is formed with a high impedance surface with the same dimensions. The dipole feeding the cavity is located in the middle of the two surfaces and a maximum directivity of $12.7dBi$ has been achieved at the operating frequency of $2.33GHz$ [54].

Two publications where the source is placed within the cavity with single and two layers of dielectrics are proposed in [55, 56]. The source is a slot coupled patch antenna which is positioned within the cavity using a spacer to generate an airgap and reduce the amount of surface waves affecting the performance of the antenna [55]. The single substrate model illustrated in Figure 2.11a is formed of a capacitive layer formed of square patches and an inductive grid etched on either side of the substrate enabling a positive phase gradient where the resonant frequency can be determined by adjusting the cavity height. The wideband property of the antenna has been achieved with a matching network placed on the feeding

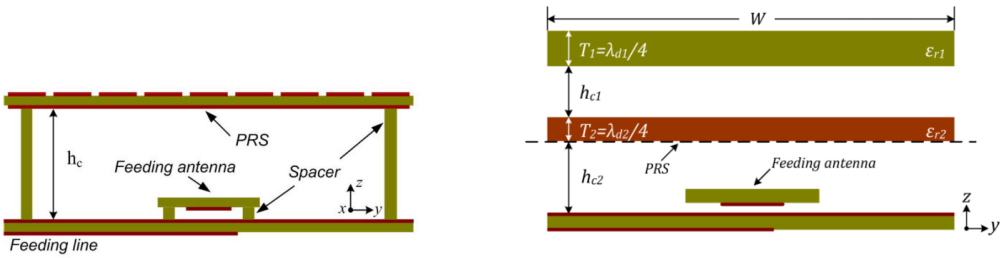

(a) Two layer substrate model

(b) Two substrate model

Fig. 2.11 Wideband Fabry-Pérot resonator antenna models [55, 56]

mechanism [55]. A boresight peak gain of 13.8dBi along the band of 8.6GHz to 11.4GHz has been achieved with the proposed model. Similarly the two dielectric substrate model shown in Figure 2.11b has been fed with a slot coupled patch antenna with a matching circuit for wide band operating range however a positive reflection phase slope is attained with the different impedance characteristics of the substrates which are aligned to have $\lambda/2$ wavelength separation. Since effective permittivity ε_r of substrate positioned on top is higher, the impedance transforms and positive gradient is attained which leads to a boresight peak gain of 15dBi and a 25.8% of 3dB gain bandwidth with a centre frequency of 15.5GHz [56]. Similar ways of attaining gain enhancement using Fabry Pérot resonance condition is studied in publications [57–59]. Despite the use of patches as a source, a well known dipole antenna has been implemented within the cavity approximately $\lambda/4$ away from the ground either a PEC or an AMC forming in phase reflections as studied in [60, 61]. Various approaches of attaining high gain using Fabry Pérot and increasing the operational bandwidth with progressively tapered unit cell for the partially reflecting surface as well as an s-shaped one is presented in [62, 63]. Metallic side walls have been included in the design to prevent the energy leaking out from the cavity and hence further enhance the gain [62]. To visualise and gain a better understanding about how to attain resonance condition with different height and possible ways of coping with the phase delay has been studied in [64]. A source of a patch antenna is used as a feeder whilst the height of the cavity is varied with integral multiples of the guided wavelength. The partially reflecting surface design involves metallic patches of various sizes which are reduced gradually towards the edges in order to recover the phase delay due to the increasing height of the reflecting surface [64]. There has been many other approaches examined intensively using Fabry Pérot for gain enhancement in [65]. A new approach of anti-resonant mode of the Fabry Pérot condition have been proposed with the two publications of Kim et al. [66, 67]. A cavity has been created with the frequency selective reflectors placed on the either side of the radiating element which is a hairpin dipole placed over a PEC ground. Due to the anti resonant mode as well as the constructive reflected waves from the ground the gain is enhanced towards the boresight direction and by implementing

two more set of reflectors at a particular distance a wider bandwidth has been attained which is explained in detail at Chapter 3.

2.5.2 Fabry-Pérot cavity type antennas and beam steering

In this section of the literature various examples of attaining high gain beam steering using the approaches of Fabry Pérot topology with the use of partially reflecting surfaces which are relatively comparable with this project will be reviewed.

Single and dual polarized high gain pattern reconfigurable Fabry Pérot antennas

The beam steering techniques of high gain Fabry Pérot resonator antennas which will be included in this section are commonly concentrated on attaining a control over the reflection phase of the surface forming a cavity where high intensity of active components as well as specific unit cell modifications are used. An approach of using capacitive patches and inductive mesh grid which were etched on either sides of a dielectric substrate and aligned to overlap each other and hence achieving a tilted beam is studied in [68]. The cavity has been reduced effectively to $\lambda_0/4$ from the traditional $\lambda_0/2$ with the use of both inductive and capacitive layers where a reflection phase of 0° is attained. The beam reconfigurability has been achieved with changing the reflection phase of the surface where the patch sizes and the mesh grid dimensions are the parameters to be adjusted. Three variations of patch and grid sizes have been tried, it has been observed that the pattern could be switched to three different directions up to 27° with a peak gain of $14.2dBi$ however the model is based on the simulation results. A beam tilting approach using a homogeneous and inhomogeneous periodic elements as a surface is presented in [69]. The periodic elements are formed of square loops and hence by gradually varying the side widths of the loop changes the phase distribution affecting the radiation characteristics of the model. The system is fed with a source of patch antenna printed on dielectric substrate over a large ground plane with a frequency range between $7.65GHz - 8.27GHz$. For the normal structure with homogeneous

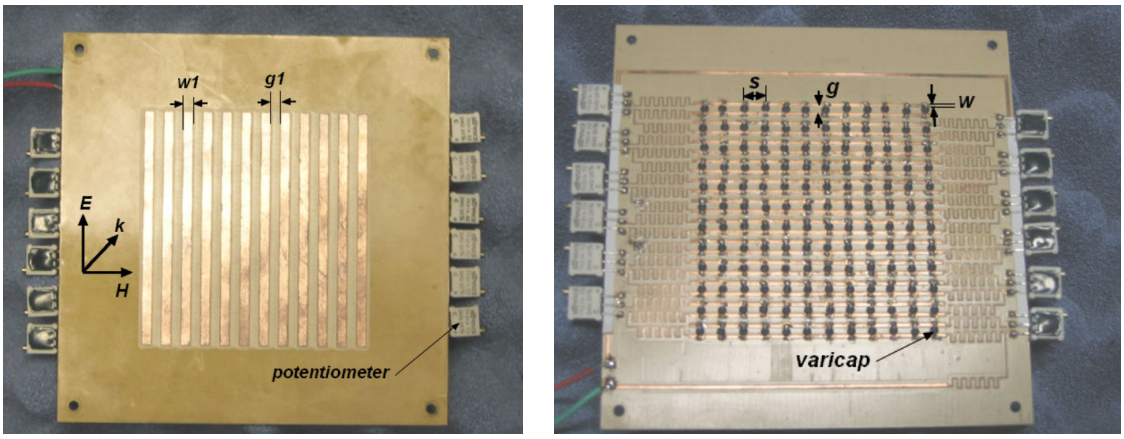

(a) Inductive grid of PRS (b) Capacitive grid of PRS

Fig. 2.12 Electronic beam steering high gain cavity type antenna model [70]

array of loops the gain is directed towards the boresight direction however with gradating loop widths it has been experimentally proven that a $16.4dBi$ gain at an angle of $\theta = 33^\circ$ has been achieved [69].

In [70], a combination of an inducting grid and an active capacitive one is integrated to form a partially reflecting surface placed on top of a PEC ground to form a cavity with a source of patch antenna resonating initially at $8.1GHz$. Altering the biasing voltage between $0-10V$ of the inserted varactor diodes within the capacitive grid, the phase of the reflecting surface has been adjusted locally and hence pattern reconfiguration is attained. The prototype model is illustrated in Figure 2.12 where potentiometers were also included to achieve continuous phase change locally along the reflecting surface. Although pattern reconfiguration is targeted it has been observed that changing the biasing voltages also increases the resonant frequency of the model within $7.92GHz-8.21GHz$ range [70]. A nonuniform reconfigurable partially reflecting surface formed of square patches where each unit cell is divided into two rectangular patches and connected with PIN diodes to form an array of square patches has been presented in [71]. For further gain enhancement, two element microstrip patch array has been preferred as the source which has a resonant frequency range of $5.5-5.7GHz$. The PRS surface has been sectored into two parts where the PIN diode states are varied to attain different phase distributions to allow beam steering. Experimental

results have proven that, a maximum gain of 16.3dBi towards the boresight is achieved. With the combination of "ON" and "OFF" state PIN diodes a peak steering angle of $\pm 15^{\circ}$ has been attained due to the symmetry and relative gain at the desired direction is depicted as 11.7dBi respectively [71].More recently the evolved model of [71] is proposed in [72] where an aperture coupled patch antenna was used as a source and further phase control has been introduced with the new meta-surface configuration operating at 5GHz. The meta-surface is formed of a mesh grid integrated with rectangular patches connected with PIN diodes to form a square patch. With the adjustments of PIN diode states (ON-OFF), different reflection phases have been attained at particular parts of the reflecting surface. The manufactured prototype is illustrated in Figure 2.13 showing the intensity of the active elements which are used to gain a control over the reflection phase. For the four different divisions of meta-surface that can be controlled separately, due to the symmetry six different combinations of beam steering angles are presented with a maximum of $\pm 54^{\circ}$ and a gain of 6.3dBi. A peak gain of 11.1dBi is achieved with the "OFF" state PIN diodes towards the boresight direction $\theta = 0^{\circ}$ [72]. A dual polarized version of the model is proposed in [73] where a PIN diode is implemented to the feeding mechanism to feed the patches with different polarizations.

There has been various publications reflecting the polarization reconfigurability of the Fabry Pérot cavity antennas where the source and the unit cell of the reflecting surface have been

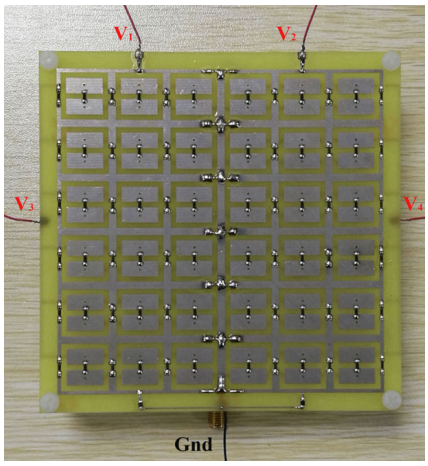

Fig. 2.13 Reconfigurable meta-surface proposed model with active components Ji et al. [72]

modified. An approach of using a single source of a patch antenna is proposed in [74]. A dual polarized feeding mechanism has been implemented to feed a single microstrip patch antenna. A partially reflecting surface was formed of a plus shaped loop unit cell array and MEMS were included within the design to activate the relative metallic strips for desired polarization. A squared patch PRS structure was introduced with a dual patch model as a source [75]. The two radiating patches were excited separately one at a time with the aid of coaxial probes for different polarizations and due to the square unit cells of the reflecting surface the gain has been enhanced for both polarizations where a cross-polarization level of $-25dB$ was attained [75]. A stacked patch feeding technique is introduced in [76] in order to achieve polarization diversity. The patch antenna placed on the bottom layer of dielectric substrate has been excited with two different ports placed on adjacent sides of the patch to achieve vertical and horizontal polarization diversity. More recently a dual polarized slot fed patch antenna array was introduced in [77]. Two port feeding mechanisms have been implemented in order to excite both patches at the same with a phase difference of 180°. The polarization diversity has been achieved by exciting the patches using different slot apertures at the same time which are positioned either horizontal or vertically on the opposite face of the dielectric [77].

Chapter 3

Background, Equipment and Software Overview

Relative background theory and basic concepts that are used to conduct the research and carry out the experimental work will be explained in this chapter. Antenna parameters as well as the simulation programme used to create the models will be discussed and previously published results will be regenerated for comparison purposes. Utilizing the software programme, applied settings for reliable and precise results as well as the experimental set-up for measurements will be discussed.

3.1 Antenna Fundamental Parameters

In this section, antenna parameters which will be used to identify, analyse and characterize the behaviour of the constructed antenna model will be theoretically explained.

3.1.1 Radiation pattern

The radiation pattern of the antenna is the graphical or mathematical representation of the radiation field of the structure representing the properties of the antenna. Most commonly the antenna is placed at a distance from the radiating element known as the farfield region where the pattern is a function of the directional coordinates [5]. Essentially the free space distribution of the radiated electromagnetic waves within a medium or an open space is illustrated with the aid of 2D or 3D plots which is stated to be the function of the observer's position usually along a path with a constant radius [5]. Relatively important radiation properties of an antenna can be listed as the flux density, radiation intensity, directivity, field strength and polarization respectively. A point source, having an evenly distributed radiation pattern in all directions (Omnidirectional) is known as an isotropic radiator where common parameters such as directivity and gain can be defined with respect to this measure.

3.1.2 Field regions

This is an important parameter for the antennas, to specify the different radiation behaviour among the various distances away from the radiating source since the wireless communication is achieved over certain distances. The surrounding environment of an antenna is categorised into field regions displaying different behaviour within each particular region. These regions are well known as the reactive near field, radiating near field and the far-field regions respectively [5]. Most commonly used region can be stated as the Far-field region where angular distribution is independent of the radial distance to the antenna. The minimum distance for the inner boundary of a Far-field known as the Fraunhofer region is $R = 2D^2/\lambda$ [5] where (R) is the distance to the antenna, (D) represents the maximum length of the antenna and (λ) is known as the wavelength.

3.1.3 Efficiency

The efficiency of an antenna determines the effectiveness of power usage which is accepted and radiated by the antenna where various factors such as the reflections caused by the mismatch, conduction and dielectric losses has a significant effect. The total efficiency e_0 can be demonstrated with equation (3.1) [5];

$$e_0 = e_r e_c e_d \tag{3.1}$$

where e_r, e_c and e_d represents the reflection efficiency as a consequence of the missmatch, conduction efficiency and dielectric efficiency respectively. The reflection efficiency e_r can be specified as $(1-|\Gamma|^2)$ where Γ is known as the voltage reflection coefficient at the antenna inputs. Furthermore, the radiation efficiency of the antenna can be stated with $e_{cd} = e_c e_d$ which is used to distinguish and relate the directivity and gain [5]. The reflection coefficient can be expressed using;

$$\Gamma = \frac{Z_{in} - Z_0}{Z_{in} + Z_0} \tag{3.2}$$

where Z_{in} and Z_0 represents the antenna input impedance and the characteristic impedance respectively.

3.1.4 Gain

According to the work of Balanis [5], it can be stated that the directivity of an antenna is the ratio of “the power that is radiated from an antenna per unit solid angle” known as the radiation intensity to the radiation intensity of an isotropic radiator. Isotropic radiator is known as an ideal source that radiates equally in all directions which ideally does not exist

however it is used as a reference [5]. Mathematical expressions for the radiation intensity as well as directivity is represented with equations (3.3),(3.5);

$$U = r^2 W_{rad} \tag{3.3}$$

where U, r and W_{rad} is radiation intensity ($W/unitsolidangle$), the distance from the antenna and radiation density (W/m^2) respectively. Radiation intensity of an isotropic radiator can be written as;

$$U_0 = \frac{P_{rad}}{4\pi} \tag{3.4}$$

where P_{rad}= Total radiated power (W). Therefore the directivity can be stated as;

$$D = \frac{U}{U_0} = \frac{4\pi U_{max}}{P_{rad}} \tag{3.5}$$

Antenna gain is an essential parameter for performance characterization of the model which is one of the main investigated parameter throughout the thesis for evaluating the performance of the antennas. It can be closely related to the directivity as discussed previously however the efficiency of the antenna is also considered as well as the directionality. The relation of antenna radiation efficiency with the radiated and accepted power is illustrated in (3.6);

$$e_{cd} = \frac{P_{rad}}{P_{in}} \tag{3.6}$$

where P_{rad} and P_{in} represents the total radiated power as well as the total input (accepted) power by the antenna respectively. Including the losses related to the reflection/mismatch

as well as the antenna radiation efficiency, the antenna gain with a function of spherical coordinate angle θ and ϕ can be illustrated using (3.7);

$$G(\theta,\phi) = e_{cd}D(\theta,\phi) \tag{3.7}$$

3.1.5 S-parameters

In an antenna design or a communication system, one of the crucial parameters which is used to identify the ratio of incident and reflected voltage at the input and output terminals of the system which can be denoted as the reflection coefficient (Γ or Return Loss) which is a function of Scattering parameters (S-parameters). Reflection and transmission coefficients are considered the main branches of scattering parameters which are functions of the frequency [78].

Considering an antenna design, S11 parameters are relatively important where the amount of power reflected back from the terminals of an antenna towards the source (generator) known as the return loss (R_L) is attained verifying the accepted power by the antenna. The return loss is expressed with a positive value since it is a loss quantity however S11 will be a negative value presented in dB where the ratio of accepted and reflected power can be determined using (3.8);

$$S11 = -R_L = -10log|\Gamma|^2 = 20log|\Gamma| \tag{3.8}$$

Ideally for an antenna all the power delivered to the input terminals of the antenna is accepted by the antenna when $S11 = -\infty$ and no power is reflected. Likewise $S11 = 0dB$ would identify that all the power is reflected back to the source and no power is accepted by

the antenna. Whereas the threshold for the antennas is to attain a minimum of reflection coefficient of $S11 = -10dB$.

Similarly for a two port network the reflection coefficients S11 and S22 are evaluated to distinguish the matching of the antennas at both ends. Additionally the transmission coefficients (S21) are computed to measure the amount of power transferred between the two ports where the power is transmitted from port 1 to port 2 and S12 representing the power transmitted from port 2 to 1 is considered respectively.

3.1.6 Polarization

Ideally two antennas operating within the same frequency band, requires the electromagnetic property of polarization to be the same at both ends in order to establish a communication. The electromagnetic waves radiated by the antenna propagate in space in the form of electric and magnetic fields. Electric fields radiated by the antenna can be expressed as vectors that have time varying magnitude and phase [5]. The polarization of an antenna can be determined by the direction of the E-field vector where Earth's surface is accepted as the reference plane [5]. Among different parts of the radiation pattern various polarizations could be attained however, if the direction of the propagation is not stated, polarization along the maximum gain direction is accepted to identify the polarization of the antenna [5]. Due to the different variations of the Electric-field propagation in free space, the polarization behaviour is assorted in three main categories identifying the polarization characteristics of the antenna.

1. Linear Polarization
2. Circular Polarization
3. Elliptical Polarization

Linear polarization will be the main electromagnetic propagation characteristic considered with the designed models within the thesis. However dual polarization capability will be investigated and implemented to the model where the linear polarization will be used with multiple E-vector directions.

3.2 Fabry Pérot Topology

Since Trentini [47], has proposed his work about enhancing antenna gain by positioning partially reflecting sheet arrays in front of the antenna forming a resonant cavity, a widely known Fabry Pérot resonance condition was introduced [51]. The concept is to generate a structure with multiple in phase reflections produced within the cavity [47]. Adjusting the distance between reflector sheet and partially reflecting surface in order to obtain dispersed rays with a same phase have resulted to an increase in the directivity/gain of the structure [47, 51]. This approach of Trentini has been used as a model for many structures proposed by various authors [48, 51, 65]. Directivity at the boresight direction can be represented mathematically in (3.9);

$$D = \left(\frac{[1-\rho^2]}{1+\rho^2-2\rho cos(\Delta\phi)} \right) \tag{3.9}$$

where ρ and $\Delta\phi$ represents the amplitude of PRS reflection coefficient $\rho e^{j\phi}$ and the phase difference respectively. For a consecutive in phase reflections the phase difference is configured to be $2\pi N$ where N is stated to be an integer and h is the cavity height (3.10) [65];

$$\Delta\phi = \phi - \pi - \frac{2\pi}{\lambda}2h = 2N\pi, \qquad N = 0,1,2 \tag{3.10}$$

3.3 Vector Network Analyser (VNA)

A Rohde & Schwarz ZVL Network analyser has been used to measure S-parameter results of the manufactured models.The specific model is capable of measuring the electromagnetic behaviour of the electrical networks connected with a frequency between 9kHz and 6GHz. This multi-functional equipment is used to measure various types of parameters mainly related to the power accepted or reflected by the AUT. Apart from the S-parameters Y and Z parameters could be visualised as well as the matching over a set of frequencies within the limitations could be represented either on the smith chart or a polar plot. It is crucial to establish a stable connection with a coaxial cable transferring the energy from the source to the antenna which could otherwise lead to inaccurate set of results. However the stability of the cable could be maintained with the aid of a calibration kit of Agilent 85052*D* where 3.5*mm* coax is used. The calibration process is carried out in 3 steps for a single port system. In this case the coaxial cable is connected to a short circuit load where the reflection coefficient $\Gamma = -1$ where impedance is zero giving a mismatch. The following calibration is done with an open circuit connection to the end of the coax where the reflection

Fig. 3.1 A capture of the Vector Network Analyzer with a coaxial connected to Port 1

coefficient attained is $\Gamma = +1$ resulting in a missmatch where impedance is infinity. Lastly a 50Ω load is connected to the coaxial cable for the perfect match where the reflection coefficient $\Gamma = 0$ and applying all the adjustments above to the VNA, full system calibration for precise measurements is achieved. The power of internal signal source is known to be $-10dBm$ ($0.0001Watts$). The vector network analyzer set up with a 50Ω coaxial cable and the calibration kit is illustrated in Figure 3.1.

3.4 Anechoic Chamber

Anechoic chamber is a specially designed room used to absorb the reflected electromagnetic waves and prevent waves interfering the region which is under test providing more accurate results which are equivalent to the system tested in free space. The antenna under test (AUT), is placed on a $\pm 180^{\circ}$ rotating arm along the azimuthal plane (H-plane). A transmitting antenna (R&S® HF906 Horn) is located at the far-field of the AUT approximately at a distance of $2.5m$ away from the AUT which are perfectly aligned to ensure line on sight

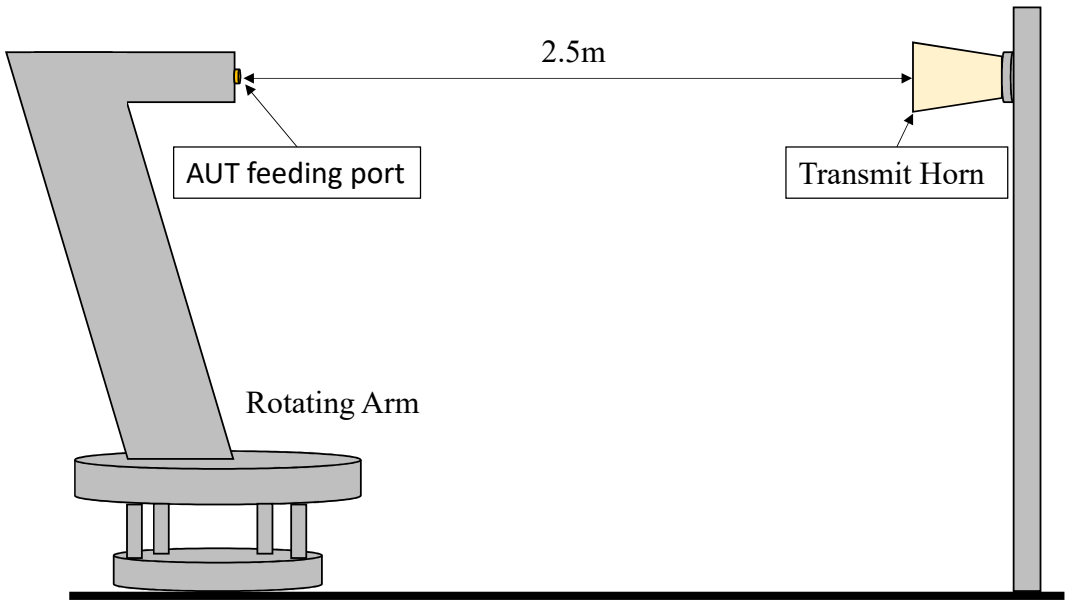

Fig. 3.2 Schematic set-up of the Anechoic chamber

propagation of the electromagnetic waves and prevent polarization diversity. The system is powered and the measurements are carried out with NSI 2000 R systems. The system set-up enables the user to generate 2D radiation patterns along the azimuth or elevation planes where the magnitude of power delivered within the antennas are attained by examining the scattering parameters $S21$ which is then plotted and analysed using Agilent Technologies E5071C ENA Series vector network analyser (VNA) which can support up to $20GHz$ frequency. Co-polar and cross polarization results can be determined by rotating the AUT from the origin along the elevation plane. A reference horn antenna (R&S® HF906 Horn) is used as the AUT where the scattering parameters (S21) have been plotted over a range of frequencies represented in Figure 3.3. The relative gain at each frequency is attained from the given data-sheet and corresponding magnitude of the S21 parameters are evaluated. Regarding the set of data collected with the reference antenna the results will be used to derive the gain of AUT using the equation where G corresponds to gain;

$$G_{AUT} = [(-S21_{Horn} + S21_{AUT}) + G_{Horn}] \tag{3.11}$$

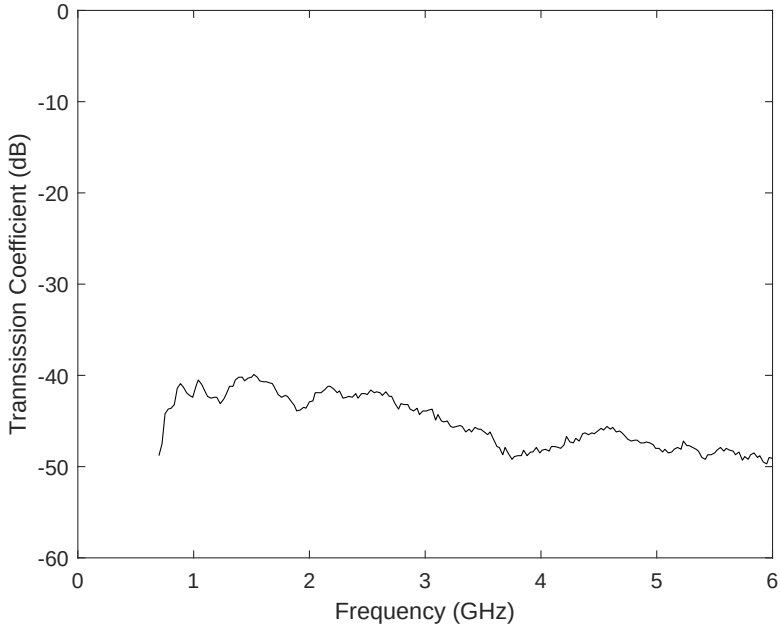

Fig. 3.3 Reference horn to horn antenna S21 transmission parameters over a frequency range of 6GHz

3.5 Initial Design and Software Configuration

At the initial stages of the project, an essential step was the validation of the results achieved with the simulation software CST Microwave Studio® for the reliability of the software simulation settings and parameter adjustments. Therefore regeneration of the simulation results provided in the publications [66, 67] has been carried out with CST Microwave Studio® which is a widely used simulation programme with features of 3D modelling, result and analysis of the electromagnetic propagation and properties of the waves radiated by the created structures. The structure is contained in a free space of a volume called the computational volume which is discretized into mesh cells of rectangular cubes with various sizes. The electric and magnetic fields within the unit cell were calculated where the accuracy of the results are strongly dependent on the size and amount of the meshcells existing in the computational volume. In order to achieve an accurate set of results within a reasonable time for the simulation to be completed, the smallest cell size has been adjusted deliberately where the maximum mesh step width is further enhanced, within local mesh properties, at the excitation and crucial regions of the model. In order to apply local mesh settings, a vacuum cuboid is created around the area of interest and the meshing within the region is maximised for increasing the accuracy of the results.

The 3D model is presented in Figure 3.4a, where a dipole antenna is placed over a metallic ground plane and coupled with a hairpin shaped structure placed along the y-axis. The hairpin shaped metal is fed with a transmission line which will produce a current on the strip and due to mutual coupling currents will be induced on the dipole and radiate. A coaxial as illustrated in Figure 3.4c is created with the aid of macros within the software where the permittivity of the materials used for inner and outer conductors as well as the length which has been adjusted to achieve a desired matching impedance of 50Ω. The meshing around the feeding port has been adjusted precisely to ensure the connection points of the discrete port are at the edges of the two metallic conductors. Occasionally the length of a discrete port influences the simulation results due to the inductance of the wire (port) which increase proportionally with the length of wire [79], therefore it is necessary to evaluate a

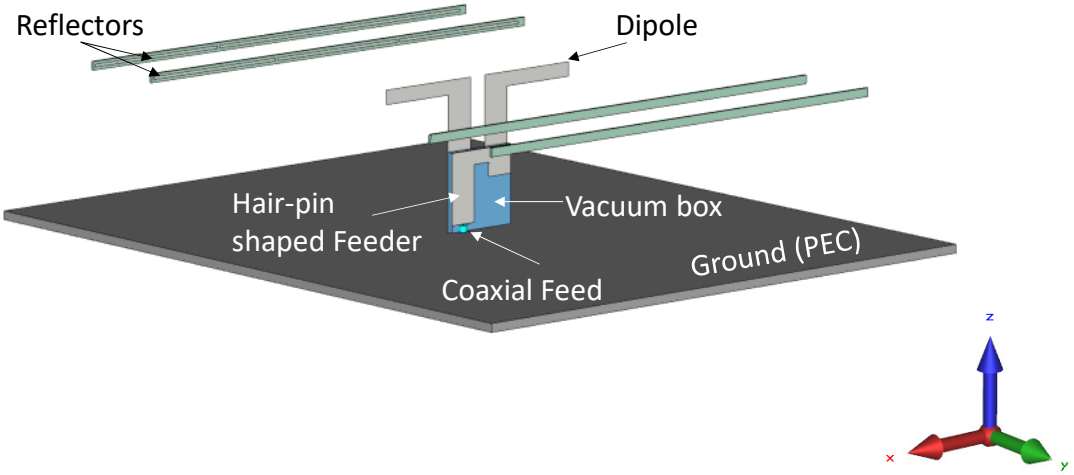

(a) Complete model representation in CST Microwave Studio®

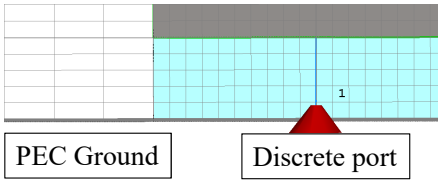

(b) Discrete port feed

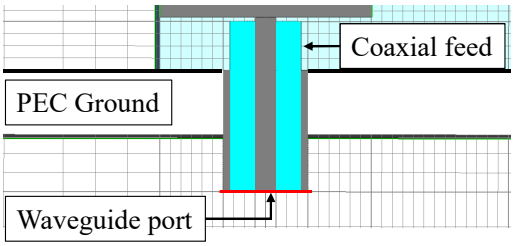

(c) Coaxial feed with waveguide port

Fig. 3.4 Regenerated Hairpin Coupled Dipole of [67] with FSR in CST Microwave Studio® for purpose of corroboration of results.

comparison between different methods of feeding mechanisms and the effects on the results. The reflectors which are perfectly aligned with the radiating dipole have a strong effect on focusing the radiation pattern towards the boresight z-direction where $\theta = 0^{\circ}$. For further improvement in the operational bandwidth, outer set of reflectors are also included in the design where the distance between the ground is set to be $\lambda/4$. This will generate an in-phase incident and reflected waves which will intensify the fields radiating boresight direction as discussed previously in the literature.

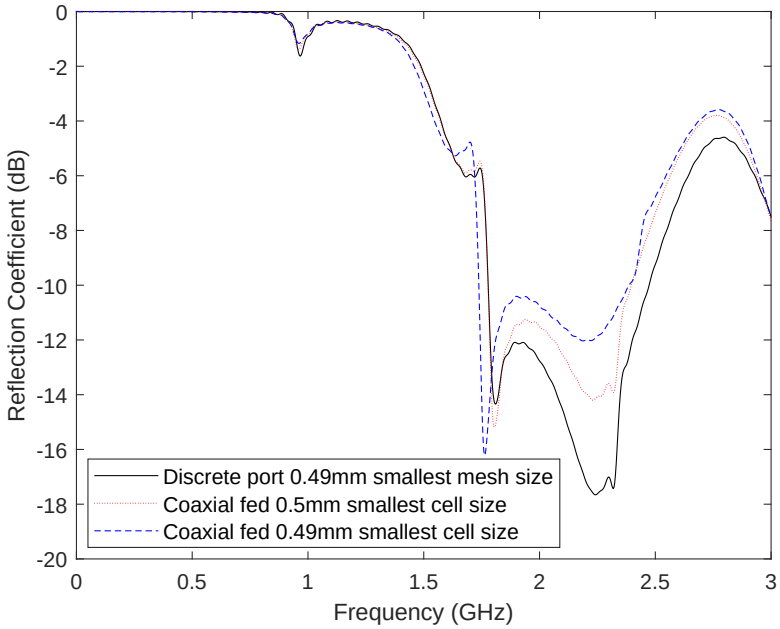

Fig. 3.5 Simulated S-parameters with mesh adjustment and port variations

A time domain transient solver, based on Finite Integration Technique, has been set up to analyse the power accepted by the antenna S11 parameters, surface currents as well as far-field radiation patterns. This technique enables perfect boundary approximation where the calculations within a meshcell are based on the geometry of the design rather than the edges of the cell. In addition to this, the density of meshing is increased within the critical areas of the model ie. at the edges and feeding points using multilevel subgridding scheme. Simulated S11 parameters with different mesh settings have been evaluated in Figure 3.5. According to the simulation results presented in [66], maximum operational bandwidth with a threshold level of -10dB was stated as 700MHz where maximum realized gain was calculated as 10.2dBi. Having a different mesh set up for the exact model some variation in the results are seen. However changing the feed type from a coaxial cable (waveguide feed) to a discrete port the effect on the results are comparatively infinitesimal, therefore discrete ports can be preferred with an accuracy adjustment of $-60dB$ to set the simulation run time threshold where the simulation will continue until the energy reaches the predefined value. It has been recommended by the software programme to use a lower threshold level

for larger frequency bands in order to provide enough amount of time for the programme to generate accurate results by aiming to minimise the fast Fourier and discrete Fourier transform limiting errors at the edge of the bounding box which is set to be $1/8$ wavelength away from the simulated model as default. Figure 3.6 illustrates the far-field radiation pattern directivity of the replicated model with a Cartesian representation at azimuthal plane where $\theta = 90^{\circ}$. The gain relative to the isotropic radiator achieved at the boresight where $\phi = 0^{\circ}$ can be stated as $10.2dBi$ with the original model respectively where a good corroboration between the original and regenerated simulation results have been accomplished proving the reliability of the applied simulation software settings used to generate results.

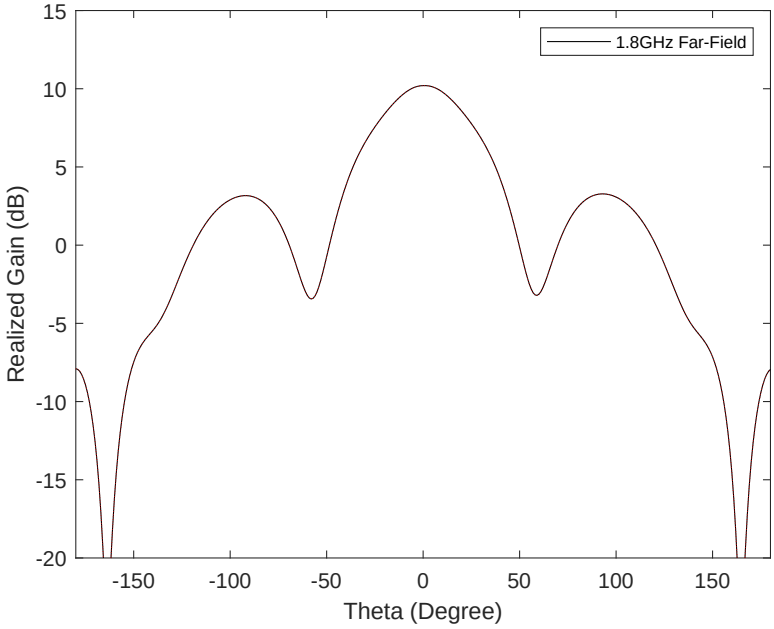

(a) Simulated Far-Field radiation pattern of regenerated model with an operating frequency of $1.8GHz$

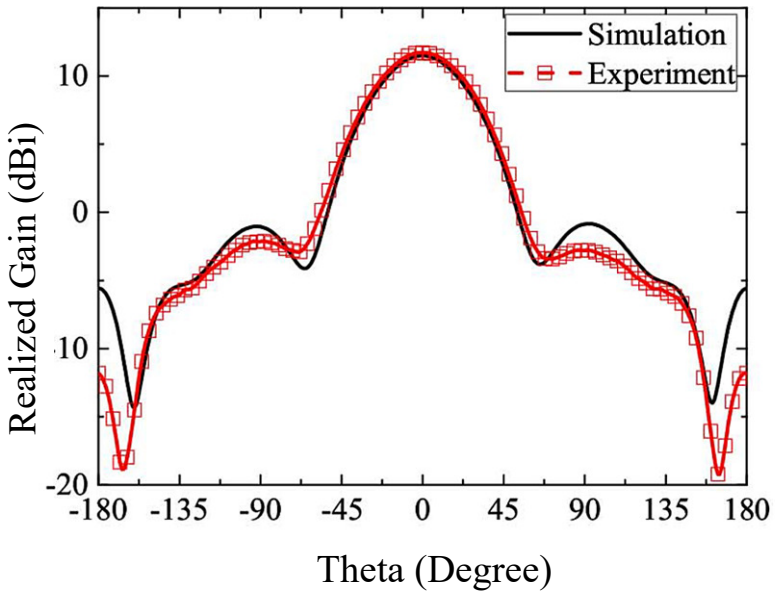

(b) Results achieved in [67]

Fig. 3.6 Comparison between simulation results achieved in CST Microwave Studio® and previously achieved results of Kim [67].

Chapter 4

High Gain Dipole Antenna with Tuned Parasitic Elements for Continuous Pattern Reconfiguration

Reconfigurability properties of the antennas have been investigated intensely over a decade due to the massive increase of the smart electronic devices connected to the everyday use of applications creating traffic and congestion within the available electromagnetic spectrum where wireless communication is carried out. Planar pattern reconfigurable antennas are of interest due to their compact design and low cost as well as producing high performance which is considered as a resolution to attain a good use of the spectrum and enhancing the overall system performance. There has been several techniques which are adopted as represented in [10, 11, 26, 29].Within this the contribution of parasitic strips on the radiation pattern by controlling the surface currents induced on the parasitics and the alignments relative to the radiating dipole will be investigated. 5 unit cell parasitic reflectors will be placed on each side of a ground plane as a starting point then the ground plane will be removed and the evaluation process for beam steering along E and H plane by including capacitors for changing the lengths of the total parasitic strip lengths. A prototype of a radiating dipole between 4 parasitic dipoles over a ground plane have been manufactured

and tested in the anechoic chamber where related field will be conducted at the end of the chapter.

4.1 A Radiating Dipole with Parasitic Strips

According to the literature previously reported in Section 2.2.3, it can be revealed that the currents induced on the parasitic elements placed around a radiating source, have a great impact on the E-field pattern of the structure. Therefore, the significance of understanding the contribution of parasitic elements is crucial. Consequently, previously modelled structure mentioned in Section 3.5 will be examined where the complexity of the model will be reduced for the ease of understanding. Complicated feed of the structure proposed in [67] results with an interference to the surface currents induced on the parasitics due to the capacitive coupling. Hence, the structure has been simplified to a model of a radiating dipole where the wavelength is calculated according to the relation where $c = \lambda f$ which is fed by a discrete port and two 5-unit cell parasitics placed at a distance of $\lambda/2$. The model of interest is illustrated in Figure 4.1. The elements are placed over a ground plane at a distance of $\lambda/4$, where the reflected waves will be in a 180° of phase shift which will constructively add to the radiated waves enhancing the gain as well as preventing radiation towards the undesired direction. The parasitic element unit cells are placed in free space with no substrate

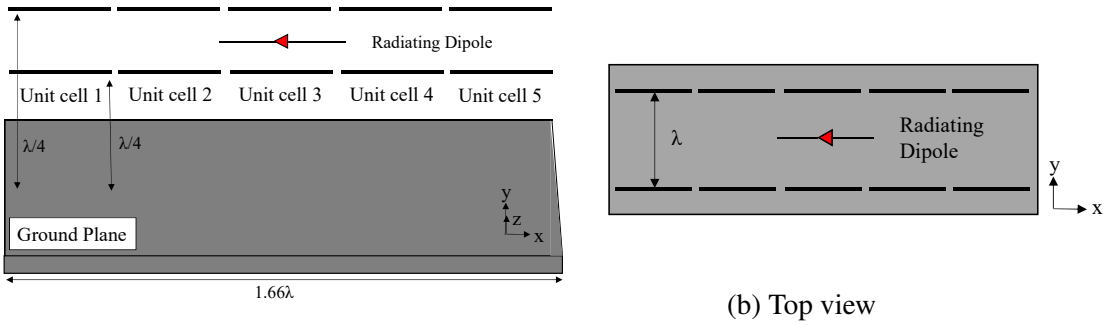

(a) Side view

(b) Top view

Fig. 4.1 Cross sections of the model in x-y-z and x-z planes where parasitics are placed over a relatively large ground (1.66λ *x* 1.66λ)

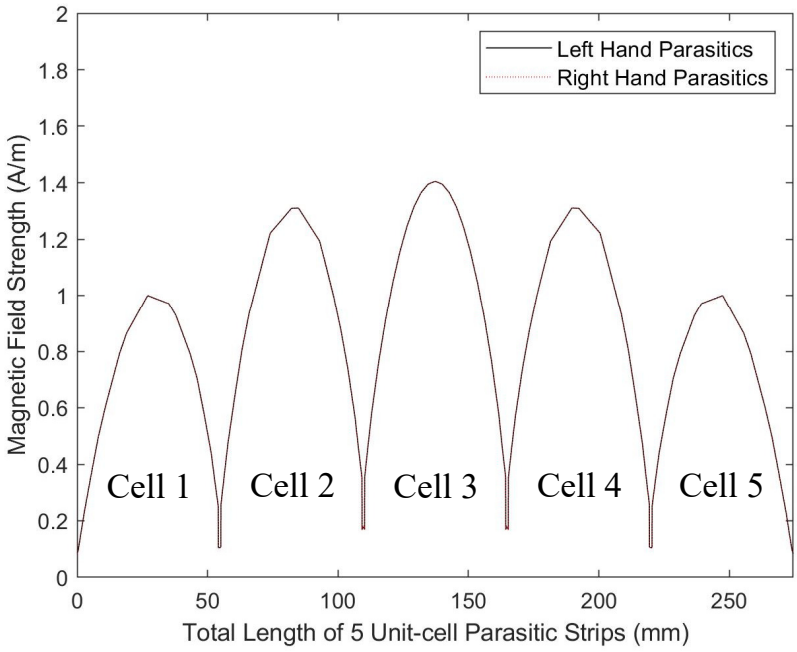

Fig. 4.2 Simulated magnetic field strength on 5 unit cell parasitic strips placed on either side of the radiating dipole over a ground illustrating complete symmetry

and modelled as PEC with zero thickness. The entire structure has been designed with a material of perfect electrical conductor (PEC) and no substrate has been used in order to generate a perfect environment for electromagnetic propagation excluding any substrate effects and any conductive material losses. The evaluation of understanding the contribution of the parasitic strips positioned in the near field of the radiating element can be carried out with investigating the surface current behaviour along the strips. The current behaviour is monitored by examining the magnetic field strength along the curves placed on the parasitic elements in the simulation programme CST Microwave Studio®.

As illustrated in Figure 4.2, the 5-unit cell parasitic length is represented with the x-axis where y-axis on this graph represents the magnitude of the magnetic field strength. It can be clearly observed that at the resonant frequency of $2GHz$ which was set initially for evaluation purposes, the magnetic field strength along the middle strip is higher due to the positioning of the strip which is next to the radiating dipole. This can be related to the positioning of the radiating dipole which is almost in line with the middle strip (Unit cell 3)

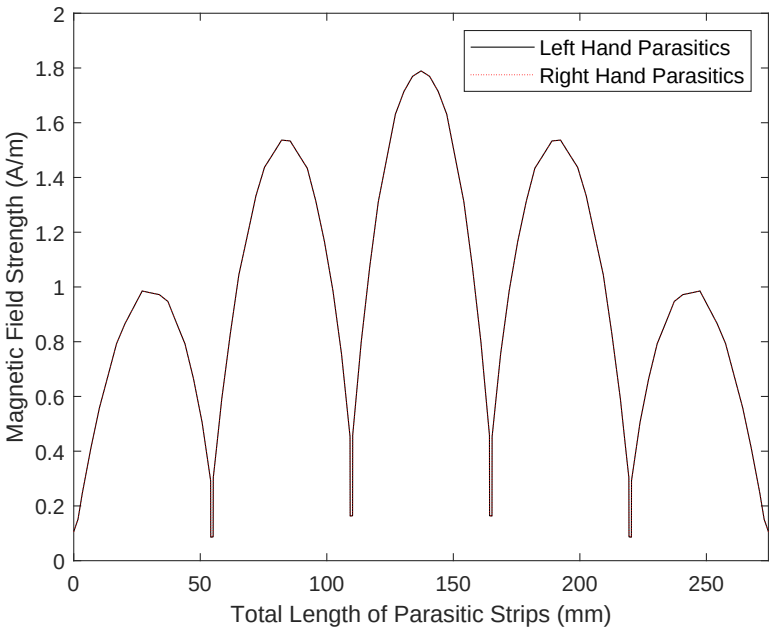

Fig. 4.3 Simulated magnetic field strength on the parasitic strips placed on either side of the perfectly aligned radiating dipole in free space no ground plane

as represented in Figure 4.1. For the parasitic strips which are not in line with the radiating dipole, the magnitude of the magnetic field strength is lower hence this is proportional to the magnitude of currents induced on the parasitics (H-field). The structure of interest is modelled completely symmetrical however the current behaviour along each parasitic strip LHS and RHS appears to be uneven. Further adjustments has been applied to the model where the ground plane has been removed and the radiating dipole has been transformed into a from of a wire strip with zero thickness which is perfectly aligned with the parasitic elements. The results are illustrated in Figure 4.3 where the peak magnitude of magnetic field strength is increased due to the perfect alignment of the parasitics and the radiating dipole.

4.1.1 Fabry Pérot initialization

In this section, the realization of the Fabry Pérot topology as discussed previously in Chapter 3 will be implemented for the purpose of achieving a smooth steering of the radiation pattern as well as further enhancing the gain of the conventional half wavelength dipole which is known

as 2.15dBi. Adjusting the distance between reflector sheet and partially reflecting surface the Fabry Pérot resonant condition can be attained with consecutive in-phase reflections where beam enhancement is observed [51]. Unlike the conventional methods an anti-resonant mode Fabry Pérot topology studied in [66] will be implemented since a high boresight radiation and beam steering capability is essential. The directivity at the boresight can be attained with Equation 3.9 which is illustrated in Chapter 3. As mentioned previously the cavity spacing, where in this chapter it has been generated with parasitics placed at either side of a radiating dipole, has a crucial effect on the radiation behaviour where the phase and the magnitude of the reflections which are formed within the cavity varies with the spacing. The two different modes of Fabry Pérot resonance [66, 67], are illustrated in Figure 4.4. As presented in the figure , it can be realized that with a shorter distance between the parasitics forming the cavity, the beam is enhanced towards the $\pm$x direction. However increasing the

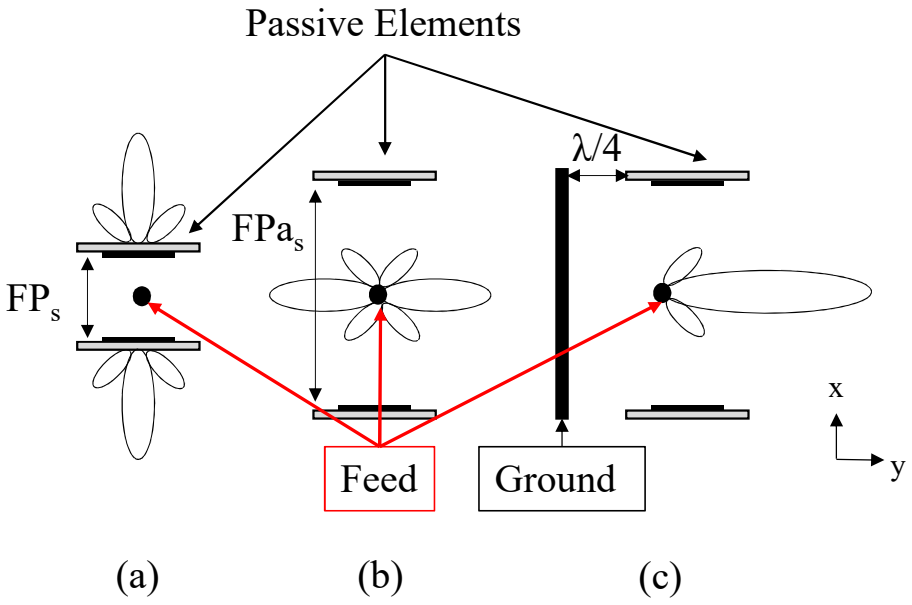

Fig. 4.4 A cross section of the Fabry-Pérot topology models with (a) resonant (FP_s) and (b) anti-resonant (FPa_s) mode spacings varied as well as (c) with a ground plane placed at a distance of $\lambda/4$ with (FPa_s) cavity spacing

distance between the parasitics the beam is reflected towards the ±y direction. The Fabry Pérot resonance and anti-resonance mode can be calculated using (4.1) [66] ;

$$FP_s = \frac{c}{2f}\left(\frac{\phi_h + \phi_l}{2\pi} + M\right) \tag{4.1}$$

where c, ϕ_h and ϕ_l represents the speed of light, higher and lower parasitic reflection phase respectively where M is an integer. The anti-resonance condition can be achieved using Equation (4.2) ;

$$FPa_s = \frac{c}{2f}\left(\frac{\phi_h + \phi_l + \pi}{2\pi} + N\right) \tag{4.2}$$

where N represents an integer number as well as π being the 180° phase shift to switch from the resonant to anti-resonant mode. According to the eqution illustrated above the distances for both modes are calculated to be $FP_s = \lambda/2$ and $FPa_s = \lambda$ respectively. Through the upcoming Chapters 5 & 6, there will be further discussions about the crucial effect of parasitic spacing on the steering angle and the gain enhancement where further adjustments and improvements will be carried out.

4.2 Evaluation of the Design

At the beginning of Chapter 4, it can be observed that the antenna structure as well as as the lengths of the parasitic strips have been modified according to [66, 67]. However in this section the construction of the model will be carried out with wavelength units. A well-known wave equation is used to determine the wavelength of the antenna according to the operating frequency that can be used to calculate the electrical size of the antenna 4.3.

$$c = \lambda f \tag{4.3}$$

where c is the speed of light, λ is the wavelength and f stands for the operating frequency of the structure. Having the dimensions in wavelength units (λ) would enable the structure to be modified for any frequency range conveniently. Initially the resonant frequency of the design has been allocated as $1.85GHz$ which is widely used in current wireless communication networks. For the desired operating frequency the wavelength is calculated to be $\lambda = 0.162m$.

4.2.1 Two lambda long parasitics

In this section the model has been changed to retain a accessible structure where the lengths are designed to be represented with wavelength (λ) units which can be adjusted for any desired frequency conveniently . In spite of not changing the overall length of the parasitic lengths, $\lambda/4$ unit parasitic strips are used to generate the 2λ long complete reflectors on each side of the radiating dipole. Regarding to the literature studied previously about the anti-

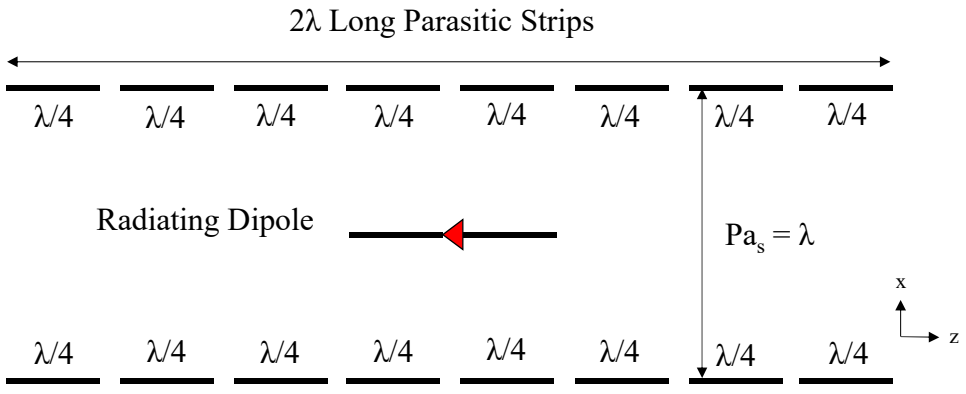

Fig. 4.5 Top view of the model in free space (no ground) with total length of 2λ long parasitc strips formed of $\lambda/4$ strips

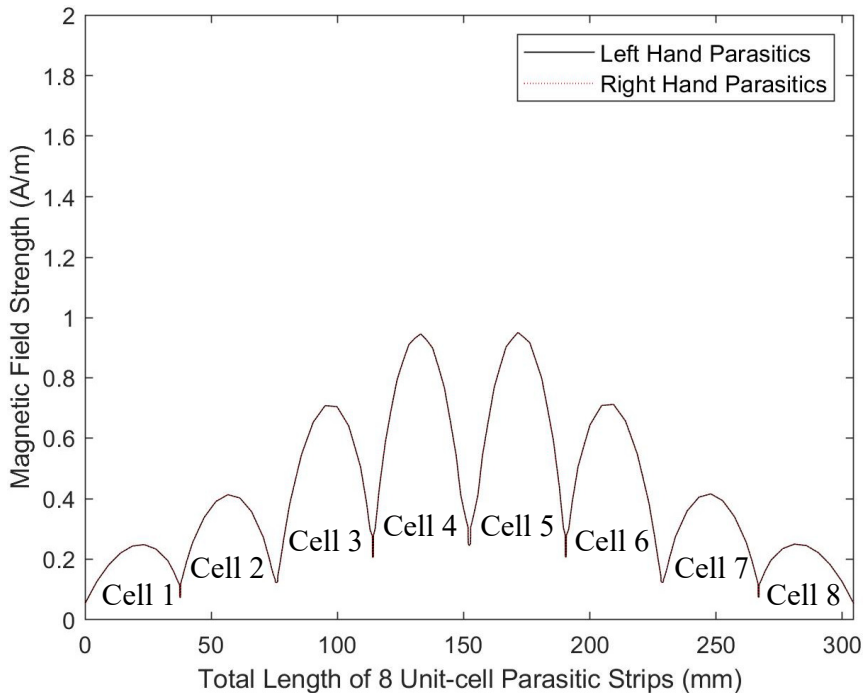

Fig. 4.6 Simulated magnetic field strength over 2λ parasitic strips placed on either side of the radiating strip dipole in free space

resonance mode of the Fabry-Pérot cavity, distance between the parallel reflectors have been set to a length of a wavelength (λ). According to this approach 4 dipoles with conducting arm lengths of $\lambda/4$ have been established as displayed in Figure 4.5, Considering the new structure represented in Figure 4.5, the induced currents on each side of the parasitics, which are perfectly aligned with the radiating dipole is illustrated in Figure 4.6. According to the figure a significant reduction of the current magnitude is observed. This can be related to the strip lengths being electrically short resonating at a higer frequency related to the equation provided in (4.3). Since the middle trips have been explicitly placed next to the radiating half wave dipole, it can be seen that the middle strips have the peak magnitude of current compared to the outermost strips. With the relevant current distribution along the parasitic strips the contribution on the radiation pattern of the conventional half wave dipole position in the centre of the parasitics are illustrated in Figure 4.7 with a far-field polar representation. The far-field behaviour of a half wave dipole is a well known doughnut shape with a gain of $2.15dBi$ [5]. Since the unit cells of the parasitic strips are not connected and the lengths are

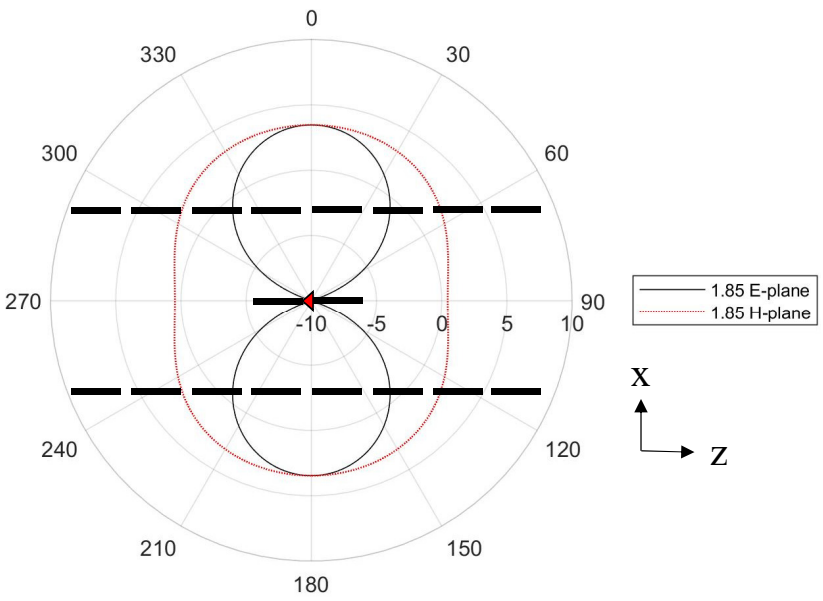

Fig. 4.7 Simulated realized elevation and azimuthal plane far-field patterns with 2λ long parasitics at $1.85GHz$ frequency

smaller than half of a wavelength, also considering the current behaviour along the parasitics represented in Figure 4.6, it can assumed that at this operating frequency of $1.85GHz$ the parasitics will not have a crucial effect on the far-field. Considering Figure 4.7 the elevation (E-plane; $\phi = 0$) and azimuthal (H-plane; $\theta = 90°$) are illustrated and clearly observed that the far-field pattern is almost omnidirectional where a slight increase in the gain $3.45dBi$ is achieved towards the parasitic strips along the x-axis. This can be related to Yagi-Uda antenna basics where the directors are made smaller in length compared to the radiating element to become capacitive and direct the beam towards the end-fire where the negligible effect is seen with the introduced model. Consequently it can be perceived that the lengths of parasitic strips can be neglected when they are much smaller than the electrical length of the resonator antenna where typical behaviour of the resonator antenna can be distinguished.

4.2.2 Introducing reactive impedance to the model

As studied in the literature review, reactive impedances have a big effect on changing the current distribution along conducting or radiating elements hence changing the behaviour of the radiation field at the far-field [22]. Therefore, recalling the results obtained in the previous section (4.2.1) where reflectors are formed with 4 equally spaced dipole length metallic strips, with addition of reactive impedance in between each of the gaps connecting the strips of Figure 4.5, a high impedance surface behaviour can be achieved. In this particular section capacitors as lumped elements will be introduced to the model which will be connected between the gaps of $\lambda/4$ parasitic strips where depending on the value of the capacitance the impedance in between strips will be varied. As a consequence either the strips will be connected to each other or will be disconnected and neglected due to the outcomes of section (4.2.1). The value of capacitance is calculated with a set of fundamental electrical impedance rules. The complex form of impedance can be stated with (4.4),

$$Z = R + jX \tag{4.4}$$

where R is the real and jX can be noticed as the imaginary part of the electrical impedance also known as the reactance. Reactance can be either capacitive or inductive which can be defined as,

$$Z_c = \frac{1}{j\omega C} \tag{4.5}$$

$$Z_L = j\omega L \tag{4.6}$$

where ω corresponds to the angular frequency known as $\omega = 2\pi f$. With respect to the design specifications of the model where the operating frequency was chosen to be $1.85GHz$ as mentioned previously. Using the equations listed above, a capacitance of $C = 1.178pF$ is attained where the impedance of the antenna was set to be 73Ω and a high impedance is accepted to be at least 3 times larger. Since the impedance of the element is inversely proportional with the capacitance (4.5), the capacitance values higher than $1.178pF$, would react as a short circuit. This will allow the current flow between two $\lambda/4$ strips generating a connection and increasing the travelling path of the induced currents hence increasing the electrical length. However reducing the capacitance would increase the impedance and hence generate a barrier with an insulator behaviour where the currents will be limited within a single $\lambda/4$ strip. The model of interest which has been discussed in section (4.2.1) has been modified and tested by applying lumped elements with values of $3pF$ in between the strips starting from the middle two strips on each side and gradually adding until all the strips are connected to increase the overall length of the parasitics by allowing the flow of current

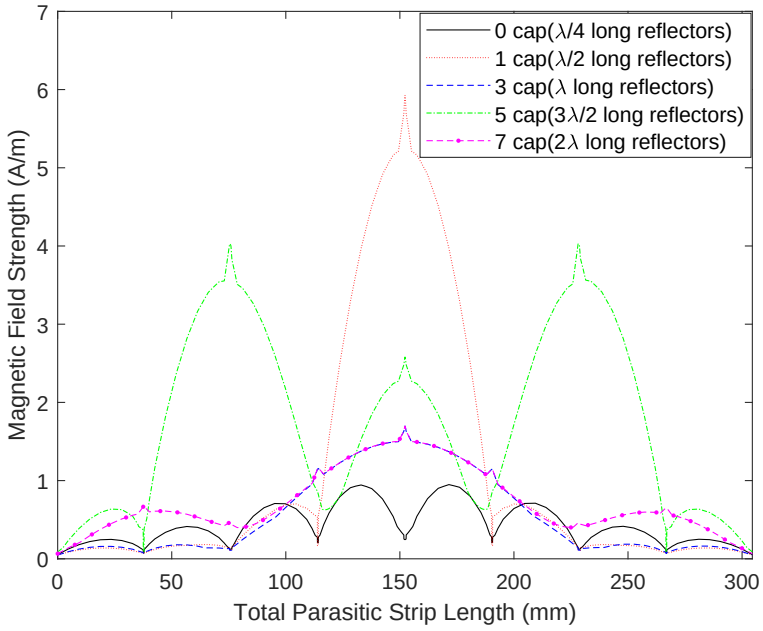

Fig. 4.8 Simulated magnetic field strength over variable parasitic lengths $\lambda/4 - 2\lambda$ parasitic strips placed on either side of the radiating dipole by including $3pF$ capacitors between strips

between the adjacent strips. Current distribution along the parasitic strips are illustrated in Figure 4.8 with different lengths of strips. As stated in the chart, parasitic strip lengths are varied between $\lambda/4$ and 2λ. The connection points of the components are generating the spikes due to the impedance differences between the components and the strips which is created by the simulation software which does not contribute with the radiation pattern and can be neglected. The parasitic strip unit cells can be identified with the current lobes created when no capacitors are included in the design. It can be clearly observed that with different parasitic strip lengths the current behaviour is varied where $\lambda/2$ and $3\lambda/2$ lengths have a considerably higher current magnitude which can be related to the current distribution of a linear wire antenna [5]. Further analysis will be carried out throughout this section to maintain a complete understanding of contribution of the parasitics lengths and induced currents to the radiation pattern in the far-field. Figure 4.9 is a polar plot illustration of the constructed model with different parasitic lengths as mentioned previously. Regarding to the far-field polar plots, it can be observed that the parasitic strips forming a $\lambda/2$ length

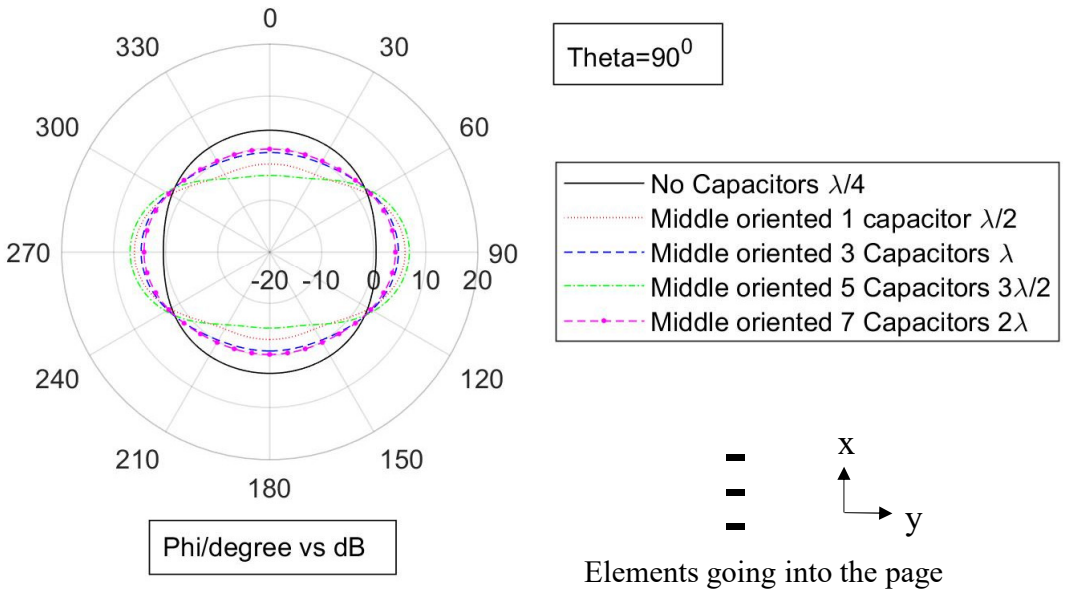

Fig. 4.9 Simulated realized far-field radiation patterns with various parasitic lengths at the resonant frequency of $1.85GHz$

Lumped Elements	Reflector Length	Realized Gain (dBi)	Beam Direction	$3dB$ width
1	$\lambda/2$	6.01	90°	51.6°
3	λ	4.72	90°	75.3°
5	$3\lambda/2$	6.80	90°	52.8°
7	2λ	4.16	90°	88.2°

Table 4.1 Comparison between the effects on far-field properties of parasitics with various sizes where $3pF$ capacitors are added symmetrically starting from the middle gap

which is perfectly aligned with the radiating dipole has a higher induced current compared to the longer parasitics and the contribution is proportional. Regarding to the theory of the current distribution along a linear wire [5], it can be noticed that when the total wire length is adjusted to be either $\lambda/2$ and $3\lambda/2$, the current magnitude is significantly higher due to the phase change of the currents propagating along the strips with $\lambda/4$ intervals where voltage is known as the maximum at the edges of the wire as discussed in [5]. However comparably low current distribution is obtained with parasitic lengths of λ and 2λ due to the cancellation of currents moving along the strips at specific lengths. According to the anti-resonant mode of Fabry Pérot where the spacing of the parasitics Pa_s is λ, the initial radiation pattern radiating towards $\pm$ x-direction ($\phi = 0, 180°$) is reflected and hence the main lobes are directing towards the $\pm$ y-direction ($\phi = 90, 270°$). This change contributes to a 90° beam switching in the Azimuth (H-plane) from $\phi = 0°$ to ($\phi = 90, 270°$). The relative far-field radiation results with different parasitic lengths are illustrated in Table 4.1. With a length of $\lambda/2$ and $3\lambda/2$ where high current magnitude is initiated on parasitics a more directive pattern is achieved with a peak realised gain of $6.80dBi$ where the contribution is lower with other cases which can be clearly seen with the realized gain magnitude which is almost $2dB$ and higher angular beam width. Realizing the effects on the far-field radiation patterns with different parasitic lengths as illustrated above, three distinctive approaches are generated.

1. Achieving beam steering in the elevation plane (E-plane) where the model of interest is illustrated in Figure 4.10. High capacitance will be used to allow flow of currents through the strips where the capacitors will be included at the gaps starting from

one end of the parasitics symmetrically at both sides. Due to such configurations on parasitics with different lengths, beam steering at the E-plane is expected to be accomplished.

2. According to the previous analysis about the currents generated on curves, capacitors will be included in the middle two strips as illustrated in Figure 4.12. The capacitance will be varied between $0.1pF$ and $3pF$ examining the current behaviour on the parasitics. Regarding to outcomes of the analysis, beam steering with $\lambda/2$ strips as well as 2λ will be illustrated.

3. Since the $\lambda/2$ length parasitics have contributed in an efficient way with the radiation pattern along the azimuth (H-plane), the structure will be renovated as illustrated in Figure 4.17 to generate a more compact design by removing the excessive parasitics. Capacitor values will be varied in order to control the current behaviour on $\lambda/2$ length strips and a beam steering along the H-plane is targeted.

4.3 Beam Steering along E-Plane (Y-Z plane)

The figure of interest is illustrated in Figure 4.10. The inclusion of the ground plane with dimensions of (2λ x λ), at a distance of $\lambda/4$, would further enhance the gain towards the boresight as discussed previously and back radiation to an undesired direction is minimised. As explained in the previous section, the parasitics are formed of 8, $\lambda/4$ conductor strips with an overall length of 2λ. The length of parasitic strips are increased in z-direction starting from one end and allocating $3pF$ capacitors in each gap configuring the overall length of the parasitics where the parasitic spacing Pa_s is kept constant.

Relative radiation pattern plots are illustrated in Figure 4.11. Analysing the results it can be concluded that, with a capacitor placed on the furthermost strips forming a $\lambda/2$ length the magnetic field strength increases due to its electrically resonating length. Hence the radiation is towards the -z-direction along the elevation plane resulting in a 11° beam steering with a realised gain of $8.73dBi$. However increasing the lengths of the parasitic elements,

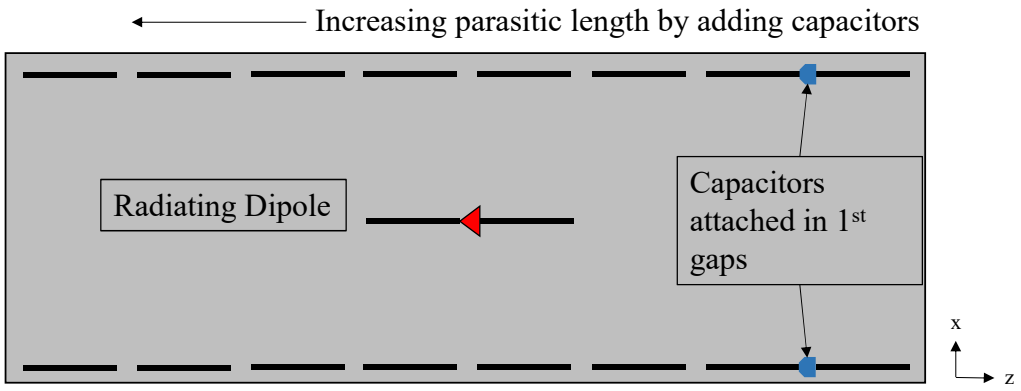

Fig. 4.10 Top view of the model over a ground plane of dimensions ($2\lambda\ x\ \lambda$) with $3pF$ capacitors are included in gaps between $\lambda/4$ strips

different current behaviour is attained where the steering angle at the -z-direction along the elevation plane is reconfigured to 5°. Further increasing the lengths by connecting the strips together with $3pF$ capacitors switched the direction of propagation where 10° and 7°pattern

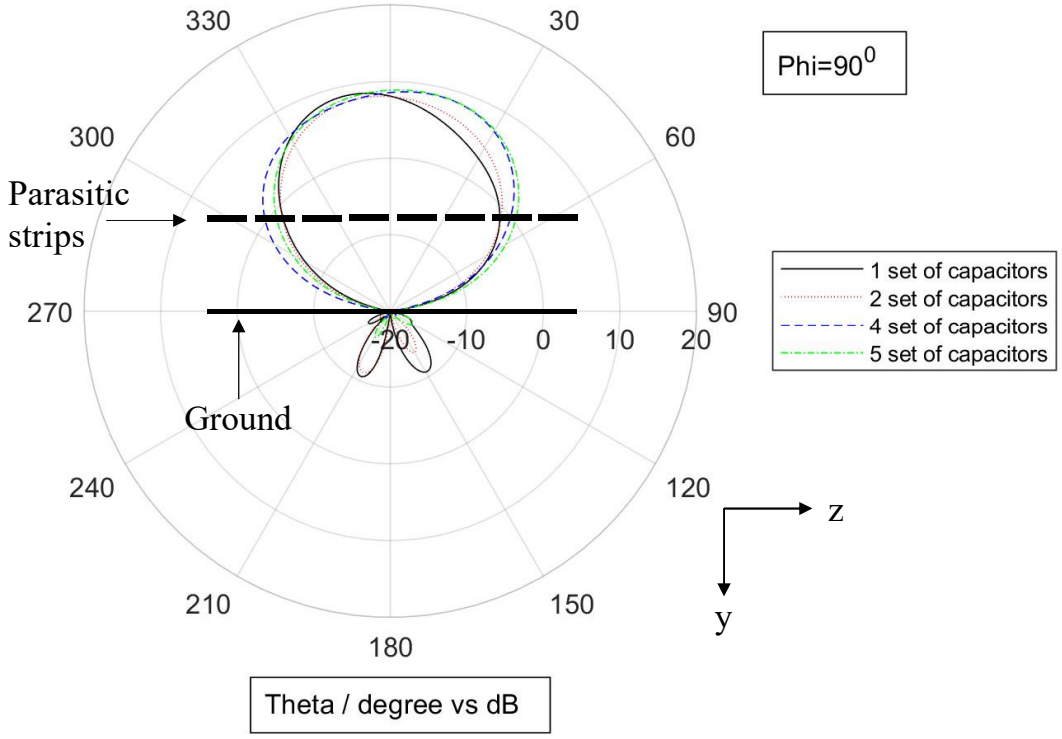

Fig. 4.11 Simulated realized E-plane gain pattern with $3pF$ capacitors included in 1 to 5 gaps symmetricallyat the resonant frequency of $1.85GHz$

reconfiguration is achieved at the z-direction and the main lobe direction can be denoted as 350° and 353° respectively. A relatively high gain with a minimum of $8.11dBi$ is achieved with different configurations where beam steering is attained along the elevation plane. The peak boresight radiation at $\theta = 0°$ is achieved with full length of parasitics 2λ with a realized gain of $9.39dBi$. It has been proved that by the inclusion of low impedance capacitors within the gaps symmetrically along the z-axis gradually increasing the total length of the parasitics, the pattern reconfigurability along the elevation plane (E-plane) where $\phi = 90°$ is possible with a reasonably high gain.

4.4 Beam Steering along H-plane (X-Y plane)

Regarding the previously discussed results about the current distribution along the parasitics it can be observed that maximum magnetic field strength has been obtained with the middle two strips which are perfectly aligned with the radiating half wave dipole. As a consequence, in this part capacitors will be allocated within these strips creating a $\lambda/2$ length parasitic strips which are positioned $\lambda/2$ away from the radiating element which is illustrated in Figure 4.12. The magnetic field strength over a full length of parasitic strips is monitored in Figure 4.13 where various capacitor values have been implemented to investigate the propagation of

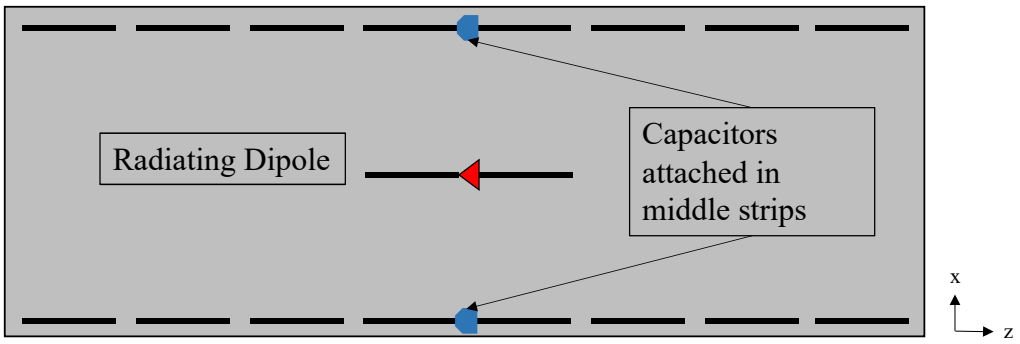

Fig. 4.12 Top view of the model over a ground plane of dimensions (2λ x λ) with various capacitor values $0.1 - 1.2pF$ capacitors are included in gaps between $\lambda/4$ strips

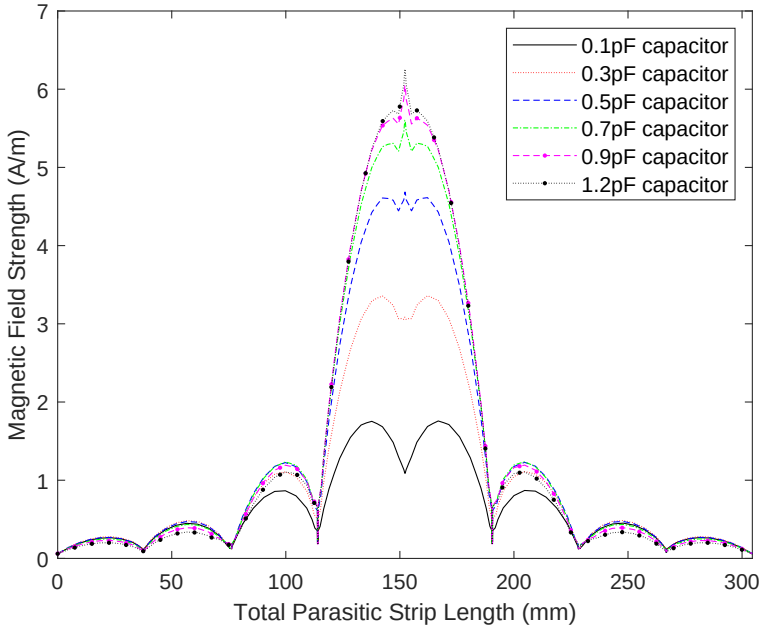

Fig. 4.13 Simulated magnetic field strength with various capacitor values implemented between middle strips at the resonant frequency of $1.85GHz$

currents along the strips. The appropriate value for the capacitance to completely short circuit hence connecting the strips have been calculated using Equations (4.4) and (4.5) as discussed previously. Since the minimum and maximum values of capacitances are previously calculated in section (4.2.2) for a complete open circuit and short circuit modes, the effect of capacitances within the constraints are represented in Figure 4.13. As illustrated in the figure, the capacitor values are varied between $0.1pF$ and $1.2pF$ where the calculated value is determined to be $C = 1.178pF$. The flow of currents along the parasitics have been altered with the inclusion of different values of capacitance. With a $0.1pF$ of capacitance the lowest magnitude of current has been attained due to the capacitor behaving as an insulator where flow of current within the strips have been limited. However these results with $0.1pF$ capacitor values are still higher than the results with no capacitors connected between the strips which is illustrated in Figure 4.9. This is due to the leakage of currents along the strips which will lead to a positive effect on the steering angle. Increasing the values of

capacitances decreases the impedance which can be observed with Equation 4.5 and hence more current is allowed to pass through the lumped element and create a short circuit in between the strips. As a result increasing the amount of capacitance increases the length of the strip form $\lambda/4$ to $\lambda/2$ effecting the behaviour of the far-field.

4.4.1 Maximum beam steering with one set of capacitors in middle strips

In this section of the chapter the maximum beam steering possibility using different values of capacitances to control the current behaviour separately along the parasitics will be investigated. A maximum beam steering with such structure illustrated in Figure 4.12 can be achieved by short circuiting the strips on one side resulting in a behaviour of a reflector with a length of $\lambda/2$ and open circuiting with higher impedance where the majority of currents are suppressed within the $\lambda/4$ length parasitic strips. Open circuiting by minimizing the capacitance in between the strips will diminish the effects of that parasitic due to minute amount of current induced on the strips causing them to become invisible set of strips at the specified frequency which is $1.85GHz$. The present structure is configured such that the open circuit parasitics are achieved with $0.1pF$ capacitance and $3pF$ capacitance has been included in between the parasitic strips for the short circuited side respectively. The model illustrated in Figure 4.12 is considered where the parasitic strips along the x-direction have been open circuited. Correspondingly the strips positioned at -x-direction is short circuited by addition of $3pF$ capacitors. Generated results are displayed in Figure 4.14 where xy-axis is examined known as the Azimuth (H-plane) which is compared against the two short circuited parasitics. The far-field realized gain patterns in polar form at the angle of $\theta = 90^\circ$ scanning through ϕ is illustrated. It can be clearly observed that with the implementation of $3pF$ capacitors, since the length of $\lambda/2$ is achieved and it is placed a distance $P_s = \lambda/2$ away from the radiating dipole the radiation towards the reflectors have been reflected towards the boresight direction at the angle of $\theta = 0^\circ$. A realised gain of 8.66dB is achieved with a half wave parasitic strip. However open circuiting one side of the parasitics hence reducing the

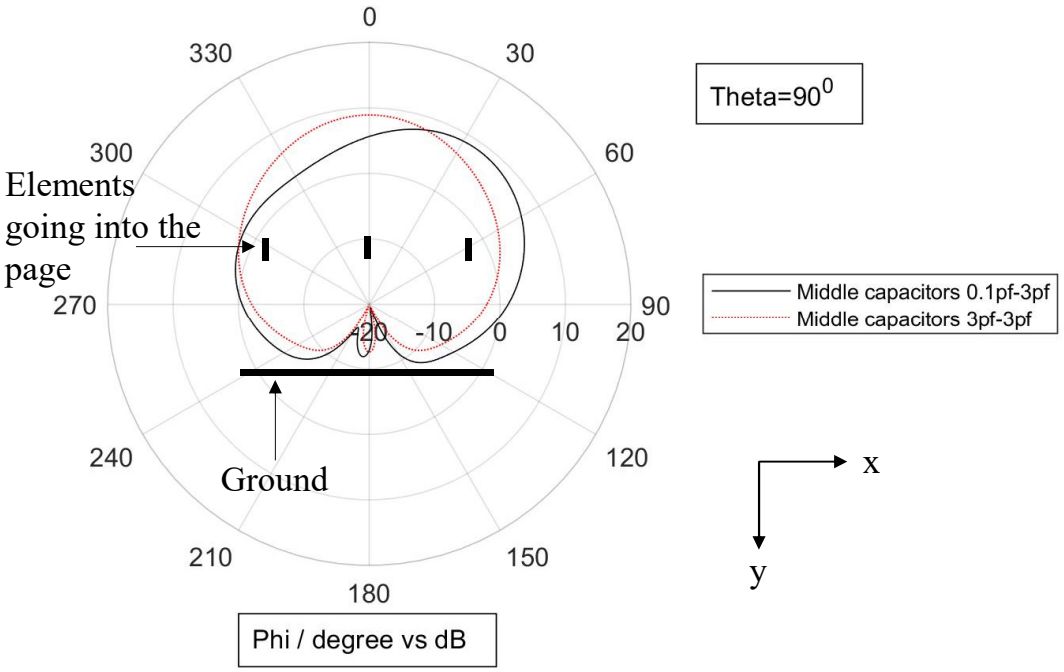

Fig. 4.14 Simulated realized far-field gain patterns with capacitors placed in between middle strips forming $\lambda/2$ parasitic length for maximum beam steering along the azimuth plane at the resonant frequency of $1.85GHz$

parasitic length to $\lambda/4$, it is clearly seen that the pattern is reflected by the $\lambda/2$ length strip along the azimuth plane towards the open circuit side without causing a significant decrease in the main lobe magnitude. A realized gain of $8.83dBi$ is achieved with an angle of 34° at x-direction.

4.4.2 Maximum beam steering full length parasitics 2λ

In this section, 7 sets of capacitors have been installed in between the strips of the structure displayed in Figure 4.12 connecting all the strips where full length of parasitics 2λ has been initiated. With respect to the previous section (4.4.1), a full parasitic length has been achieved with short circuiting the parasitic strips using $C = 3pF$ and to eliminate the effect of the parasitics a low capacitance of $0.1pF$ has been used to increase the impedance between the strips. Revealing the simulation results illustrated in Figure 4.16, with a full length

parasitics 2λ where $3pF$ capacitors included in between the strips, beam is directed towards the boresight with a realized gain of $9.4dBi$ which is reasonably high gain for such structure where only a single radiating element (half wave dipole) is used. However reducing the capacitance to $C = 0.1pF$ the flow of currents are altered and the magnetic field strength is reduced along the parasitics. The relative current distribution represented with magnetic field strength along the parasitics are illustrated in Figure 4.15. Revealing the figure it can be seen that, the short circuited parasitics with full length has a lower magnetic field strength compared to the opposite reflectors where the capacitance between the strips are reduced. As explained previously, the currents along the 2λ length parasitics cancel due to the propagation of currents with such electrical length of metallic conductor resulting in a lower magnitude. However on the other set of parasitics with $0.1pF$ capacitors, the induced currents are illustrating an open circuit behaviour where each lobe represents the magnetic field strength at each individual parasitic strip. Comparing the curves represented in Figure 4.15, it can be detected that the magnetic field strength along the parasitics with

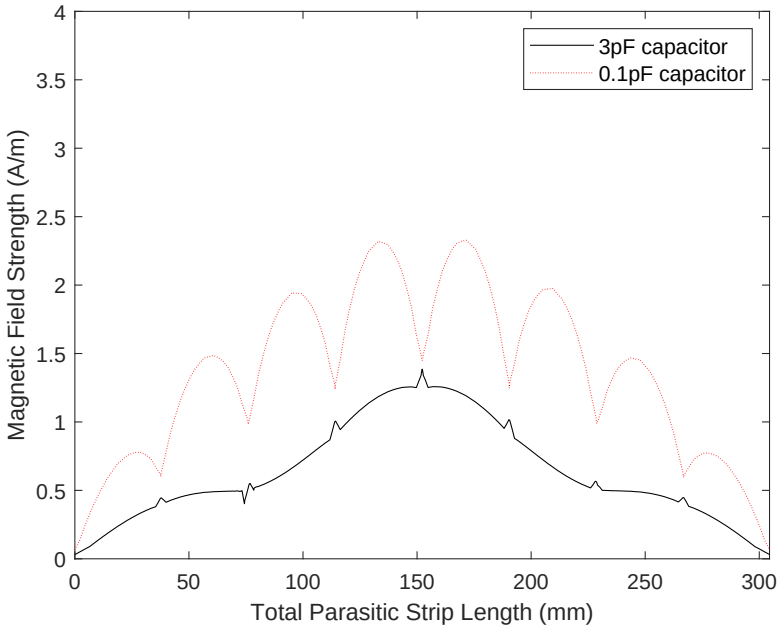

Fig. 4.15 Simulated magnetic field strength along the parasitic strips with $0.1pF$ and $3pF$ capacitors values are implemented in full length of parasitics

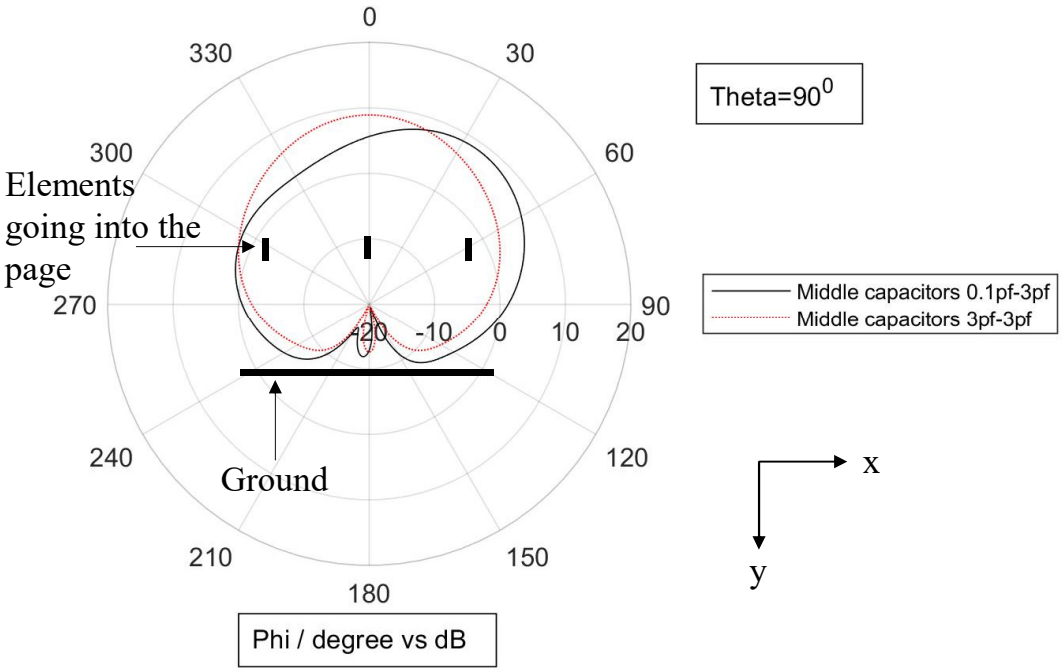

Fig. 4.16 Simulated realized far-field gain patterns with capacitors placed in between all strips forming 2λ parasitic length for maximum beam steering along the azimuth plane at the resonant frequency of $1.85GHz$

lower capacitances included between the strips are higher than the short circuit side where $3pF$ capacitors are used. This can be related to the leakage of currents between the strips since $0.1pF$ capacitors are used and there will be some current travelling between the strips. Regarding the discussions made above the simulated realized gain is illustrated in Figure 4.16. For the short circuit case for both sides where $3pF$ capacitors are included, it is observed that the beam is directed towards the boresight $\theta = 0^\circ$ with a realized gain of $9.4dBi$. Reducing the capacitance to $0.1pF$ on the RHS parasitics, the radiation pattern is reconfigured towards the x-direction with an angle of 24°. The main lobe magnitude defining the realized gain at the specific angle is observed to be $9.04dBi$. Evaluating the results in Figure 4.15 and 4.16, it can be observed that, having a full length of parasitics 2λ, the currents induced on the strips do cancel out and having a smaller magnitude compared to the opposite side the beam is reflected towards the short circuited side which is x-direction along the azimuth (H-plane). Comparing the results achieved with a $\lambda/2$ and 2λ long reflectors the simulated steering

angles do not have a major difference. The results reflects that increasing the lengths of the parasitic strips does not have a positive contribution to the beam steering angle therefore shorter parasitic length will be used for further evaluation in order to achieve less bulky structure.

4.5 Beam Steering Using Planar Parasitic Array of Dipoles

Since it is proved in the previous section that beam steering angle is not proportional to the lengths of the parasitics, further modification has been applied and excessive length of parasitics are eliminated as illustrated in Figure 4.17. The length of parasitic strips are reduced and positioned at a distance of $\lambda/2$ away from the radiating dipole. The capacitance between the strips will be altered to control the flow of current between the strips. As evaluated previously, one side of the parasitics will be short circuited with a capacitance of $3pF$ and the capacitance between the parasitic strip positioned on the opposite side will be adjusted to control the beam over a set of angles. The set up can be related to [22], where the parasitics are aligned on a planar axis (x-axis). The capacitance between the parasitic strips, positioned at the (+x) side where the radiating element is considered as origin, will be varied between $0.1pF$ and $3pF$ respectively. The current behaviour over the

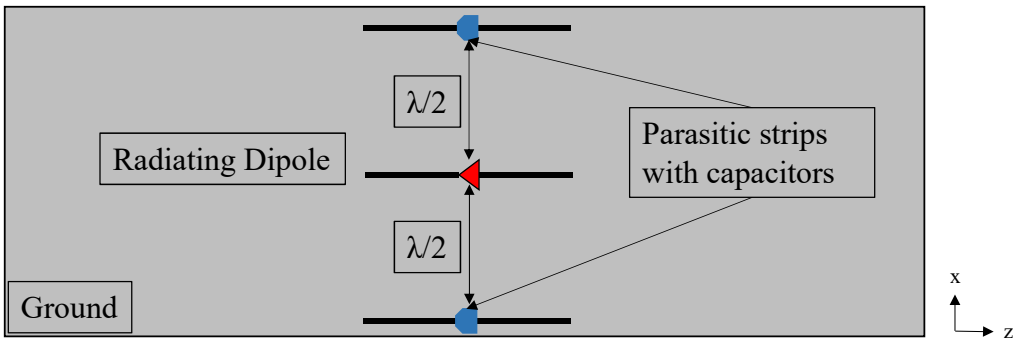

Fig. 4.17 Top view of the model over a ground plane with capacitors are included in gaps between the $\lambda/2$ parasitic strips

length of parasitics will be monitored with different capacitances between the strips where the current distribution within the strips will be altered in order to explore the possibilities of continuous beam steering feature. Different capacitor values with realized gain main lobe magnitudes and the steering angle of the radiation pattern are illustrated in Table 4.2. Evaluating the set of results contained in the table represented below, it is observed that a maximum of 44° has been achieved, towards the x-direction where capacitance is varied, along the azimuth plane with a realized gain of $7.04dBi$. However it is investigated that the increase in capacitance contributes with the radiation pattern proportionally. A trade off between the steering angle and the main lobe magnitude is observed. Lower capacitance $0.1pF$ cause a lower steering angle with a higher magnitude of realized gain and enhancing the capacitance hence allowing more current flow within the parasitic strips increase the steering angle decreasing the main lobe magnitude. The current behaviour along the parasitic strips with lengths of $\lambda/2$ is illustrated in Figure 4.18. The capacitance between the parasitic located in the RHS x-direction of the radiating dipole has been varied between $0.1pF$ and $3pF$ altering the flow of current between each unit cell of parasitic elements. Analysing the magnetic field strength along the curves, the contribution to the radiation pattern and steering angle could be observed. Revealing the results shown in Table 4.2 and Figure 4.18 and 4.19, it is seen that with a lower capacitance where a higher impedance is achieved within the strips, the flow of current has been minimised. As discussed previously the resonant length of a perfect electrical wire is determined to be $\lambda/2$. Since the length of the parasitic has been

Capacitance (pF)	Realized Gain (dBi)	Beam Steering Angle	Angular Width $3dB$
0.1	9.04	29°	63.5°
0.5	8.72	36°	64.3°
0.8	8.08	40°	72.0°
1.0	7.97	41°	127.2°
1.5	7.04	44°	148.7°
3.0	7.35	0°	118.9°

Table 4.2 Simulated realized H-plane gains with varied RHS capacitance where LHS is short circuited at the resonant frequency of $1.85GHz$

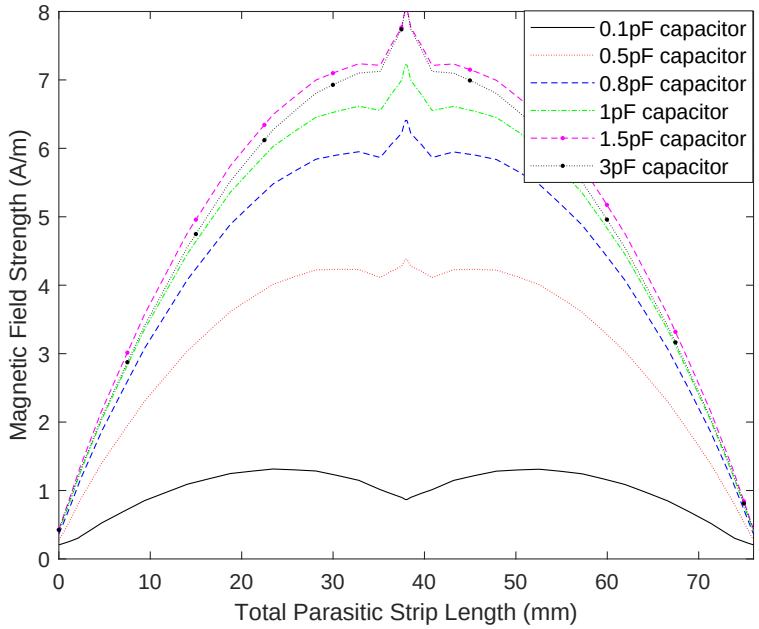

Fig. 4.18 Simulated magnetic field strength along the $\lambda/2$ parasitic strips with $0.1pF$-$3pF$ capacitor values varied on RHS parasitics

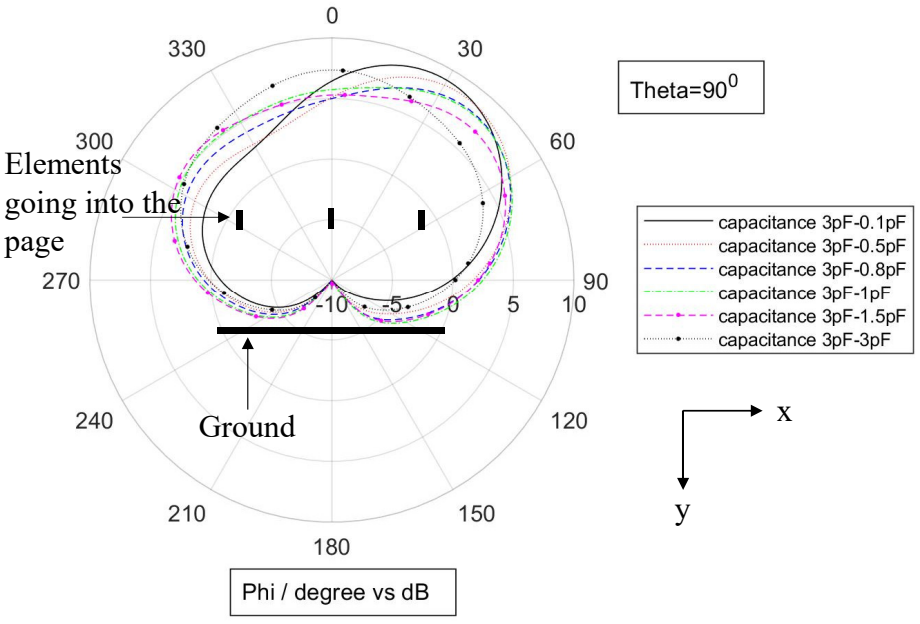

Fig. 4.19 Simulated realized far-field gain patterns with capacitors placed in between $\lambda/2$ RHS parasitics are varied between $0.1pF$-$3pF$ where beam steering along the azimuth plane is observed at the resonant frequency of $1.85GHz$

limited to two $\lambda/4$ parasitics strips with a high impedance in between the strips the current distribution (magnitude and phase) is altered and a low magnetic field strength is observed. However, increasing the capacitance and allowing more current flow within the strips it can be seen that the magnetic fields along the parasitic strips have been enhanced and the steering angle of the radiation pattern is increased proportionally. Equating the capacitances at both parasitics where identical current behaviour is attained along the parasitics, the effect on the radiation pattern is balanced therefore the beam is directed towards the boresight direction where $\theta = 0^{\circ}$. The figure of interest is illustrated in Figure 4.19, where realized gain polar plots are plotted with various capacitances included between the RHS parasitic strips located at a $\lambda/2$ distance away from the radiating dipole where the LHS parastics are short circuited with a $3pF$ capacitance attaining full length parasitic with a length of $\lambda/2$.

Regarding to the literature, it can be concluded that the structure is displaying a behaviour similar to basic Yagi-antenna which is known as an end-fire antenna where the main lobe of the radiation pattern is enhanced and directed towards the directors. Therefore increasing the amount of capacitance in the RHS reflector directs the beam towards the H-plane (x-direction) where field is at broadside in E-plane. On the other hand it can be examined that increasing the amount of steering results with an increase in the angular width, decreasing the gain at the desired direction. Due to the symmetry similar results could be achieved with short circuiting the LHS parasitics and the beam will be directed towards the (-x direction) along the azimuth (H-plane). It can be concluded that varying the amount of capacitance between the reflectors strips, a smooth beam steering within various angles with reasonable gain has been achieved.

4.6 Design Evaluation with 5 Element Model with Parasitic Strip Spacing of $\lambda/2$

The model of interest is illustrated in Figure 4.20. As it can be seen a more compact structure has been created where two additional parasitic strips of $\lambda/2$ lengths are included in the design for further increasing the steering angle of the model. The lengths of the driven element and parasitics as well as the spacings between each element has been arranged to be half of a wavelength. As represented in the figure, the model comprises a driven element fed from the middle and two parasitic strips placed at each side along the (x-axis). As stated previously, capacitors were implemented to control the flow of current between the two $\lambda/4$ parasitic strips. The elements are placed over a perfectly electrical conductor ground plane with dimensions of approximately 2λ by λ at a distance of $\lambda/4$. The parasitics positioned at the RHS (x-direction) of the dipole has been allocated with various capacitance values $0.1pF$ to $3pF$. The LHS parasitics are with a length of $\lambda/2$ where the connection is established with a $3pF$ capacitance placed between the strips as discussed previously in section 4.5. Corresponding results achieved with the structure explained above is displayed in Table 4.3.

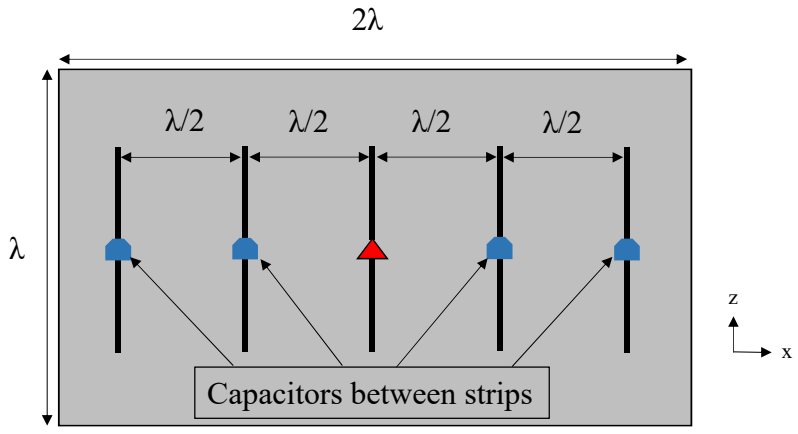

Fig. 4.20 Top view of the model over a small ground 2λ by λ with 2 set of parasitic strips on each side with capacitors included connecting the strips

Capacitance (pF)	Realized Gain (dBi)	Beam Steering Angle	Angular Width $3dB$
0.1	9.8	36°	51.6°
0.5	9.5	43°	48.1°
0.8	8.1	47°	68.9°
1.0	6.9	47°	127.5°
1.5	7.4	-29°	109.0°
3.0	7.8	24°	97.2°

Table 4.3 Simulated realized H-plane gains with 5 element model, varying RHS capacitances where LHS is short circuited at the resonant frequency of $1.85GHz$

According to the table presented above in Table 4.3, it can be observed that beam steering angle has been improved compared to the previous model where a peak steering angle of 47° is achieved when LHS parasitics are connected with $3pF$ capacitance and RHS capacitances are adjusted to $0.8-1pF$. The reflectors on the RHS have been acting as directors focusing the beam towards the x-direction. Increasing the amount of capacitance has enhanced the angle of steering along the azimuth plane due to the increase of induced

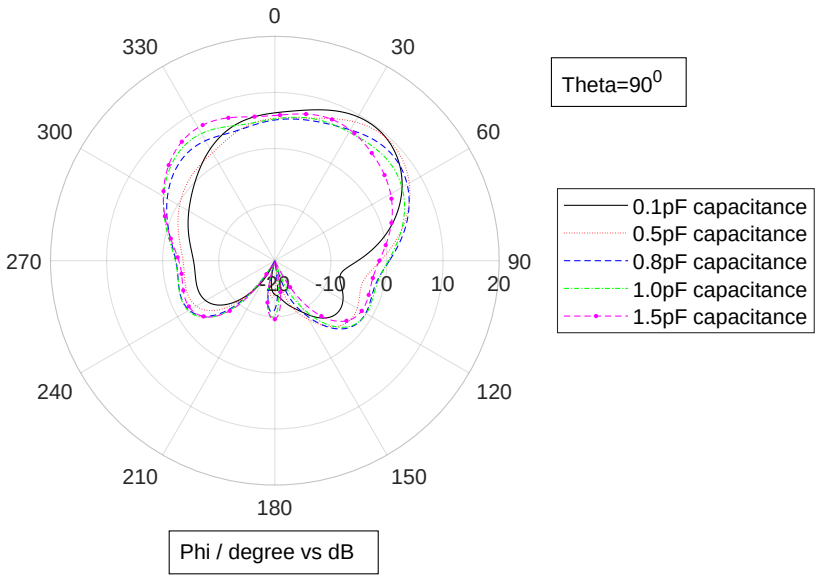

Fig. 4.21 Simulated realized far-field gain patterns with capacitors placed on RHS parasitics are varied between $0.1pF$-$1.5pF$ where beam steering along the azimuth plane is observed at the resonant frequency of $1.85GHz$

current magnitude on the strips. However an unexpected behaviour is achieved with a $1.5pF$ capacitance where the main lobe magnitude is observed at the -x-direction which can be related to the propagation of the induced currents along the parasitics causing a reduction on the magnetic field strength and hence the beam is tilted towards the -x-direction along the azimuth (H-plane). Furthermore analysing the table illustrated above it can be seen that with $3pF$ capacitance connecting the parasitic strips results in a 24° beam steering towards the x-direction. It can be clearly observed from the Figure 4.21, that the inclusion of two parasitics at each side has lead to a model which can be related to conventional Yagi-Uda topology where directors are used to direct the beam towards the enfire direction. Where in this case the two short circuited parasitics placed at either side of the radiating dipole contributes with the radiation pattern to direct the beam towards the $\pm$ x-direction respectively. However the lengths of the parasitics are adjusted to resonate at the operating frequency rather than being a reflector or a director therefore two main lobes are observed. The software programme can only illustrate a single main lobe therefore it has chosen the direction which has a slight difference in the main lobe magnitude as a primary direction of radiation. For the completeness of the results, the effect of the parasitics on the radiation

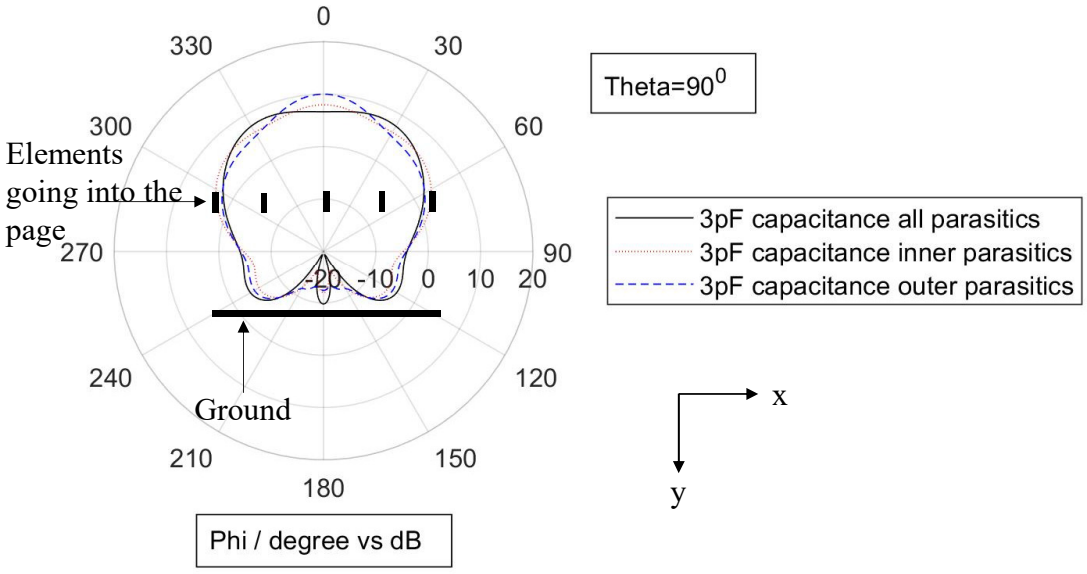

Fig. 4.22 Simulated realized far-field gain patterns with capacitors placed in between inner, outer and all parasitics with $3pF$ capacitances at the resonant frequency of $1.85GHz$

pattern has been illustrated in Figure 4.22 with connecting $3pF$ capacitance in all parasitics, secondly only at the inner parasitics and lastly only to the outer parasitics and combined in Figure 4.22. Realizing the figure represented above it has been proved that with two parasitics allocated each side with lengths of $\lambda/2$ using $3pF$ capacitors, the beam is directed off the boresight. However only including a single set of parasitics where only inner or outer strips are connected and hence the remaining ones are set to be $\lambda/4$ to minimise the effect, it is clearly observed that the strips behave as reflectors and direct the beam towards the boresight where $\theta = 0^\circ$ with a realized gain of $7.97dBi$ with parasitics $\lambda/2$ away and $10dBi$ with λ.

4.6.1 Further adjustment on the model to increase the steering angle

Since the approach of reconfiguring a pattern is to direct the main lobe of the antenna towards a desired direction with a maximum gain, as it is clearly noticed from the results illustrated in section 4.6, with such structure half of the power has been dispersed to an undesired direction. In such congested traffic of wireless communication nowadays, such behaviour would cause further interference to adjoining signals. Therefore, according to the assumptions made previously in section 4.6, in order to obtain a main lobe focused at a specific direction, reflector spacing has been modified as represented in Figure 4.23.

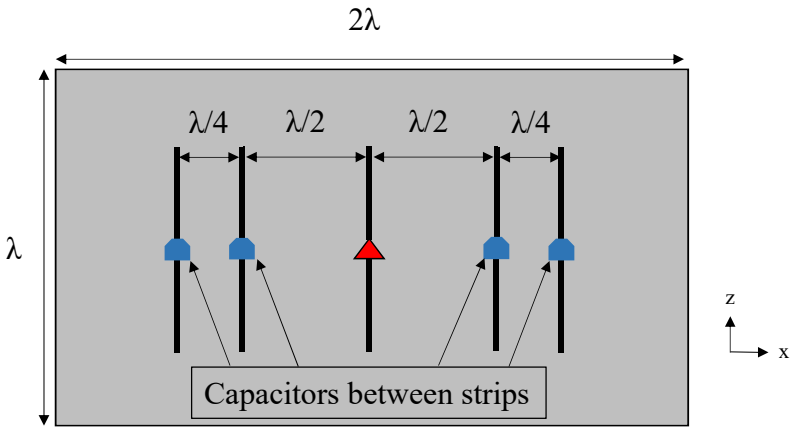

Fig. 4.23 Top view of the model over a small ground 2λ by λ with 2 set of parasitic strips on each side $\lambda/2$ and $\lambda/4$ spacing with capacitors included connecting the strips

Capacitance (pF)	Realized Gain (dBi)	Beam Steering Angle	Angular Width $3dB$
0.1	9.19	41°	77.3°
0.5	8.91	46°	45.9°
0.8	8.72	50°	44.0°
1.0	8.78	52°	43.5°
1.5	8.99	-3°	26.8°
3.0	9.02	0°	53.4°

Table 4.4 Simulated realized H-plane gains with 5 element model with $\lambda/2$ and $\lambda/4$, varying RHS capacitances where LHS is short circuited at the resonant frequency of $1.85GHz$

It can be clearly detected from Figure 4.23 represented above that first pair of reflectors which are closer to the radiating dipole have been located at $\lambda/2$ distance away from the radiating dipole. On the other hand, the distance between the outer and the first set of parasitics at each side has been reduced to $\lambda/4$ respectively. The distance of the elements to the ground plane ($\lambda/4$) as well as the ground size (2λ) by (λ) has not been changed for comparison with the previously discussed model. The radiation pattern is reconfigured with changing the capacitance between the RHS parsitics where LHS parasitics are short circuited with $3pF$ capacitance as stated previously. According to the symmetry of the model altering the LHS capacitance and short circuiting the RHS parasitics would result in beam steering towards the -x-direction. The simulation results representing the direction and the magnitude of the radiation pattern along the azimuth plane is illustrated in Table 4.4. Regarding to the set of results illustrated it can be seen that a maximum beam steering of 52° is achieved with a relatively high gain of $8.78dBi$ using $1pF$ capacitance at the RHS parasitics. With various capacitances due to the alteration of currents along the parasitics a smooth transition is achieved between 41° and 52° towards (x direction) where the angular beamwidth is reduced effectively. Therefore the approach undertaken by decreasing the spacing between the outer and inner parasitics to a length of $\lambda/4$, has been precise. The relative realized gain plots are illustrated in Figure 4.24 showing the beam steering along the azimuth (H-plane). Revealing the results in Table 4.4, there has been a significant increase in the steering angle of the radiation pattern when compared to the previous models. While increasing the capacitance

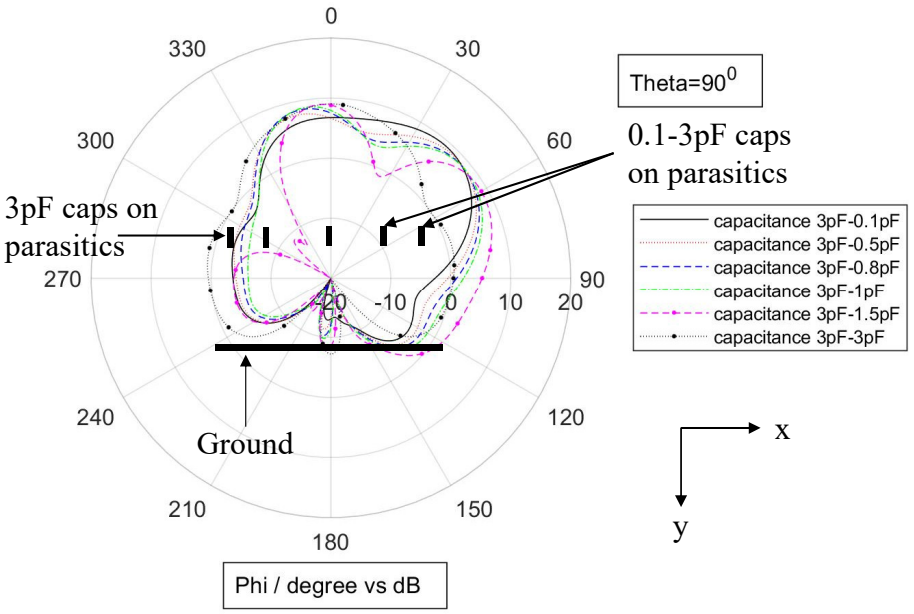

Fig. 4.24 Simulated realized far-field gain patterns of $\lambda/2$ and $\lambda/4$ parasitic spacings with capacitors placed on RHS parasitics which are varied between $0.1pF$-$3pF$ where beam steering along the azimuth plane is observed at the resonant frequency of $1.85GHz$

between the strips to allow more current flow in order to interact with the radiation pattern, due to the lengths of the parasitics which are resonant at the operating frequency, a sidelobe is generated close to the boresight direction where $\phi = 0°$. The illustrated results are achieved varying the capacitance between $0.1pF$ and $3pF$, where completely open circuiting the RHS parasitics will reduce the amount of sideloble level observed in the boresight direction. However as realised, maximum beam steering is achieved with $1.0pF$ capacitance and in order to reduce the sidelobe, there should be further complications applied to the model to enhance the control over the current flow along the parasitics where the amount of active components would increase and cause further resonances within the components leading to a less efficient and stable system.

4.7 Manufactured Design Simulation and Experimental Results

A cross-section of the beam steering manufactured design of interest is represented in Figure 4.25 consisting of a radiating element which is a half wave dipole, and 2 set of parasitic elements positioned along the dipole at a distance of $\lambda/2$ and $3\lambda/4$ away from the dipole respectively. Five elements are of copper strips with a typical thickness of $34.79\mu m$ are etched on a dielectric substrate $FR-4$ ($\varepsilon_r = 4.3, tan\delta = 0.025$) with a thickness of $1.6mm$ and placed over a height of $h_a = \lambda/4$ away from the PEC ground. Due to the inclusion of a substrate with dielectric losses and higher relative permittivity compared to the vacuum, the speed of the wave propagation will be significantly reduced hence affecting the resonance of the structure. Therefore further adjustments have been applied to establish the desired operational frequency of $1.85GHz$. The relation between the permittivity of the medium and the wavelength is evaluated with (4.7)[5, 80];

$$c = \frac{1}{\sqrt{\mu\varepsilon_r\varepsilon_0}} \tag{4.7}$$

where c, $\mu_0 = 4\pi\text{x}10^{-7}$, $\varepsilon_0 = 8.854\text{x}10^{-12}$ representing the speed of light in free space, permeability and permittivity of vacuum where relative permittivity is illustrated with ε_r.

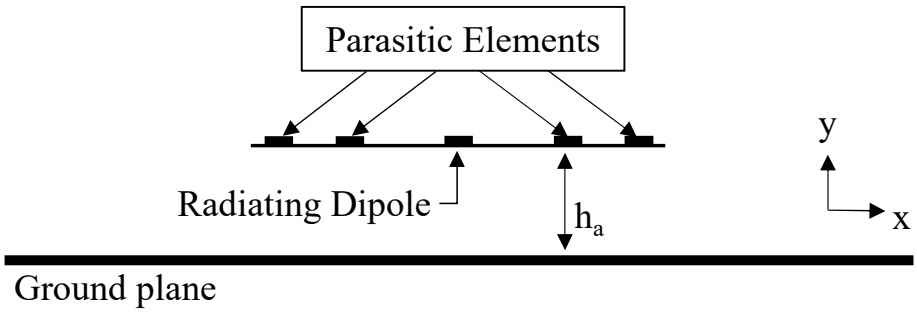

Fig. 4.25 A cross-section of the model over a small ground 2λ by λ with 2 set of parasitic strips on each side $\lambda/2$ and $\lambda/4$ spacing with capacitors included connecting the strips

The relative wavelength of an electromagnetic wave through a medium with permittivity ε_r can be represented with 4.8;

$$\lambda = \frac{c}{f\sqrt{\varepsilon_r}} \tag{4.8}$$

where λ and f represents the wavelength and the operational frequency respectively. Regarding to the equations illustrated above the lengths of the radiating and parasitic elements are optimised and reduced to $54.1mm$ length with a width of $1mm$ with the inclusion of substrate to maintain the desired resonance at the frequency of $1.85GHz$. Alternative methods of attaining the effective length of a conducting strip on a dielectric substrate has been studied where effective permittivity approximation has been made in [81]. The relative reflection coefficients (S11) is illustrated in Figure 4.26 representing the amount of reflected power from the antenna. It can be observed from the illustrated S11 results that significantly low reflection has been attained over a range of frequencies between $1.74GHz$ and $1.9GHz$

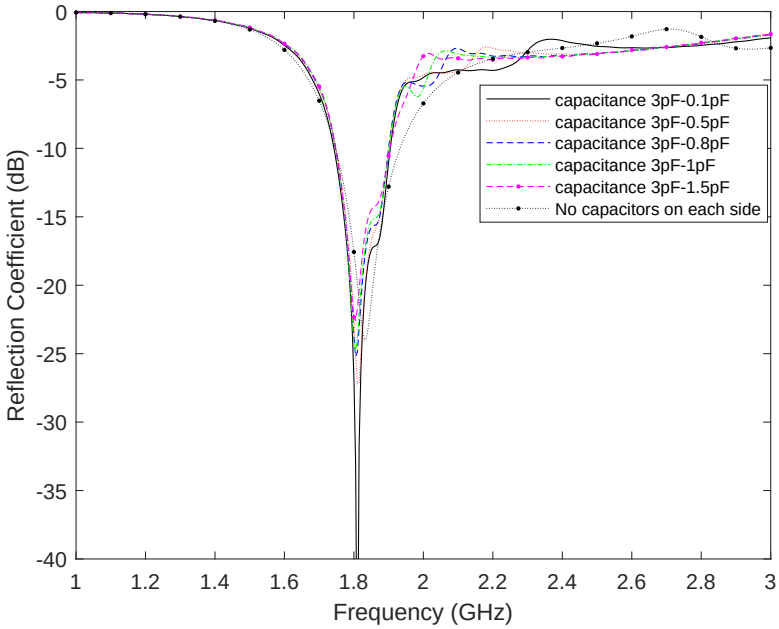

Fig. 4.26 Simulated reflection coefficients (S11) with various capacitances included at both of the RHS parasitics where LHS parasitics are short circuited with $3pF$ capacitance

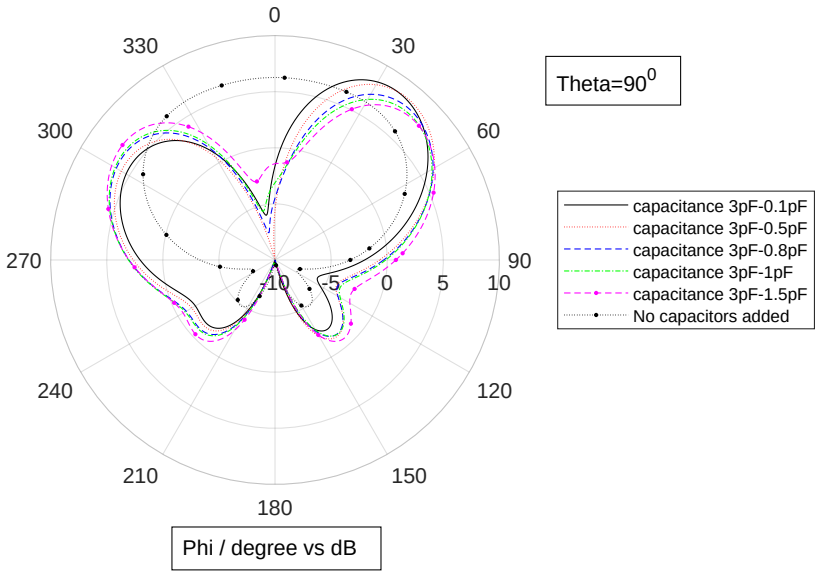

Fig. 4.27 Simulated realized far-field gain patterns of $\lambda/2$ and $\lambda/4$ parasitic spacings with $FR-4$ substrate varying the RHS capacitance parasitics where beam steering along the azimuth plane is observed at the resonant frequency of $1.85GHz$

proving that at the operating frequency of $1.85GHz$ the antenna is accepting the power sent by the source. Furthermore the achieved total efficiency of the model with different capacitor values are significantly high including losses with a minimum efficiency of 84% respectively. The corresponding far field behaviour of the model with different capacitor values inserted between the RHS reflectors are illustrated in Figure 4.27 where the LHS parasitics has been short circuited. Evaluating the results it can be stated that,increasing the capacitance where the current distribution between the two parasitic strips are enhanced the interference to the radiation pattern is increased proportionally resulting with a higher steering angle. With a $0.1pF$ capacitance included in both parasitics positioned on the RHS x-direction of the radiationg dipole, the beam has been switched from the boresight direction where $\phi = 0^\circ$ to an angle of 36° along the azimuthal plane (H-plane). Further increase on the capaciance allows more currents to propagate within the strips of a parasitic element. A smooth transition between the angle of 36° and 45° is observed from the realized gain plots represented in Figure 4.27. The realized gain of the model compared to the previously discussed results in Table 4.4 is slightly lower due to the presence of the dielectric substrate. However in overall

it can be determined that a peak realized gain of $8.62dBi$ which is relatively high compared to the single dipole which is used for the radiating element.

4.7.1 Experimental results

According to the discussions and investigations carried out within section 4.7, a prototype antenna has been manufactured as a standard PCB where the driven element and the parasitics of copper strips are etched on a $FR-4$ substrate (dielectric). The radiating dipole is fed with a $\lambda/4$ folded balun technique to balance the unbalanced coaxial by cancelling the unwanted current flow through the coaxial which is discussed in detail Section 5.6 [5]. A capture of the proposed manufactured model is shown in Figure 4.28. The antenna under test (AUT) , is placed horizontally on the rotating arm positioned 2.5m away from the transmitting horn antenna (R&S® HF906 Horn) which has a fixed position perfectly aligned at the boresight of the AUT. The complete set up for the fully anechoic chamber is illustrated in Figure 4.29. NSI 2000 R system has been configured for undertaking the measurements in the chamber

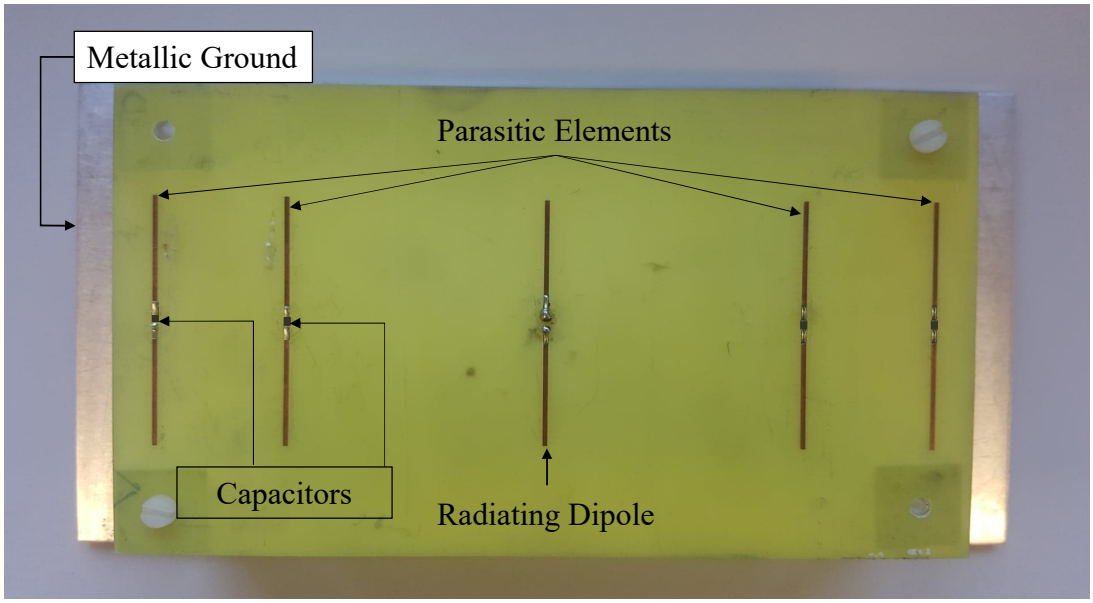

Fig. 4.28 Manufactured model over a small ground 2λ by λ with 2 sets of parasitic strips on each side $\lambda/2$ and $\lambda/4$ spacing with capacitors included connecting the strips

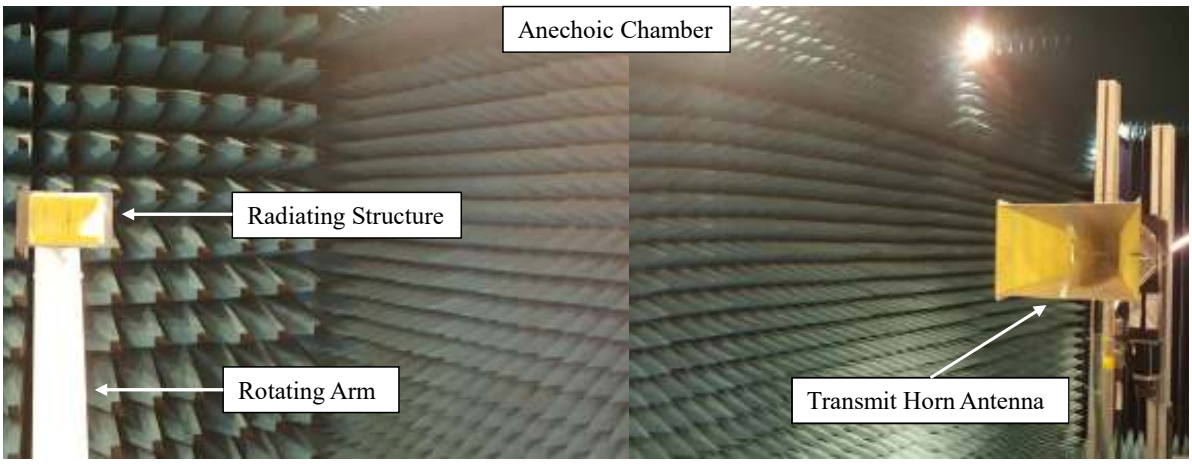

Fig. 4.29 A complete Anechoic Chamber set up with the beam steering antenna placed on the rotating arm

where E and H field 2D radiation pattern scans are carried out where complex scattering parameters are attained with a 1° step size over a $\pm 180^\circ$ range of angles. The results are analysed and exported with the aid of an Agilent Technologies E5071C ENA Series vector network analyser (VNA). As discussed previously in Section 3.4, a reference horn antenna (R&S® HF906 Horn) scattering parameters (S21) is measured and the corresponding amount of transferred powered is compared with the gain provided within the data sheet of the antenna. The gain of the AUT can be then evaluated using the Equation (3.11). As illustrated in Figure 4.28, surface mount capacitors are soldered in between the parasitic elements to establish the control of the currents over the parasitic strips. The LHS capacitors are set to be resonant with $3pF$ capacitors creating a short circuit and enabling a full length of parasitics $\lambda/2$. However RHS capacitors are varied between $0.1pF - 1.5pF$ and the measurement results are illustrated in Figure 4.30. The outcomes of the measurement results attained from the chamber reflects that the radiation pattern of the manufactured antenna at the farfield is steered along the azimuth (H-plane). A smooth transition is observed between the angles of $30^\circ - 51^\circ$ with gains varying from $7.02dBi - 7.5dBi$ where peak gain and steering angle is achieved with the adjustment where RHS capacitors are set to $1.5pF$ capacitance. The measurement results are in a good corroboration with the simulation results as illustrated in

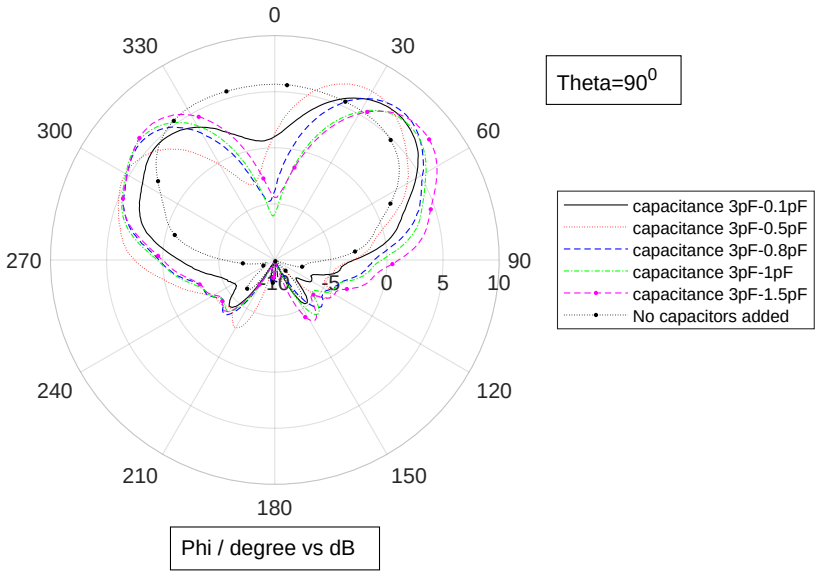

Fig. 4.30 Measured radiation gain patterns along azimuth (H-plane) of $\lambda/2$ and $\lambda/4$ parasitic spacings with $FR-4$ substrate varying the RHS capacitance between the parasitics at the operating frequency of $1.85GHz$

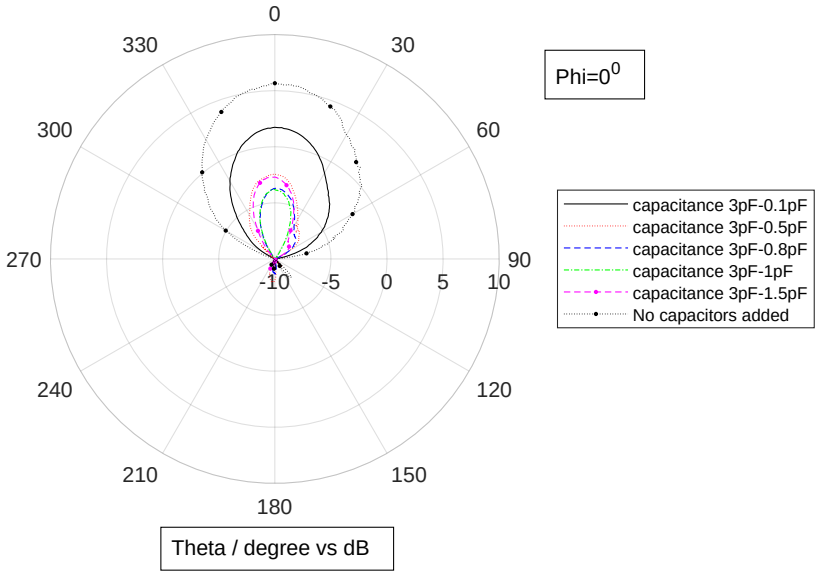

Fig. 4.31 Measured radiation gain patterns along elevation (E-plane) $\phi = 0^\circ$ of $\lambda/2$ and $\lambda/4$ parasitic spacings with $FR-4$ substrate varying the RHS capacitance between the parasitics at the operating frequency of $1.85GHz$

Figure 4.27 and Figure 4.30. Measured radiation patterns of the manufactured model along the elevation (E-plane) is represented in Figure 4.31for the completeness purposes. It can be clearly seen from the E and H plane polar plots that, towards the boresight direction the magnitude of the main lobe is in good corroboration for both planes where the peak gain along both planes where no capacitance is included within the parasitic strips, the gain at the boresight is attained to be $5.66dBi$.

4.8 Summary

A low cost beam steering antenna has been structured and proposed in this chapter. The main approach of the chapter is to reduce the complexity of the radiating structure to achieve reliable and low cost systems attaining continuous beam steering over a wide range of frequencies with a reasonably high gain compared to the previously designed models available in the literature. In this chapter two sets of dipole length parasitic strips are placed at a distance of $\lambda/2$ and $\lambda/4$ away from the radiating dipole and hence continuous beam steering is achieved within $\pm 30^{\circ}$ and $\pm 51^{\circ}$ due to the antennas' symmetrical geometry whilst varying the capacitance between $0.1pF$ and $3pF$. Both simulation and measured results attained from the chamber approve the gains of $7.02dBi$-$7.5dBi$. Further improvement on the steering angle as well as peak gain towards the intended directions will be investigated through the upcoming chapter.

Chapter 5

A High Gain Pattern Reconfigurable Microstrip Dipole Antenna with a Gain Enhancing Partially Reflecting Surface

The radiation pattern of a radiating structure can be reconfigured by varying the length and positioning of the parasitic strips as investigated in the previous chapter. Altering the currents on the parasitics using different values of capacitance, the lengths of the parasitic strips can be adjusted and the steering angle can be controlled. However the idea of having a better steering angle as well as enhancing the gain for a more reliable and efficient system for existing and future communication network systems, is considered in this chapter. The intention of this chapter is to construct a structure having the abilities to communicate with antennas positioned at boresight and endfire directions. The high gain feature is targeted due to the spectrum limitations at the allocated frequency bands, the future communication networks will be shifted to higher frequencies to handle the evolving capacity demand which is growing exponentially with everyday usage of Internet of Things (IoT). The usage of a higher frequency band in the spectrum would increase the losses according to high molecular absorption and atmospheric attenuation therefore gain enhancement has a crucial role in establishing a communication at higher frequencies. Throughout the modelling process, the

units will be expressed relative to the wavelength (λ) for the ease of adopting the structure to operate at a desired frequency. For the evaluation of the model partially reflecting surfaces will be deliberated in this chapter and the prototypes will be demonstrated at low frequencies for the proof of concept.

5.1 High Gain Beam Reconfigurable Concept

The proposed reconfigurable antenna is illustrated in Figure 5.1 as a cross section through the centre of the antenna. A radiating dipole antenna with two parasitic strips spaced on either side is placed over a ground plane at a distance of h. The antenna radiation is controlled by the use of PIN diodes placed at the centre of the parasitic elements. A partially reflecting surface is placed at a distance of h_c in order to create a cavity and enhance the gain at the intended direction. The antenna is designed to be radiating in the boresight and enfire directions by utilizing two methodologies. Considering the OFF state of a PIN diode where the PINs are placed in the middle of the strips prevent the current flow from one side of the parasitic strip to another. Therefore the total length of the strip will be approximately $\lambda/4$ which will not have a considerable effect on the radiation pattern due to non-resonant behaviour at the design frequency. In this case it is crucial to determine the spacing h_c with

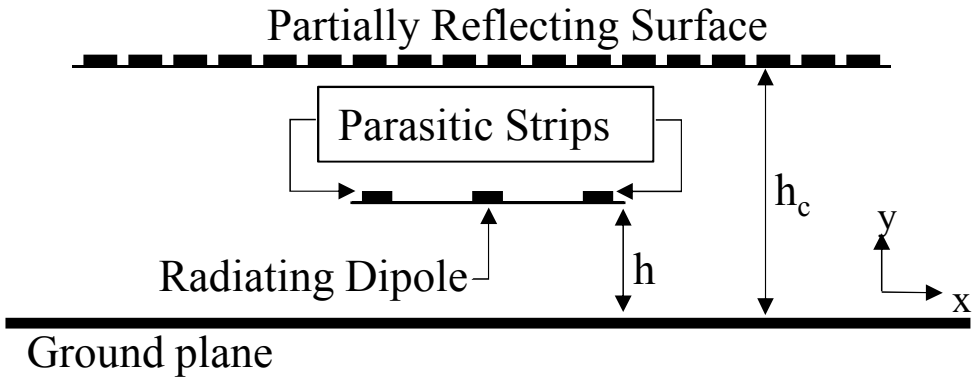

Fig. 5.1 A cross-section of the complete model for high gain beam switching antenna where top view is shown in Figure 5.2

Fabry Pérot analysis which is going to be discussed in Section 5.3 . However switching ON the PIN diodes will allow the flow of current between two strips. This will establish a connection increasing the length of the strip (approximately $\lambda/2$) to resonate and have a larger contribution to the radiation pattern if they are spaced appropriately away from the fed dipole leading to a gain enhancement towards the endfire direction.

5.2 Partially Reflecting Surface and Unit-cell Analysis

The interest and investigation on the periodic surfaces, where structures with two-dimensional distribution of the metallic elements are etched on a dielectric substrate, has been growing extensively thorough past decades where various application and problems have been addressed due to their electromagnetic band gap properties as well as the ability to be adopted as a

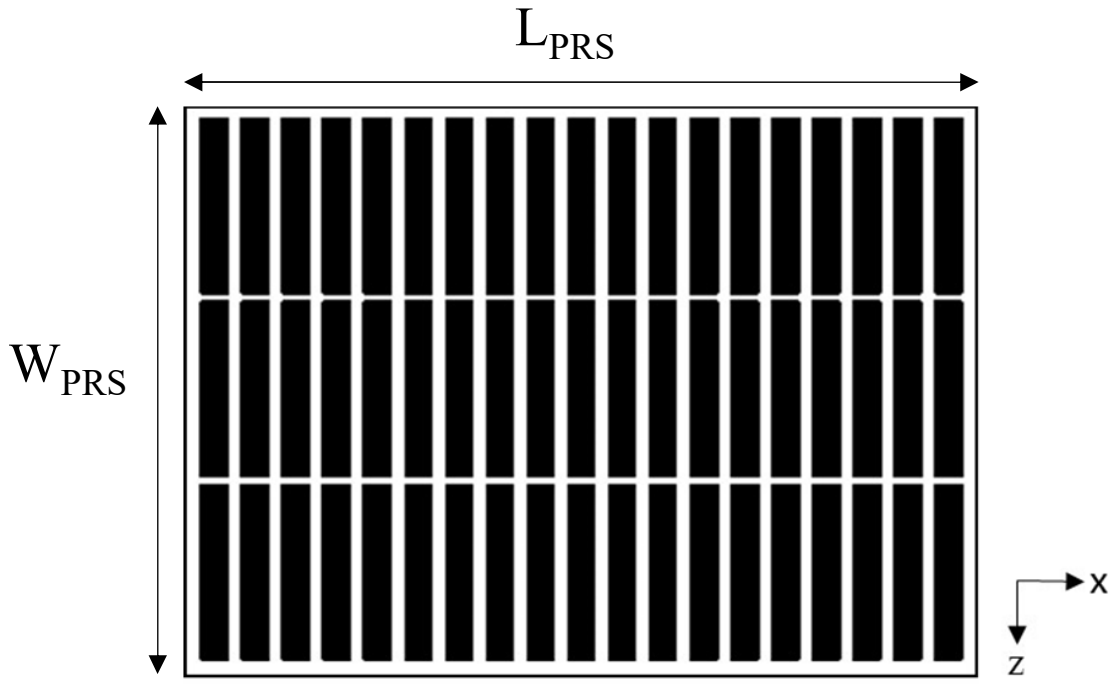

Fig. 5.2 Partially Reflecting Surface complete model top view

band pass/stop filter [82–84]. Owing the discussions included in the literature Section 2.5.1, a periodic dipole shaped metallic strips are deployed on a dielectric medium of $FR-4$ with a thickness of $0.8mm$ ($\varepsilon_r = 4.3, tan\delta = 0.025$) to create a partially reflecting surface as illustrated in Figure 5.2. The partially reflecting surface unit cell analysis is illustrated in Figure 5.3a which comprises a dipole shaped thin copper with length L and width W where the unit cell periodicity is represented with P_x and P_z. The initial steps of modelling a unit cell requires an equivalent circuit representation represented with Figure 5.3b which is then analysed in order to derive the relevant parameters such as X_L and B_C known as the reactance and susceptance for a periodic structure with an infinite amount of unit cells. The equivalent

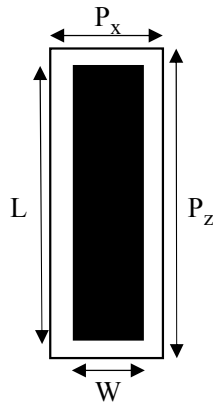

(a) Unit cell

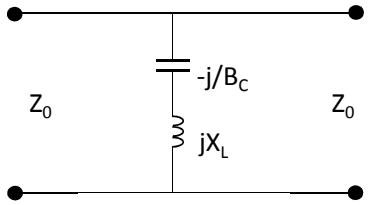

(b) Equivalent circuit of unit cell

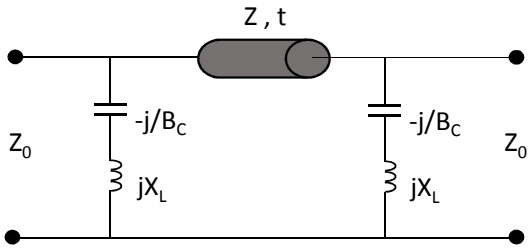

(c) Complete model analysis

Fig. 5.3 Evaluation process of a unit cell parameters with a single cell and complete model equivalent circuit representation

circuit parameters are calculated using (5.1) and (5.2) [85],

$$X_L = \frac{KP_xZ_0\left(\frac{P_z-g_{zeff}}{P_z}\right)}{\lambda}\left[ln\left(cosec\left[\frac{\pi w_{eff}}{2P_x}\right]\right)\right] \tag{5.1}$$

$$B_C = \frac{4K_{eff}KP_z\left(\frac{w_{eff}}{P_x}\right)}{Z_0\lambda}\left[ln\left(\frac{2P_z}{\pi g_{zeff}}\right)\right] \tag{5.2}$$

where $w_{eff} = 1.68W\sqrt{\frac{P_x-W}{P_x}}$, $g_{zeff} = 0.29\sqrt[4]{P_z-L}\sqrt{\frac{P_z}{P_x}}$ and $K = \frac{P_z}{P_x\sqrt{L}}$. The remaining term, K_{eff}, can be estimated using (5.3).

$$K_{eff} = 0.475f_1f_2f_3 \tag{5.3}$$

where

$$f_1 = 1 - 1.37\left(\frac{P_z-L}{P_z}\right)\left[\tanh\left(25\frac{P_z-L}{P_z}\right)\right]^2 \tag{5.4}$$

$$f_2 = 1 - \exp\left(-13t_s + \frac{13}{\varepsilon_r}\sqrt{\frac{t_s}{\varepsilon_r}}\right) \tag{5.5}$$

$$f_3 = \frac{\varepsilon_r}{(\tanh[\sqrt{\varepsilon_r}])^2} \tag{5.6}$$

t_s and ε_r represents the substrate thickness and relative permittivity respectively. The values calculated for $X_L = 3.6\Omega$ and $B_C = 0.011\Omega^{-1}$ for reactance and susceptance are implemented in $B_C = \omega C$ and $X_L = j\omega L$ to derive the capacitance and inductance as $C = 0.973pF$ and $L = 0.325nH$. The full model equivalent circuit for the Fabry Pérot resonator is then generated as illustrated in Figure 5.3c. As it can be seen the ground plane of the resonator has been removed and image theory has been employed by adding a second PRS at a distance of $t = 2h_c$ [60] where the transmission coefficients are then investigated in CST Design Studio, through which a maximum would then provide a Fabry Pérot resonance condition. Following the design approach the PRS dimensions are determined to be $L = 97.5mm$, $W = 15.15mm$, $P_z = 102mm$ and $P_x = 22.72mm$ for a resonance at $1.8GHz - 1.85GHz$ band where the frequency was chosen both for demonstration purposes and is also a typical cellular transmission frequency. Throughout the designing process of the unit cell, a full field simulation has been generated for corroboration of the transmission coefficients of the model. The resonator was modelled as a unit cell of an infinite structure by adopting a Floquet mode analysis. A frequency domain solver has been set up with highly defined tetrahedral meshing due to the small size of the structure. The boundary conditions are set to be periodic along the x and $y-axis$ where the ports Z_{max} and Z_{min} are aligned at a distance of

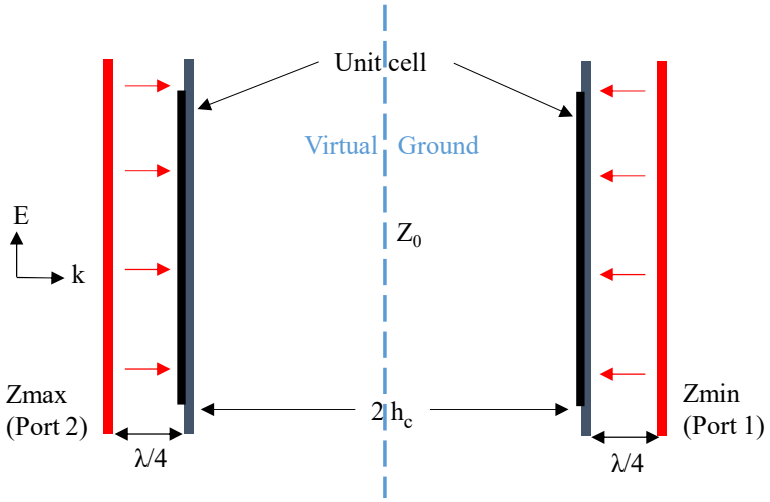

Fig. 5.4 Floquet mode full field analysis with two unit cells spaced $2h_c$

$\lambda/4$ away from the unit cells at each side as illustrated in Figure 5.4 where E and k represents the direction of the electric field and the propagation direction of the waves. According to the set up illustrated in the figure above, for evaluation purposes the floquet mode and the equivalent circuit transmission coefficients are computed with a distance of $2h_c$ where $h_c \sim \lambda$ and the results are shown in Figure 5.5. The results achieved with the equivalent circuit model represents a transmission through the free space where $Z_0 = 377\Omega$. The equivalent circuit has been created and operates under a perfect environment where no losses exist which can be determined from the peak at $1.85GHz$ which is $0dB$ proving a perfect transmission. However as it is illustrated in the Figure 5.5, with the floquet mode full field simulation the transmission frequency has been decreased significantly to $1.81GHz$ due to the effect of the propagation of the electromagnetic waves through a lossy media with dielectric losses ($FR-4$) where impurities exist. For further analysis, the separation of the unit cell hence h_c is varied and the results of transmission coefficients are presented in Figure 5.6. The unit cell dimensions were fixed where the cavity heights h_c was varied between $87.7mm - 167.7mm$. The frequency range is adapted to interpret the variations close to the desired operational

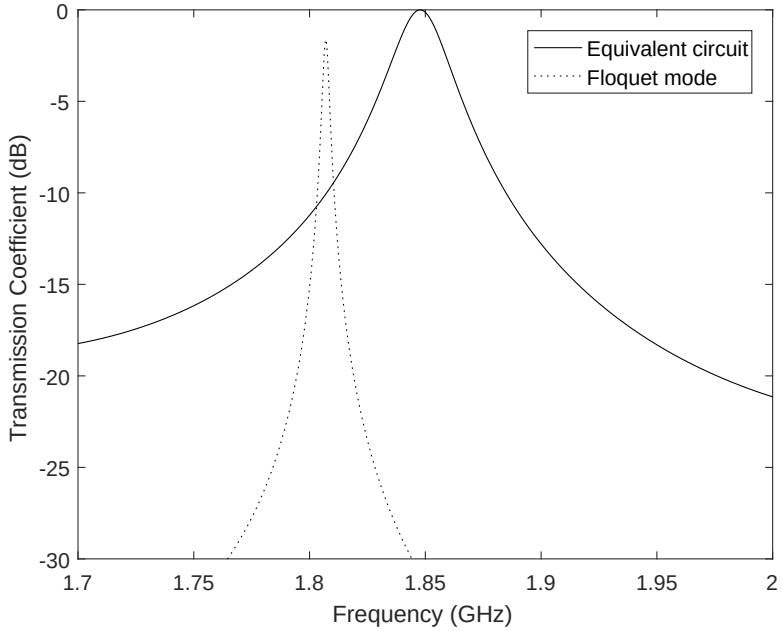

Fig. 5.5 Simulated equivalent circuit and Floquet model for PRS unit cell alone with $h_c \sim \lambda$

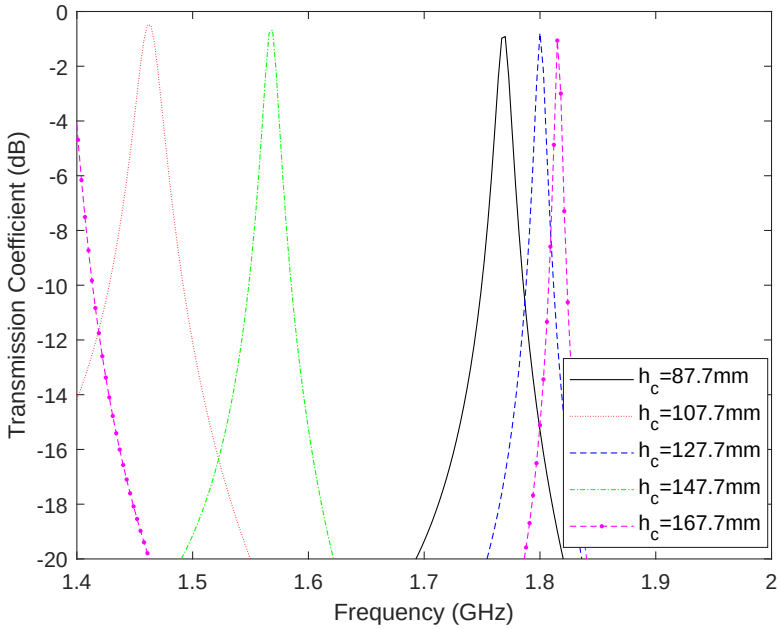

Fig. 5.6 Transmission coefficients simulated results for various h_c spacings of PRS

frequency range. As illustrated, the variation of cavity height h_c, has a considerable effect on the transmission frequency of the unit cell where increasing the distance between the unit cells, the harmonics of the transmission coefficients are observed to be shifted to lower frequencies. It can be clearly observed that with a distance of $h_c = 87.7mm, 127.7mm$ and $h_c = 167.7mm$ would be the decisive cavity height to achieve the gain enhancement towards the boresight direction.

5.3 Fabry Pérot Implementation

Fabry Pérot resonance condition [47], which is discussed in the literature Section 2.5.1 and Chapter 3, can be adopted to calculate the PRS spacing for enhancing the gain towards the intended direction. In this section further analysis for the desired specifications to enhance the boresight gain has been carried out. The topology of Fabry Pérot condition is to generate multiple reflections within a cavity formed of a ground plane and a PRS shown in Figure 5.7.

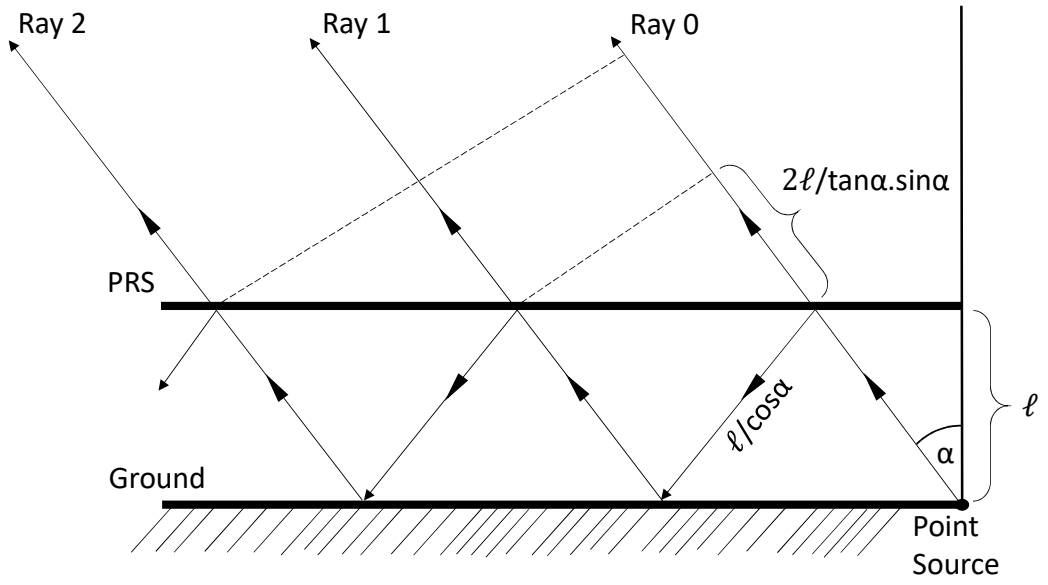

Fig. 5.7 Partially reflective sheet array model of Trentiny [47]

A point source is deployed at the edge of the ground plane with a distance ℓ away from the partially reflected surface labelled as PRS. Due to the consecutive reflections within the cavity, phase differences between the direct and reflected waves will be observed and this relation can be represented with (5.7);

$$\Theta_1 = \frac{2\pi}{\lambda} 2\ell \tan\alpha \sin\alpha - \frac{2\pi}{\lambda}\frac{2\ell}{\cos\alpha} - \pi + \psi \tag{5.7}$$

where λ is the free space wavelength, ℓ is the spacing between the PRS and ground plane, α is known as the angle of incidence. The reflected waves from the ground plane is considered with additional 180° phase shift included as π and ψ can be denoted as reflection phase of the PRS. Previous studies [47, 49, 51, 65] revealed that, according to the phase differences generated within the cavity with distinctive path lengths, the directivity at the boresight direction can be determined, when $\alpha = 0°$ as shown in (3.9). In order to evaluate the height of the

cavity for maximum directivity, the phase difference between direct and the reflected wave is represented with $\phi = \psi - \phi_{GND} - \frac{4\pi}{\lambda}\ell\cos\alpha$ where ϕ_{GND} is the reflection phase of the ground plane which then can be arranged to attain the resonant height for gain enhancement is illustrated using (5.8) [60];

$$h_c = \frac{\lambda}{4\pi}(\psi + \phi_{GND} - 2N\pi) \qquad N = 0, 1, 2... \tag{5.8}$$

where N, is an integer number. Since the source is placed within the cavity at a distance of h from the ground plane, this height h as well as the PRS height h_c should be aligned to have reflected and radiated waves to constructively accumulate. The reflection phase of the ground plane can be achieved with the given Equation (5.9) [60];

$$\phi_{GND} = \pi - 2\tan^{-1}\left(\frac{Z_d \tan\left(\frac{2\pi h}{\lambda}\right)}{Z_0}\right) \tag{5.9}$$

where Z_d and Z_0 are the characteristic impedances of the spacer material and freespace respectively. Regarding to the calculations represented in (5.8), Fabry Pérot resonance condition is achieved with a cavity height of $h_c = \lambda/2$ where the beam is focused in the boresight direction. However the cavity height , contributes to the reconfigurability behaviour of the model. For a more inclusive analysis the behaviour of the complete model with variable cavity height h_c will be presented with ON and OFF states of PIN diodes in Section 5.5.

5.4 Radiating Structure Antenna Design and Evaluation

The design of interest is represented in Figure 5.8 consisting of a dipole with a length of approximately $\lambda/2$ and two parasitic strips equally spaced on each side with a resonant frequency of $1.8GHz$. The copper strips with a typical thickness of $34.79\mu m$ are etched on a dielectric substrate $FR-4$ ($\varepsilon_r = 4.3, tan\delta = 0.025$) with a thickness of $1.6mm$. As it is indicated in the literature, an increased length of a parasitic strip relative to the radiating element have an inductive behaviour which is used as a reflector however a shorter strip is capacitive due to the electrical length directing the beam towards the intended direction [26]. The modelled radiating structure is represented in Figure 5.8.

The length of dipole and two parasitic strips were set to $L_d = 54.27mm$ due to the effect of the dielectric substrate with a higher permittivity. The propagation of waves are considerably slower than free space causing a decrease at the resonant frequency. At the proposed design whilst the PIN diodes are at ON state the parasitic elements are chosen to be resonant in order to have a maximum impact on the radiation pattern. The parasitic strips are placed at a distance of L_p on either sides of the radiating dipole and are formed with two thin metallic strips which are connected with PIN diodes as represented in Figure 5.8. There are several

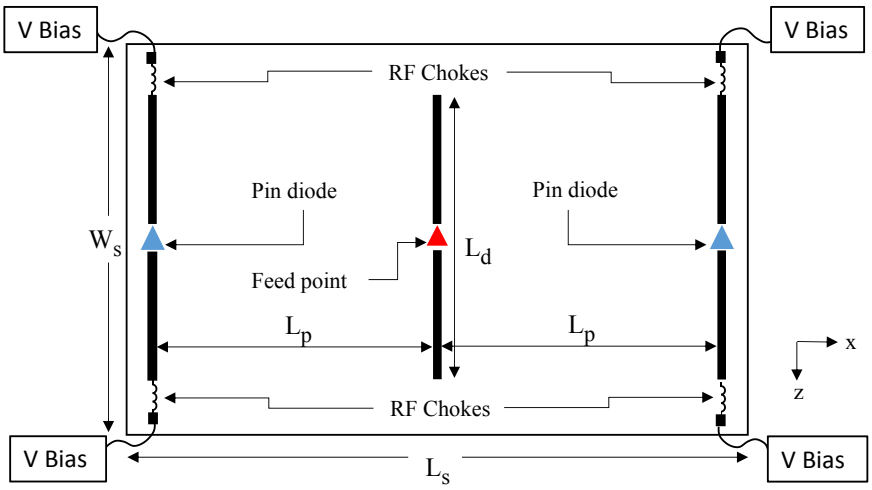

Fig. 5.8 Radiating antenna structure with parasitic strips component and biasing allocation

paths to generate lumped elements (Capacitors, inductors, resistors) which can be added in series or parallel to generate more complicated elements such as diodes. This can be achieved by constructing a lumped element within the two preselected metallic edges in the microwave studio. However if the designed structure is occupying large amount mesh-cells, optimization of the element values will occupy a larger amount of time due to the repetitive simulations for each parameter sweep. This can be resolved using the CST Design Studio where the model which is simulated in Microwave Studio is imported as a block reflecting the behaviour of the model. Instead of generating the lumped elements in MWS, discrete ports have been created for each component between the two edges of the metallic strips where the components will be connected. The simulation time for a model occupying a determined number of mesh-cells have a constant simulation time for each run. Therefore increasing the number of ports would increase the simulation time uniformly however no repetition of the complete model simulation in MWS is necessary for further optimization which could be carried out in the Design Studio. The block model in design studio is then modified with the addition of components to the corresponding ports. The effect of the components can be evaluated in much shorter times and the results are merged with Microwave Studio simulations with a post process of combining results. For evaluation purposes a lumped and spice model of the Infineon Technologies BAR64-02V were used due to its good performance

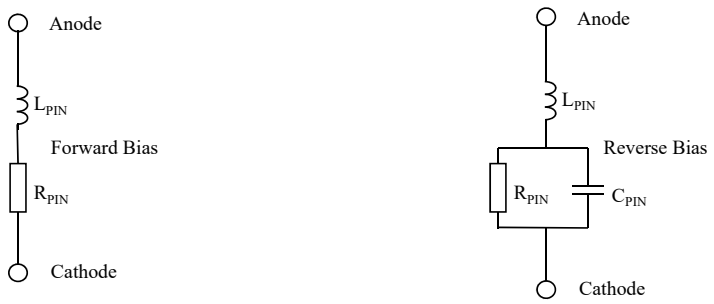

(a) Forward Bias "ON" (b) Reverse Bias "OFF"

Fig. 5.9 Forward and reverse bias PIN diode equivalent circuit representations

in the presence of high frequency radio waves up to $6GHz$ and offers a very low capacitance $0.17pF$ at zero volts where almost complete isolation can be achieved between forward and reverse bias states. The relevant circuitry Figure 5.9 and component values at each state were obtained from the relative data sheet [86] of the product which assisted in configuring the biasing conditions for the spice model method. A forward bias voltage of $1.5V$ applied with a $50mA$ current in order to turn ON the specific PIN diode. When the PIN diodes are forward biased the equivalent circuit is a series resistor (R_{PIN}) and inductor (L_{PIN}) with the values of $R_{PIN} = 1.35\Omega$ and $L_{PIN} = 0.6nH$ respectively. Forward biasing the PIN diodes "ON" state, will short circuit the two ends of the parasitic strip which would generate a full path $\lambda/2$ length for the currents to be distributed and resonate at the resonant frequency, interfering with the radiation pattern of the dipole and hence the beam will be directed towards the endfire direction. However in reverse bias "OFF" state, as stated previously, the current flow through the strips will be restricted and the strips which are shorter in length would not resonate at the desired operating frequency and the effect on the radiation pattern will be diminished. In the reverse bias state the equivalent circuit can be represented as a series RLC where the component values for the resistance, inductance and capacitance are $R_{PIN} = 1.35\Omega$, $L_{PIN} = 0.6nH$ and $C_{PIN} = 0.17pF$. Voltage bias lines are also included which are used to apply the required voltage for switching between "ON" and "OFF" state of PIN diodes. The biasing lines are connected to a power supply where the flow of RF through the cables are blocked with the use of high impedance RF chokes (inductors) of values $L_{ind} = 22nH$.

5.5 Simulations for Full Structure Analysis and Optimization of Parameters

Design methodologies and evaluation of the individual parts of the structure has been considered in the previous sections of this chapter which will be combined and constructed in this section. A set of simulation results will be investigated and analysed for the optimization of the complete structure for a desired beam switching at the boresight where $\theta = 0^\circ$ and

endfire directions. For evaluation purposes 19x3 unit cells are used to generate the partially reflecting surface with a size relatively large with dimensions $W_{PRS} = 1.9\lambda$ and $L_{PRS} = 2.6\lambda$ as illustrated in Figure 5.2. The cavity is formed with a reflecting sheet (ground plane) with dimensions of 3.3λ x 3.3λ is placed a $\lambda/4$ away from the radiating antenna to generate constructive in phase reflected waves by creating a $\lambda/2$ propagation distance as illustrated in Section 5.1.

5.5.1 Cavity height adoption

It is understood from Fabry-Perot analysis that there are a number of choices for h_c where the resonant conditions apply, however, there is a trade-off between the borsight and endfire gains where further analysis has been carried out for the "ON" and "OFF" diode states.The effect of the cavity height h_c on the radiation pattern is represented in Figure 5.10. The cavity height h_c is varied between the lengths of appropriately $\lambda/2$ and λ. It has been proved with the calculations that (5.8), Fabry Pérot resonance condition can be achieved with a cavity height

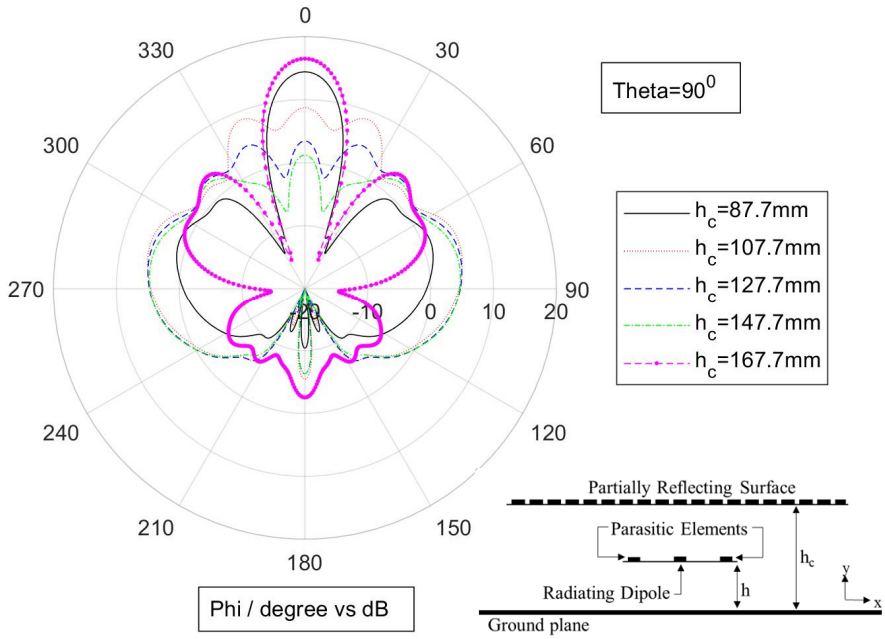

Fig. 5.10 Simulated realized H-plane gain patterns with "OFF" State PIN diodes at the resonant frequency of 1.8GHz

of 87.7mm away from the ground plane. The realised gain (H-plane) towards the boresight where $\phi = 0°$ is verified to be 14.42dBi with "OFF" as well as $-0.63dBi$ with "ON" state PIN diodes. Whilst the cavity height has been increased, it can be clearly seen that the PRS is at a position where resonance condition has not been attained. As a result the radiation patterns with a cavity height of $h_c = 107.7mm$ and $h_c = 127.7mm$ is arbitrary where multiple low gain beams are observed. However when the PRS has been positioned λ away from the ground plane, an anti-resonant mode of Fabry Pérot has been accomplished which enhances the gain towards the boresight when the PIN diodes are at the OFF state. Hence a substantial null is created along the enfire direction where $\phi = 90°$. According to the simulations results, the boresight realized gain of 16.5dBi is accomplished with a cavity height of $h_c = 167.7mm$ and $-14.19dBi$ gain towards the endfire direction. Such radiation pattern with a big null at the endfire direction and higher gain towards the boresight will increase the chances of beam switching compared to the cavity height of $h_c = 87.7mm$. Relative S-Parameters of the model with the PIN diodes at OFF states are represented in Figure 5.11. It can be clearly stated that

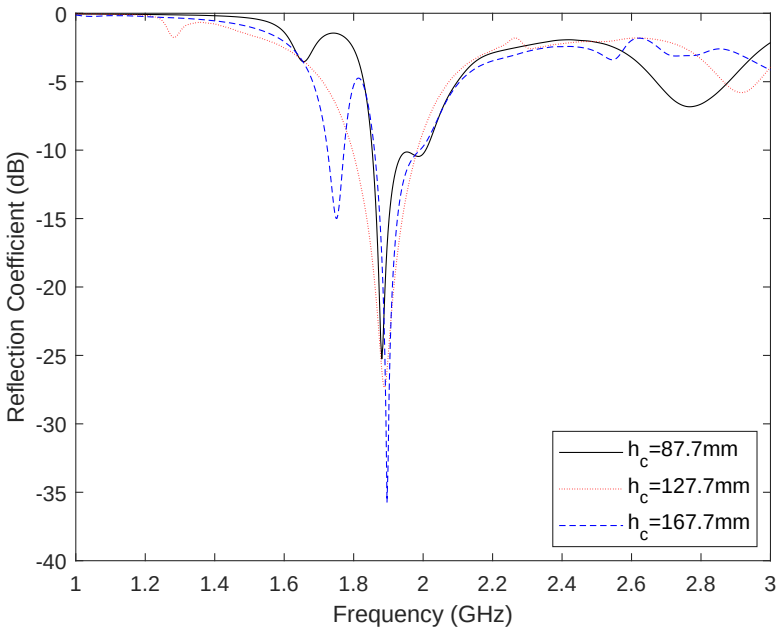

Fig. 5.11 Simulated reflection coefficients (S11) with diverse cavity height and OFF state PIN diodes

the inclusion of PRS where a cavity is formed, the direct propagation of the waves which are reflected back to the radiator have a different phase which interferes with the distribution of currents along the radiating strips and hence the return loss is increased. At the desired frequency of $1.8GHz$, a reflection coefficient magnitude of $S11 = -5.26dB$ is achieved with the cavity height $h_c = 167.7mm$ and $h_c = 127.7mm$, whereas the reflection coefficient of the model with a cavity length of $h_c = 87.7mm$ is attained to be $S11 = -2.2dB$. To sum up, the partially reflecting surface positioned closer to the radiating structure $h_c = \lambda/2$, the interference to the radiating dipole increases affecting the efficiency of the antenna which will be investigated through the Section 5.5.3. However the matching problem could be addressed with well known uncomplicated two element matching circuits using capacitor and inductors where the imaginary part (Reactance) of the input impedance is matched to zero at the desired frequency.

The simulated radiation pattern with ON state PIN diodes are presented in Figure 5.12. As discussed previously the cavity height has been varied to visualize the effect on the radiation patterns and authorize the most convenient set up for a high gain and beam switching model.

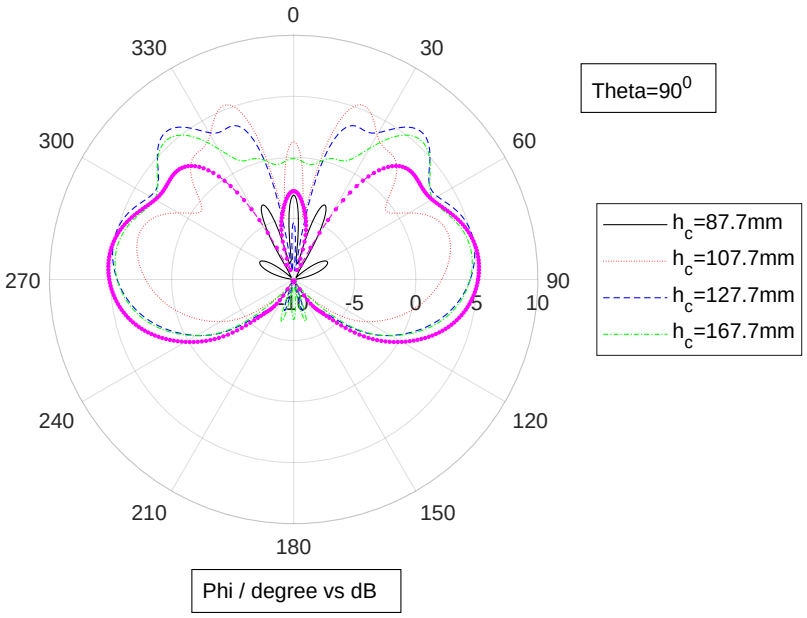

Fig. 5.12 Simulated realized H-plane gain patterns with "ON" State PIN diodes at the resonant frequency of 1.8GHz

The effect of PRS distance from the ground plane is more distinct compared to the OFF state due to the interference of two parasitic strips to the distribution of the radiated and reflected waves within the cavity. Initially the cavity height has been set to $\lambda/2$. The results illustrate that having the PRS at such distance to the ground plane cause a poor radiation performance towards the boresight where $\phi = 0^\circ$ the realised gain is $-2.76dBi$ and according to the perfect symmetry of the design a gain of $-6.88dBi$ is achieved at the angles of $\phi = 63^\circ$ and $\phi = 297^\circ$. This is mainly due to the impedance match of the antenna to the 50Ω source. In this case the simulated reflection coefficient magnitude was $-2.2dB$ which is represented in Figure 5.13. Increasing the distance of the PRS from the ground plane limits the amount of interference to the feeding point and the currents induced on the parasitic strips which would internally interfere with matching due to the capacitive coupling of the parasitics and the radiating dipole. Increasing the height of the PRS away from the ground plane reduces the effect on the matching where the dipole and the parasitics would behave in an appropriate manner where the beam could be controlled effectively. It can be clearly observed that with

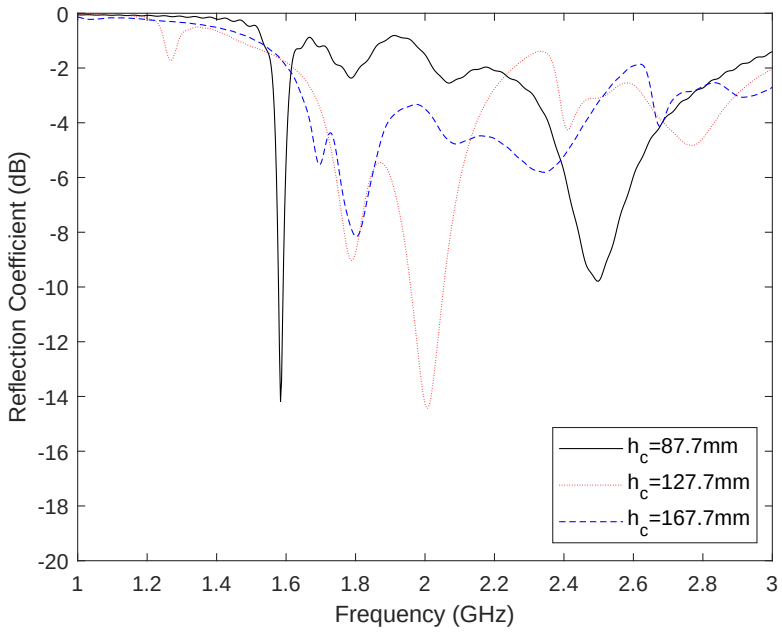

Fig. 5.13 Simulated reflection coefficients (S11) with diverse cavity heights and ON state PIN diodes

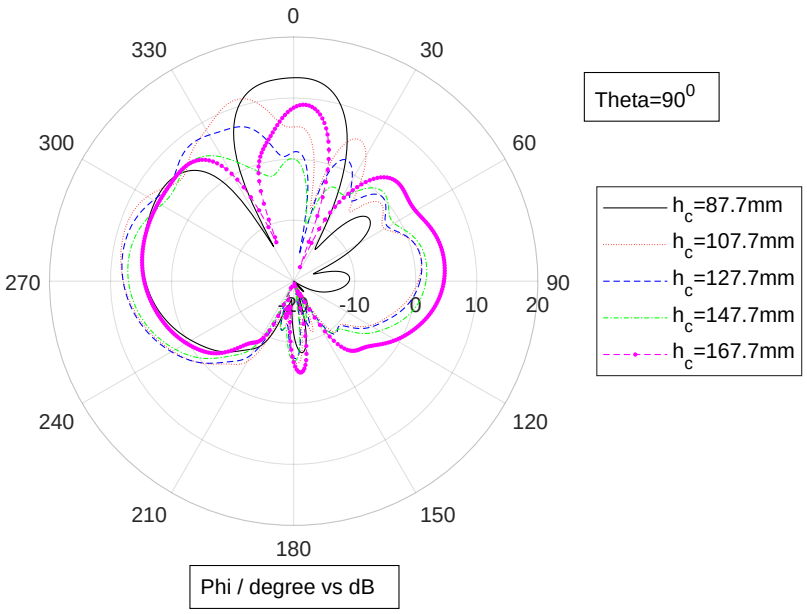

Fig. 5.14 Simulated realized H-plane gain patterns with one side "ON" and other side "OFF" State PIN diodes at the resonant frequency of 1.8GHz

a cavity height of $h_c = 167.7mm$, which is approximately a wavelength long, the endfire realized gain along the x-axis, $\phi = 90^\circ$ and $\phi = 270^\circ$ is $5.2dBi$. For the completeness of the results "OFF-ON" PIN diode states are evaluated and presented in Figure 5.14. It can be observed that a more balanced radiation pattern performance between boresight and endfire can be achieved with gains of $8dBi$ and $5dBi$ respectively. As it might be expected the radiation patterns are asymmetric due to the bias conditions on each side of the parasitic strips, where the "ON" side is resonating and "OFF" side does not contribute due to the short length of strips at the operating frequency.

5.5.2 Allocation of parasitic strips

The parasitic strip spacing located at each side of the radiating dipole as illustrated in Figure 5.8, has a crucial impact on the switching behaviour of the radiation pattern at the endfire direction. As mentioned previously in Section 5.4, the idea of allocating the parasitic strips at a certain distance of L_p to interfere the radiation pattern of a dipole antenna can

be related to the Yagi-Uda antenna topology. The parasitic strips are used as a resonator in order to have maximum impact on the boresight and endifire direction radiation patterns with "ON" and "OFF" states. However the Fabry Pérot topology can be implemented in this case where ideally with a correct adjustment of parasitic spacings a resonance condition could be achieved and gain would be enhanced towards the endfire direction (x-axis) as discussed previously in the literature Section 2.5.1. Figure 5.15 illustrates the realized gain of the complete structure with different parasitic spacings with a cavity height of $h_c = \lambda$. "ON" and "OFF" state PIN diodes are considered where the strip spacings are adjusted. As shown in the figure, the reverse bias "OFF" state gain is independent of the parasitic spacing L_p where identical set of results were achieved due to the shorter lengths of the parasitics ($\lambda/4$) which does not resonate at the desired frequency. However forward biasing the PIN diodes "ON" state, a good compromise between the maximising endfire direction whilst reducing the forward radiation can be achieved with an element spacing of $L_p = 52.5mm$ which equates to approximately $\lambda/3$.

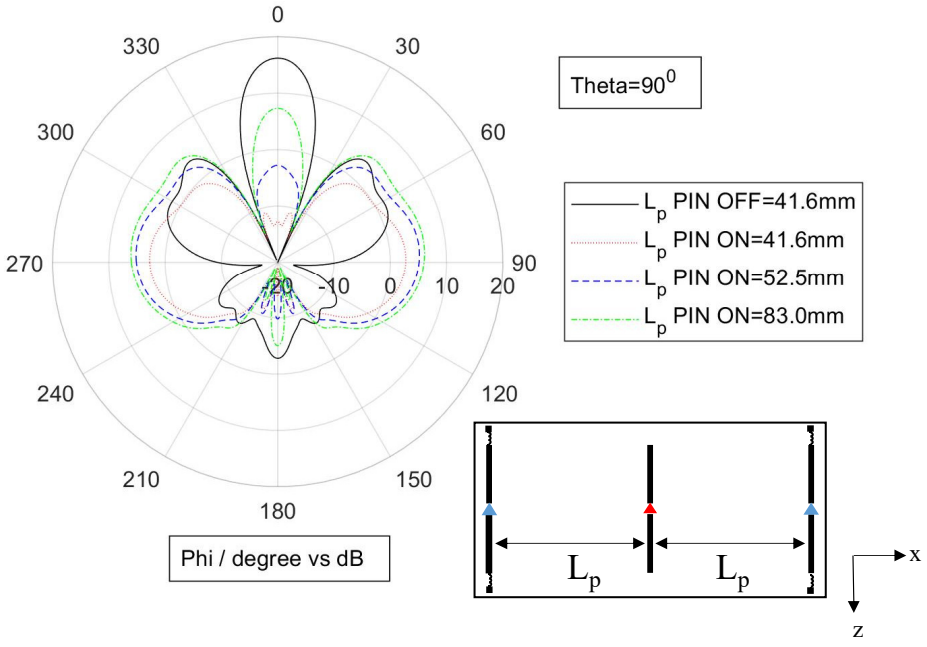

Fig. 5.15 Simulated realized H-plane gain patterns with "ON" and "OFF" State PIN diodes with different strip spacing L_p at the resonant frequency of 1.8GHz

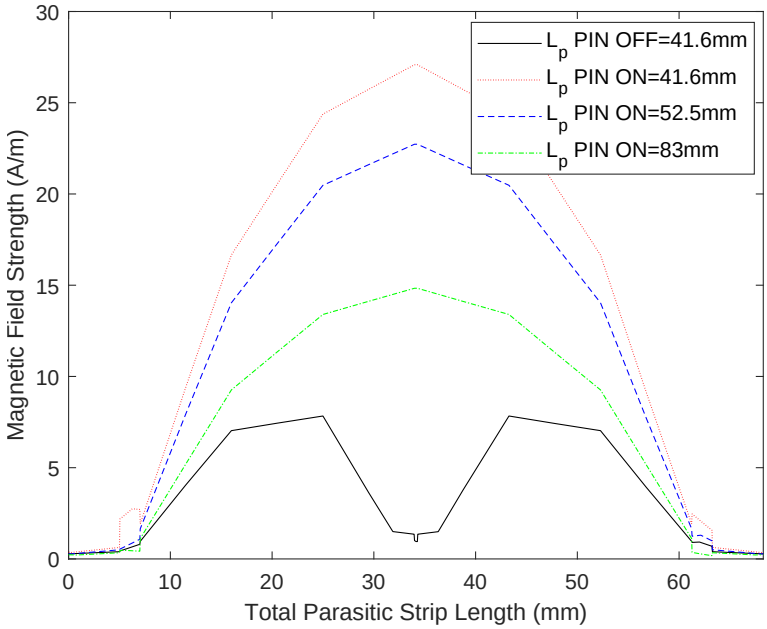

Fig. 5.16 Simulated magnetic field strength on the parasitic strips with "ON" and "OFF" PIN diode states with variable parasitic spacings

Simulation results of the surface currents along the parasitic strips with various spacings with "ON" and "OFF" state PIN diode modes are evaluated for completeness and are represented in Figure 5.16. The strip lengths are represented with the x-axis from $0-68.275mm$ including the patches for bias soldering points at the tip of each parasitic strip. It can be clearly observed that the patches are isolated completely where the magnetic field strength is minimum at each ends of the strips for both "ON" and "OFF" states. For the "OFF" state the length of the strips are shorter than half of a wavelength at the desired frequency where the magnetic field strength is considerably lower than the "ON" state PIN mode. The fluctuations on the plots are the connection points of the components that causes resonances due to impurities and tolerances at such frequencies. It is observed in Figure 5.16 that the currents induced on the parasitics increase when the distance L_d is arranged to be $\lambda/4$ length ($41.6mm$). According to these specifications it can be observed that a good cancellation of the boresight radiation is achieved with "ON" state diodes and parasitic spacing of $L_p = 46.1mm$. However the endfire radiation with such adjustment is lower than the case where $L_p = 52.5mm$. Therefore

the trade-off between the boresight and endfire radiation has been decisive on allocating $L_P = 52.5mm$ as the spacing of the parasitic strips.

5.5.3 Simulations for verification of constructed model effectiveness

The efficiency of an antenna is known as the power delivered ratio to the power accepted by the antenna as interpreted previously in Section 3.1.3. The simulated total and radiation efficiency are plotted against the frequency represented in Figure 5.17. Considering the "OFF" state PIN diodes, a radiation efficiency above 80% over the displayed frequency range is achieved where the losses are predominately due to the $FR-4$ substrate. However the total efficiency reduces down to 50% due to the mismatch. This mismatch is due to the presence of the PRS but as stated previously could be alleviated with the use of an external matching circuit. When the switches are "ON", a radiation efficiency of 68% achieved at the resonant frequency of $1.8GHz$. This can be directly related to the PIN diode resistance where a total

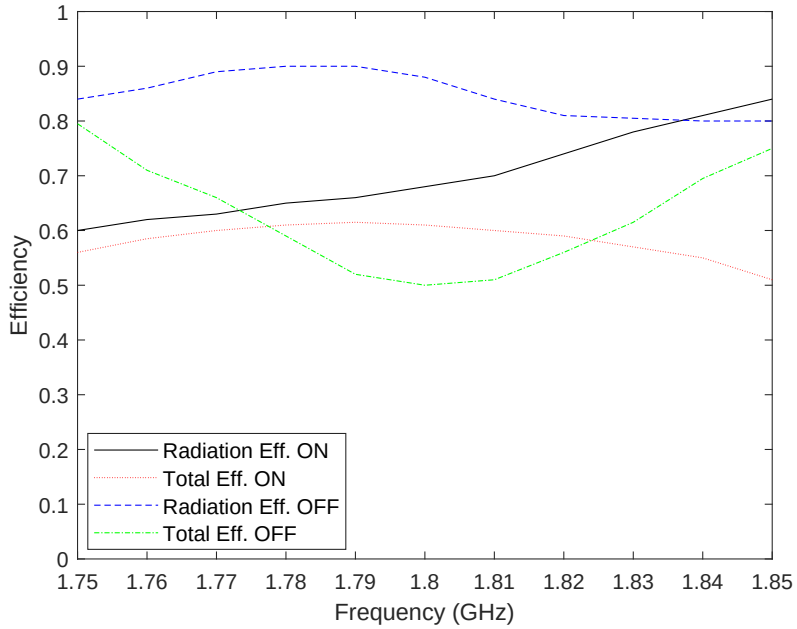

Fig. 5.17 Simulated total and radiation efficiency over frequency with "ON" and "OFF" state diodes

efficiency of 61% is attained as the antenna mismatch is reduced. Gain versus frequency is illustrated in Figure 5.18. The gain is determined over a range of frequencies where it can be observed that with "ON" state PIN diodes, the gain variation over a 100MHz frequency band with a centre frequency of $1.8GHz$ is approximately $7dB$. This can be accepted as reasonably stable and wideband compared to the typical communication bandwidths. Considering the "OFF" state, there is an increased gain variation compared to the "ON" mode. However over a 20MHz bandwidth the variation is only $0.9dB$ which would be sufficient for many communication applications.

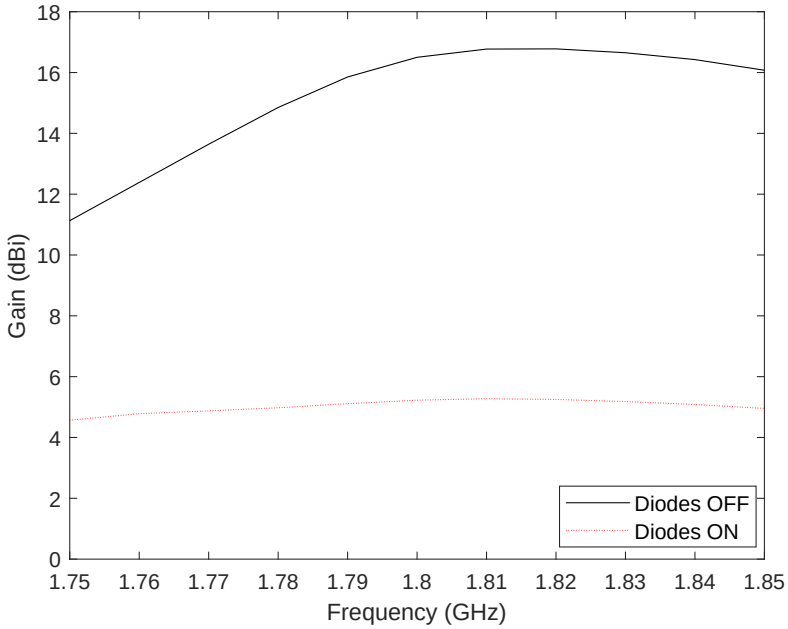

Fig. 5.18 Simulated gain over frequency with "ON" and "OFF" state diodes with $h_c \sim \lambda$

5.6 Experimental Results

A prototype antenna was manufactured using standard PCB etching techniques for both the partially reflecting surface and dipole/parasitic elements. To conduct the measurements, a feeding mechanism has been constructed to feed the radiating structure. The radiating element in the model is the dipole originated in the middle of a two parasitic strips which

is fed with a semi-rigid coaxial cable as seen in Figure 5.19a. A $\lambda/4$ folded balun was implemented on the feeding mechanism in order to balance the unbalanced dipole caused by the unwanted leakage of I_3 at the outer sleeve of the coaxial. As it is represented in the Figure 5.19b and 5.19c, a $\lambda/4$ long wire is connected to the outer sleeve of the semi-rigid coaxial cable in order to generate a current I_4 having a 180° phase shift with equal magnitude. At the point of connection which is a $\lambda/4$ distance away, the flow of currents on the outer surface sleeve which can be recognized as I_3 and I_4 are inhibited [5].

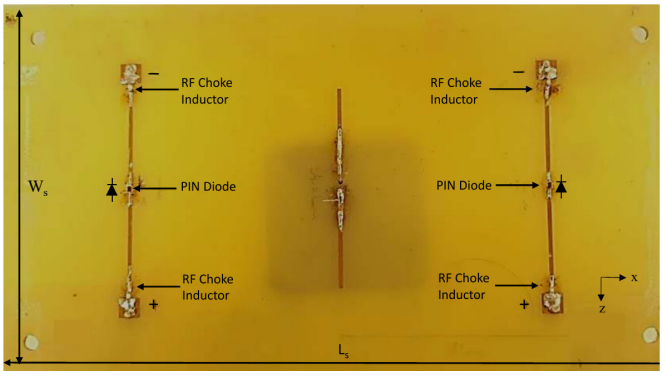

(a) A detailed capture of radiating dipole and parasitics

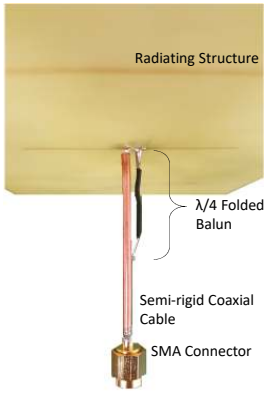

(b) Feeding mechanism of the proposed model with $\lambda/4$ folded balun

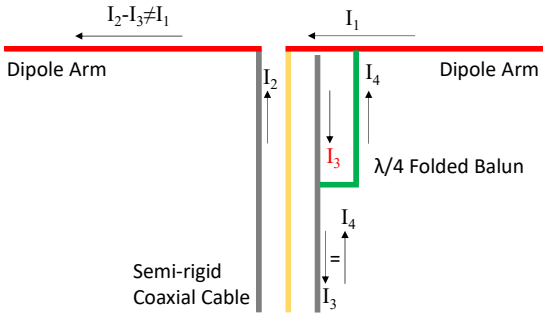

(c) Folded balun matching technique schematic with current paths [5]

Fig. 5.19 Radiating structure and the feeding mechanism of the proposed model with detailed schematic presentation of the folded balun matching technique

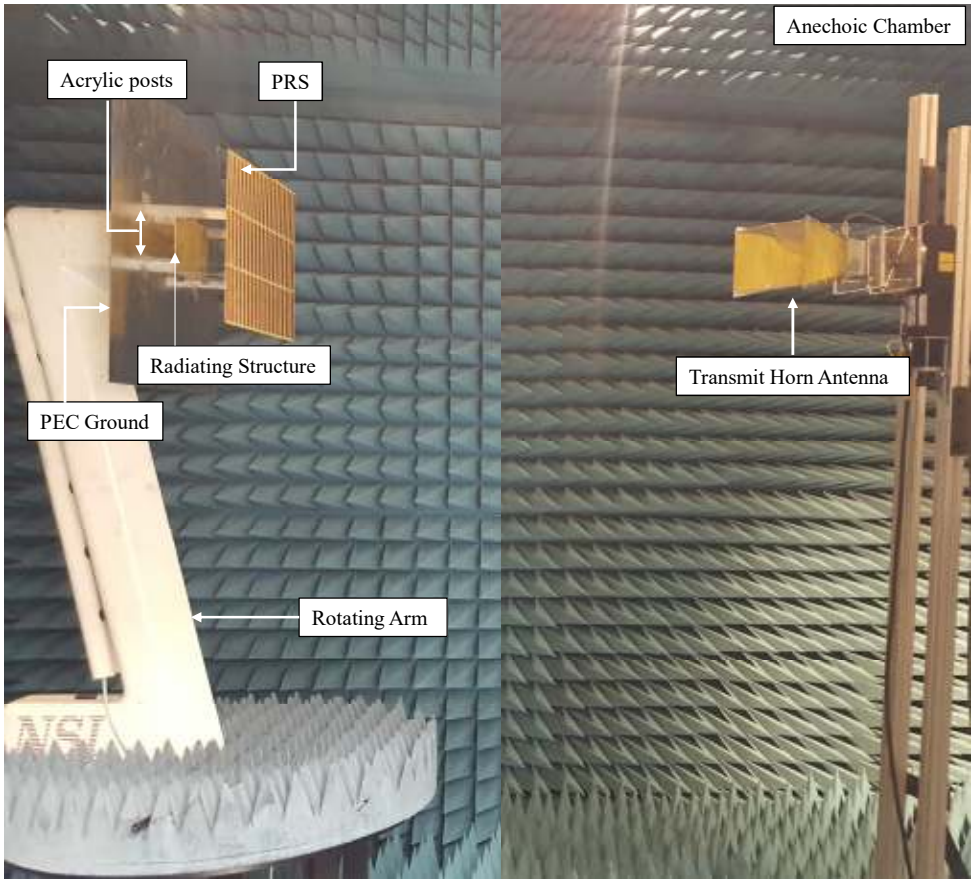

Fig. 5.20 Experimental configuration in the anechoic chamber

Figure 5.20 illustrates the complete model set up for measurements at 1.8GHz frequency, in the fully anechoic chamber where the antenna under test (AUT) is mounted on the horizontally rotating arm acting as a receiver. A transmitting antenna (R&S® HF906 Horn) which has a fixed position was placed at a distance of 2.5m away from the AUT. As discussed previously the alignment of the two corresponding antennas is crucial for accurate measurement results. The configuration in Figure 5.20, represents the set up for a H-Field 2D radiation pattern scan where the complex S-parameters were measured using an Agilent Technologies E5071C ENA Series vector network analyser (VNA) over a range of angles between $\pm 180^\circ$ in 1°steps. The measurements were carried out automatically using the NSI 2000 R system. The PIN diode control voltage was applied using a DC power supply placed outside the chamber in order to have minimum interference with the far-field response. Measurements were also

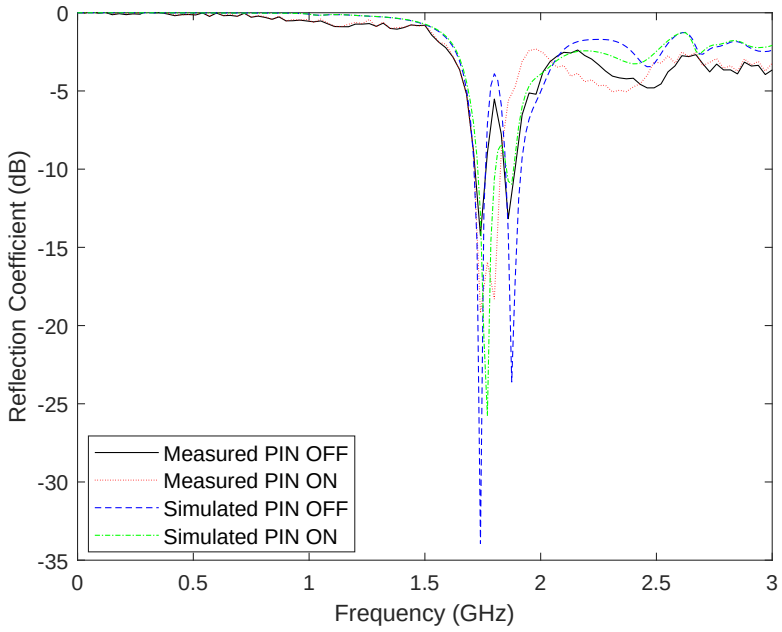

Fig. 5.21 Measured and simulated reflection coefficients with the "ON" and "OFF" state PIN diodes

carried out where the AUT was replaced with a (R&S® HF906 Horn)with known gain. The S21 measurements of the known antenna demonstrated in Section 3.4 and the AUT were then compared to infer the realized gain of the antenna using the equation (3.11). Simulation and measurement results of the AUT were carried of for comparison. The measured reflection coefficients are presented in Figure 5.21. It can be revealed that reflection coefficient magnitude of $-18.3dB$ and $-5.5dB$ is achieved for ON and OFF diode states respectively. Compared to the simulations results presented in Figure 5.11 and 5.13, the measured results are higher due to the impurities due to soldering is developed while constructing the model. The simulated and measured realized gains for co and cross polarizations with ON and OFF state PIN diodes are shown in Figure 5.22 and Figure 5.23. The operational frequency of the structure has been considered as $1.8GHz$. Evaluating the results achieved in Figure 5.22 and Figure 5.23, it can be affirmed that considerable difference between ON and OFF states of the PIN diodes can be observed. At boresight where $\phi = 0^{\circ}$ there is a maximum gain of $15.8dBi$ for the OFF diode state as compared to a gain of $7.3dBi$ in the ON state towards the

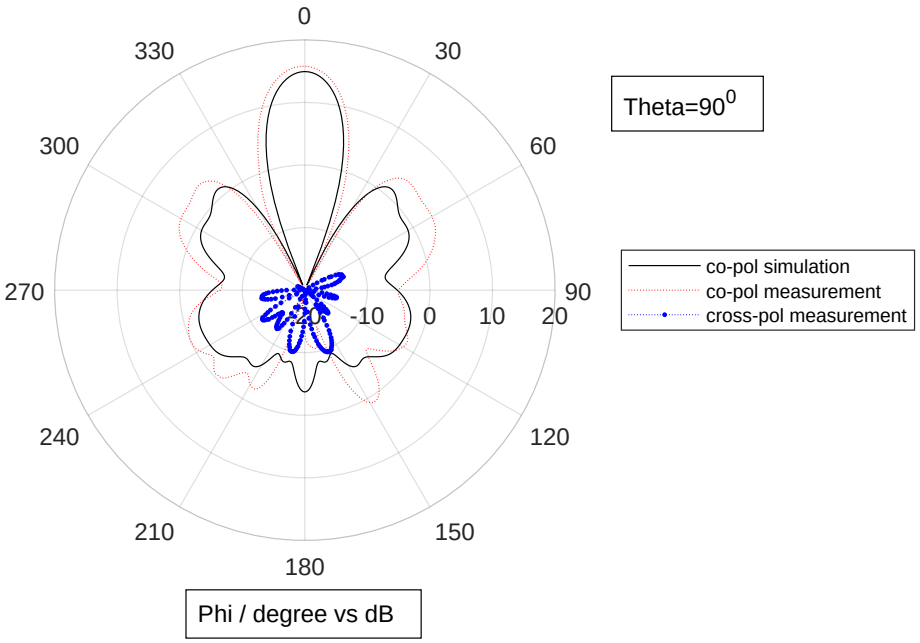

Fig. 5.22 Measured and simulated co and cross polarised OFF state H-plane radiation pattern 1.8GHz frequency

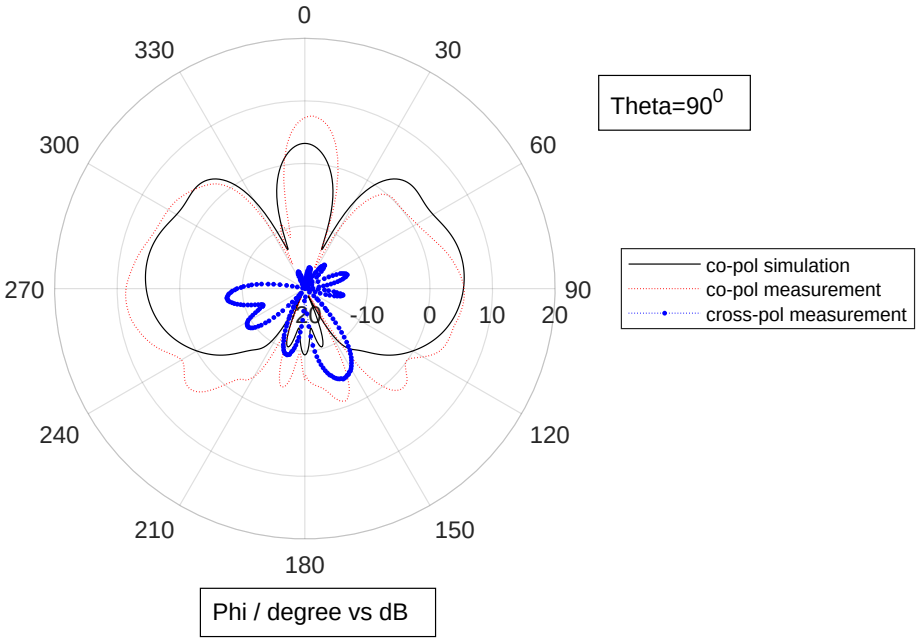

Fig. 5.23 Measured and simulated co and cross polarised ON state H-plane radiation pattern 1.8GHz frequency

same orientation. The cross-polarization with both "ON" and "OFF" modes have a $20dB$ less power is radiated illustrating a very low interference with the alternative polarization which is not desired. Similarly analysing the behaviour of radiation pattern towards end-fire direction where the angle of 270° is considered, the gain switches between $-6.5dBi$ and $8.6dBi$ for the OFF and ON diode states respectively. It can be seen that there is an asymmetry in the pattern giving an OFF/ON gain at 90° of $-5.0dBi/5.5dBi$ which can be related to the tolerances of the components and the soldering increasing inductance which would change the size of the parasitic effecting the behaviour. Considering the simulation result it can be seen that a good corroboration has been achieved between the measured and the simulated results where an endfire switching between $-6.9dBi$ to $5.59dBi$ and at the boresight gains of $14.9dBi$ and $3.2dBi$ is attained. For the completeness of the results the elevation plane (E-plane) far-field plots are illustrated in Figure 5.24 where a good corroboration between both planes have been attained.

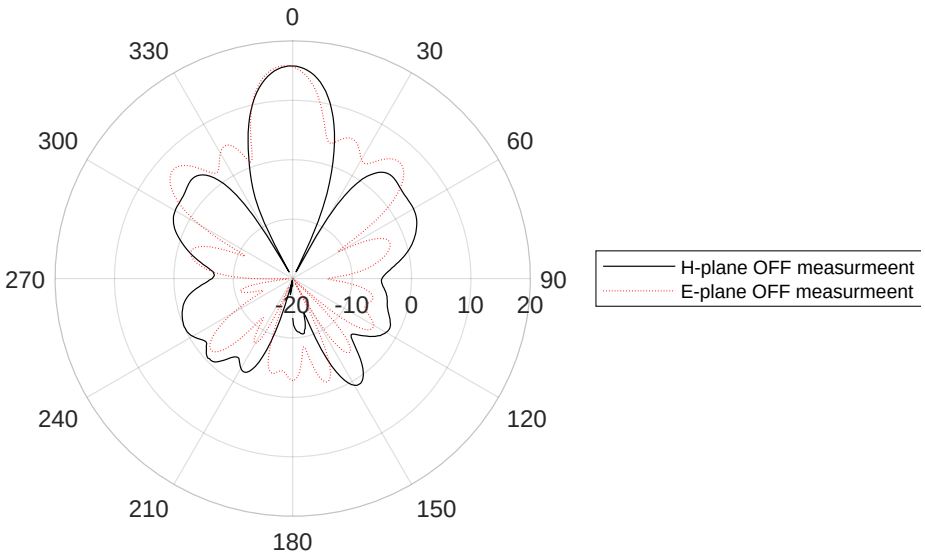

Fig. 5.24 Measured co-polarised OFF state E-plane and H-plane radiation pattern at $1.8GHz$ frequency

5.7 Summary

In this chapter a low complexity high gain beam switching antenna with the use of Fabry Pérot topology with introducing a PRS has been proposed. The main objective of the chapter is to present a reliable low cost structure to replace conventional techniques used for pattern reconfiguration such as mechanically tuned structures and also phased arrays [87, 88] which are high in cost, complex structures. It is a challenging and time consuming process for the field engineers to identify any problems and assure the maintenance for the complex structures where the effectiveness of time usage is crucial for the client utilizing the service. However in this chapter it has been presented and proven that the approach of using only two active elements (PIN diodes), and partially reflecting surface a measured gain of $15.8dBi$ is achieved at the boresight $\phi = 0^\circ$. Whereas the beam is switched $\pm 90^\circ$ to endfire direction with "ON" state PIN, resulting with a $8.6dBi$ peak gain which is switched from $-6.5dBi$ with "OFF" state. Further improvement on the proposed design could be done to further enhance the gain and consider the dual polarised version of the model to adopt and minimise the possibilities of interference within the spectrum which will be discovered in the upcoming chapter.

Chapter 6

A Dual Polarized Beam Reconfigurable High Gain Antenna Operating at 3.6GHz

Within Chapter 5 it has been proved with both simulation and measured results that a significant beam switching can be attained with the aid of parasitics aligned on either side of a radiating dipole where the lengths are varied with PIN diodes. The boresight gain as well as the endfire radiation is discovered to be highly dependent on the partially reflected surface placed above the ground and the radiating structure. However regarding the theory mentioned in Chapter 3 about polarization, the spectrum can be used more effectively if different polarizations are to be used within the same frequency band which in return will decrease the inference. The scope of this chapter is to discover the possibilities of achieving beam switching at azimuthal (H-plane) and elevation (E-plane) planes where further enhancement of the gain at the boresight direction is targeted. The new generation wireless communications will be using multiple frequency bands in order to provide a better infrastructure for the users where the capacity and congestions within the preallocated frequency bands are crucial. It is most likely to open up a new spectrum for mobile communications where $3.4-3.8GHz$ band is a strong candidate [89] where International Telecommunication Union (ITU) will be releasing the Europe and UK next generation 5G communication bands in 2020. For the evaluation purposes a different partially reflecting structure will be designed consisting

square patches to achieve gain enhancement in both azimuth and elevational (H and E) planes. As a feeder two orthogonally positioned dipoles have been designed and deployed to generate polarization diversity with boresight high gain and endfire switching. Design procedure supported with simulation and anechoic chamber measurements have been evaluated in this chapter.

6.1 Dual Polarized Beam Reconfigurable Concept with Gain Enhancing Partially Reflecting Surface

A cross-section of the proposed dual polarized pattern reconfigurable antenna is illustrated in Figure 6.1 and Figure 6.2 consisting of a radiating element with two half wave radiating dipoles positioned perpendicular to each other at each side of the dielectric substrate $FR-4$ with a thickness of $0.8mm$ ($\varepsilon_r = 4.3, tan\delta = 0.025$). In order to achieve the beam steering property, previously proven concepts in Chapters 4 and 5 are considered where half wave long parasitics are placed at a $\lambda/2$ distance apart from the radiating element. The antenna is designed to operate at a frequency of $3.6GHz$ where PIN diodes are used in between the

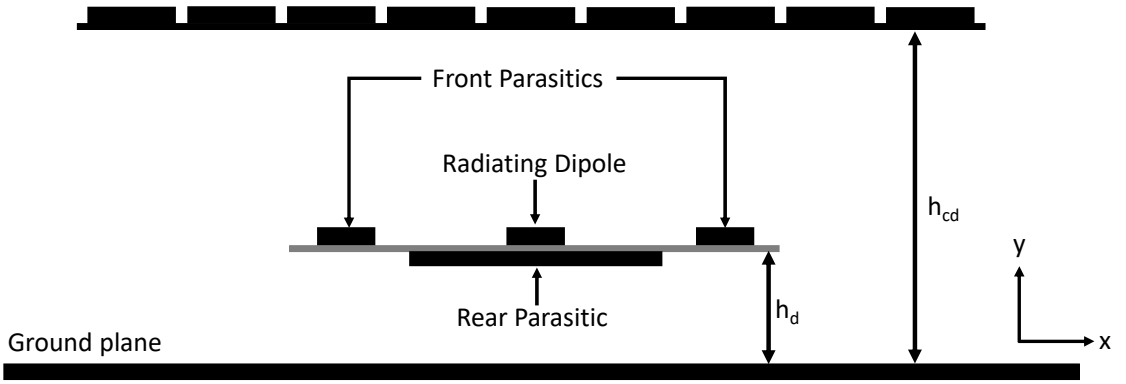

Fig. 6.1 A cross-section of the complete model for dual polarized high gain beam switching antenna

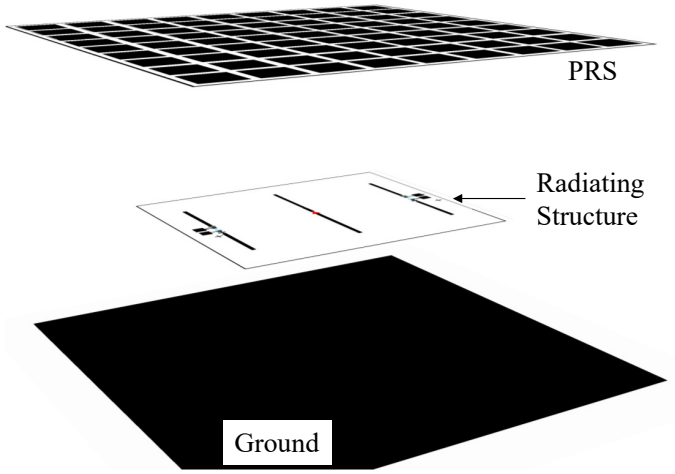

Fig. 6.2 A 3D representation of the modelled structure illustrating PRS the radiating structure and the ground plane

parasitic strips to adjust the lengths of the strips for beam switching from boresight to endfire directions. In order to cancel out the effects of DC biasing on the current behaviour along the parasitics, capacitors are included as well as the inductors which are used as RF chokes as discussed previously. With the use of capacitors further tuning on the parasitic strip lengths are targeted in order to reduce the boresight radiation whilst the PIN diodes are switched ON and the desired antenna radiation direction is endfire. For further gain enhancement a partially reflecting surface formed of square patches has been implemented where a cavity is formed with a metallic ground and the spacing has been precisely modified according to the outcomes of Chapter 5. Regarding to these justifications, the gain has been enhanced at the boresight ($\theta = 0^{\circ}$) with two different polarizations.

6.2 Fabry Pérot and PRS Square-patch Unit-cell Analysis

The methodology and techniques of using Fabry Pérot anti-resonance condition as well as resonance condition to control the main beam direction as well as enhancing the gain towards the boresight direction are discussed in Chapters 4 and 5. Regarding the outcomes achieved within these chapters the implementations of the Fabry Pérot cavity distance as well as the

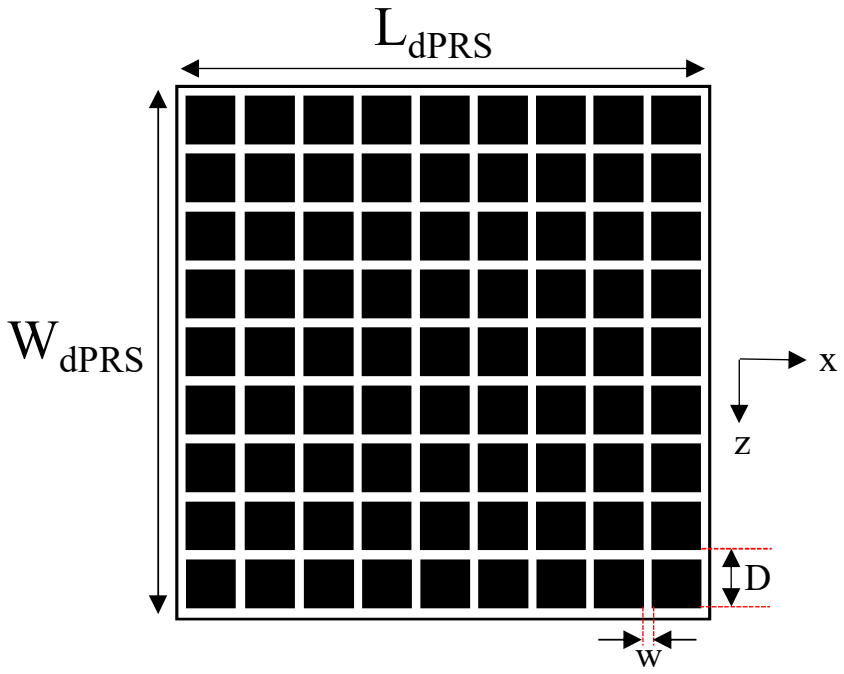

Fig. 6.3 Dual polarized partially reflecting surface complete model

separation of the parasitics will be applied to the dual polarized version of the model. The proposed partially reflector surface of interest is illustrated in Figure 6.3. As visualized the periodic structure is formed of 9 x 9 square patches of copper etched on an dielectric medium of $FR-4$ with a thickness of $0.8mm$ respectively. The total length and width of the dual polarized structure can be stated as $Ld_{PRS} = Wd_{PRS} = 215mm$. The behaviour of such structures were analytically modelled by various authors [90–92], and it has been proved that periodic surfaces formed with patch arrays commonly have a capacitive behaviour where the capacitance is dependent on the inter element spacings. The positioning of the PRS will be customized regarding to the outcomes of Chapter 5 where the cavity height h_c is adopted as λ for a maximum gain enhancement and steering angle. The square patch unit cell analysis is illustrated in Figure 6.4 where the unit cell periodicity is given with D and w represents the spacing between each element forming the periodic structure. The unit cell dimensions represented with L_u and D has been initially attained from [75] and used as a starting point to modify the structure to resonate at the desired frequency of $3.5GHz$ - $3.6GHz$ band, which

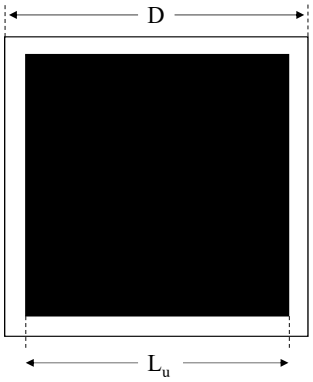

(a) Unitcell

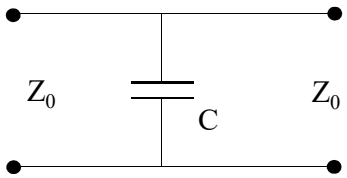

(b) Equivalent circuit of unit cell

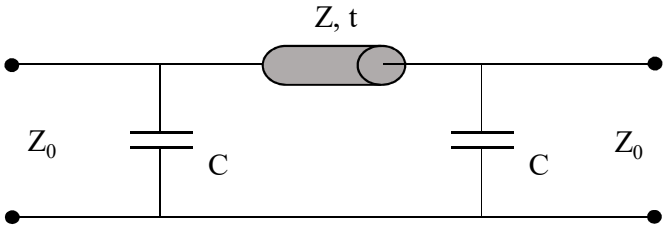

(c) Complete model analysis

Fig. 6.4 Evaluation of a square dual polarized unit cell parameters with a single cell and complete model equivalent circuit representation

is expected to be one of the next generation cellular transmission frequency band. In order to adjust the dimensions and inter element spacings of the periodic patches a floquet model with two unit cells has been generated where a frequency domain solver has been used and a parametric study has been carried out to evaluate the transmission matrices $S21$. Similarly to the previously discussed technique in Chapter 5, the effect of the ground is established with insertion of a mirror image of the unit cell which are perfectly aligned with a separation of 2λ which is illustrated in Figure 6.5. The direction of the propagation and electric field is represented with k and E as illustrated in the figure. A highly defined tetrahedral meshing has been set for the Frequency domain solver in the simulation software to achieve convenient

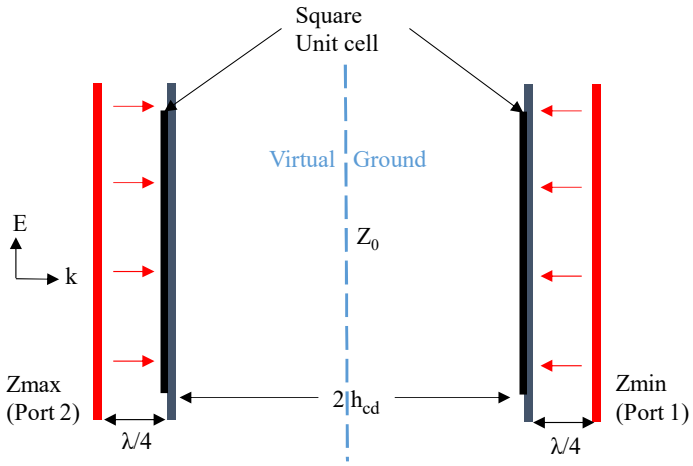

Fig. 6.5 Floquet mode full field analysis with two square unit cells spaced $2h_{cd}$

results for such small structures. As discussed previously the boundary conditions are set to be $\lambda/4$ away from each unit cell along the $Z-axis$ where Z_{max} and Z_{min} ports are located at the edges of the boundary box. Unit cell boundary conditions are applied to generate infinitely long periodic structure. The parametric study of the transmission coefficients are

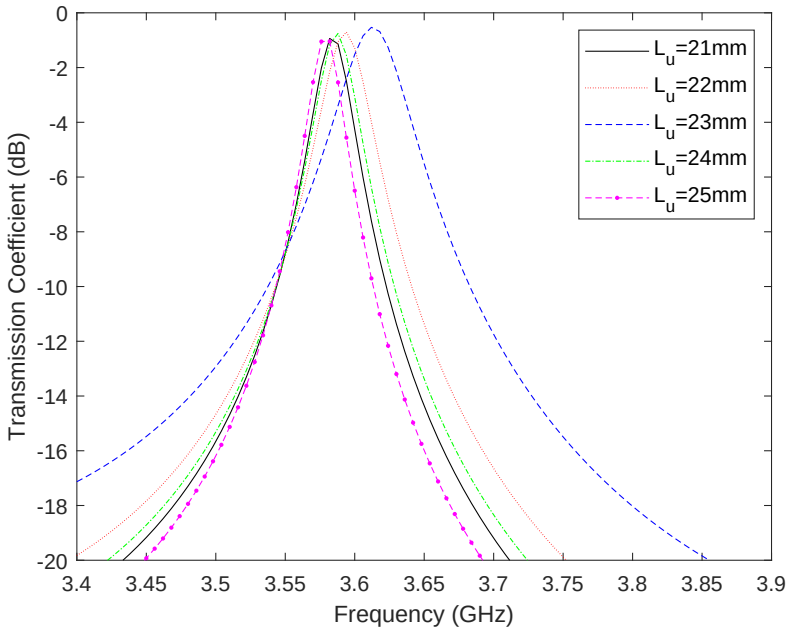

Fig. 6.6 Floquet mode full field analysis with different unit cell dimensions spaced $2h_{cd}$

illustrated in Figure 6.6. The parametric study has been conducted varying square patch unit cell lengths illustrating the resonant behaviour of the unit cell where appropriate assumptions can be made for the complete reflecting surface. The sizes of the patch unit cell has been varied between 21*mm*-25*mm* where the periodicity of the unit cell is dependent on the patch size respectively. It can be observed from the transmission coefficient plot that different patch lengths affects the resonant behaviour of the reflecting surface shifting it up and down the frequency range which can be related to the capacitive behaviour of the patches. In order to generate a better understanding of the frequency selective surface square patch behaviour an equivalent circuit modelling technique has been studied [90]. Due to the relatively small sizes of the square patches to the guided wavelength which is given with $\lambda_g^{\varepsilon_r} = D(\sqrt{\varepsilon_r} + sin(\theta))$ where θ is the incident angle, the model can be specified within the quasistatic region where averaged theory can be applied to determine the capacitance. According to the studies illustrated in [90, 93], the following formulas for different polarizations has been attained and applied to generate the equivalent circuit models for proof of theory. For TE (Transverse Electric) and TM (Transverse Magnetic) polarizations, the impedance of a patch unit cell is considered to be a capacitor and hence the capacitance can be achieved with (6.1) and (6.2);

$$C_{patch}^{TE} = \frac{D\varepsilon_0(\varepsilon_{r1}+\varepsilon_{r2})}{\pi} ln\left(\frac{1}{sin\left(\frac{\pi w}{2D}\right)}\right)\left(1-\frac{k_0^2}{k_{eff}^2}\frac{\sin^2(\theta)}{2}\right) \tag{6.1}$$

$$C_{patch}^{TM} = \frac{D\varepsilon_0(\varepsilon_{r1}+\varepsilon_{r2})}{\pi} ln\left(\frac{1}{sin\left(\frac{\pi w}{2D}\right)}\right) \tag{6.2}$$

where D represents the periodicity of the unit cell, $w = D - L_u$ which is the spacing between the array of patches, k_0 is known as the wave number in free space and hence k_{eff} is the

wave number of the incident wave vector given with $k_{eff} = k_0\sqrt{(\varepsilon_{r1}+\varepsilon_{r2})/2}$. ε_{r1} and ε_{r2} represents the permittivity of different mediums such as free space and dielectric. The equivalent unit cell model is illustrated in Figure 6.4b and with respected to Equation (6.1) the relative capacitance of the unit cell has been calculated to be $C = 0.72pF$. The full field analysis with the complete model where a transmission line of free space with an impedance of 377Ω with a length of $2h_{cd}$ is also included to generate a realistic configuration for the comparison between the simulation and analytical model. The complete model of the equivalent analytical circuit is represented in Figure 6.4c and for evaluation purposes the comparison between the simulation results as well as the analytical model using equivalent circuit theory has been conducted and illustrated in Figure 6.7. It can be clearly observed from the transmission coefficient results that a perfect transmission $0dB$ with almost zero losses has been attained with the equivalent circuit model peaking at the frequency of $3.59GHz$ since it has been designed to operate in a perfect environment where the transmission is achieved over a distance of a wavelength where $\lambda \approx 85.71mm$ and free space impedance is 377Ω. However, with the floquet modal analysis it has losses have been observed through

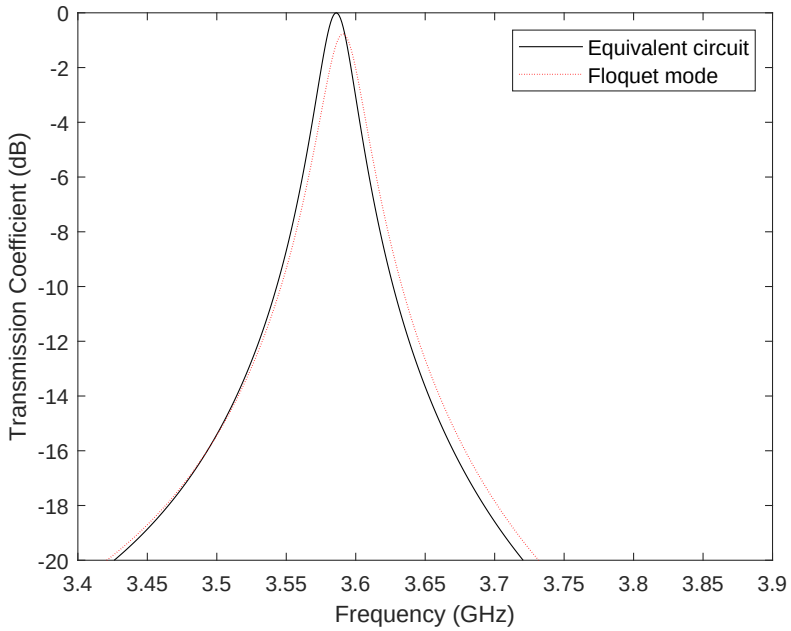

Fig. 6.7 Simulated equivalent circuit and floquet model transmission coefficients for $h_{cd} = \lambda$

the transmission which is acceptable due to the presence of losses throughout the path of electromagnetic waves travelling through different media with losses where impurities exist such as dielectric material $(FR-4)$. Eventually it has been proven that with such unit cell dimensions where $L_u = 21.74mm$ and $D = 23.74mm$ a transmission can be achieved at the operating frequency of approximately $3.6GHz$ which is stated previously to be within the margins of next generation wireless communication frequency bands. However minute differences have been attained with the two analytical models where Floquet mode and equivalent circuit theory is compared, for the proof of principle this was found to be sufficient.

6.3 Dual polarized radiating structure antenna design and evaluation

The top and bottom layers of the prototype antenna design is represented in Figure 6.8 and Figure 6.9. The antenna design has been evaluated regarding the previously made design for high gain beam steering structure. A dipole antenna is considered as the radiating element operating at the resonant frequency of $3.6GHz$ and the parasitic strips are implemented with the same topology regarding the previous chapters which are placed at a distance of $\lambda/3$ away from the radiating dipole. The bottom layer of the antenna can be considered as the 90° rotated version of the top layer model along the y-axis in order to achieve the dual polarization property of the antenna where the dipole has a linear polarization, rotating the antenna along the relevant axis would change the polarization of the antenna. The rotated version of the antenna has been allocated at the rear side of the substrate in order to minimise the co-polarization effects and avoid complex circuitry for feeding mechanisms to ensure phase differences with orthogonal dipole arms. In addition, due to the interference between the orthogonal dipoles placed on the same plane, the matching is affected significantly.
The dielectric of $FR-4$ ($\varepsilon_r = 4.3, tan\delta = 0.025$) with $0.8mm$ thickness has been used as a substrate where a thin layer of copper has been etched as discussed in the previous chapters. Regarding the previous chapters 4 and 5, it can be observed that the parasitic strip length

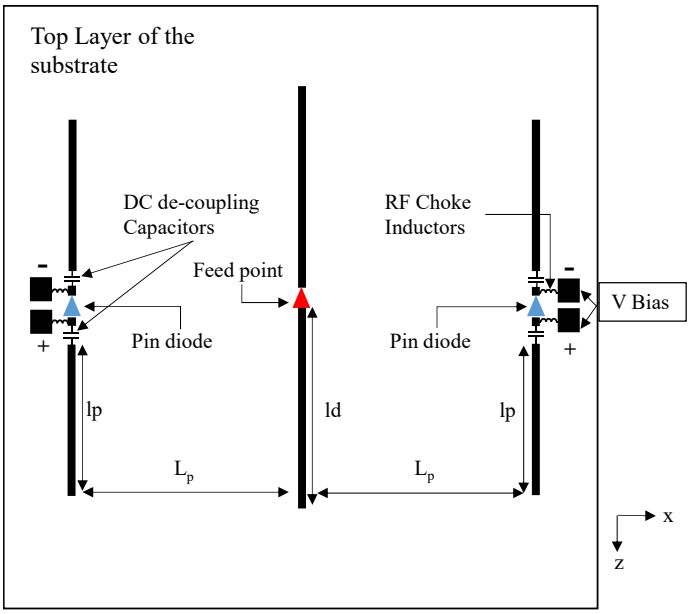

Fig. 6.8 Radiating antenna structure with parasitic strips, components and biasing allocation Top-Layer

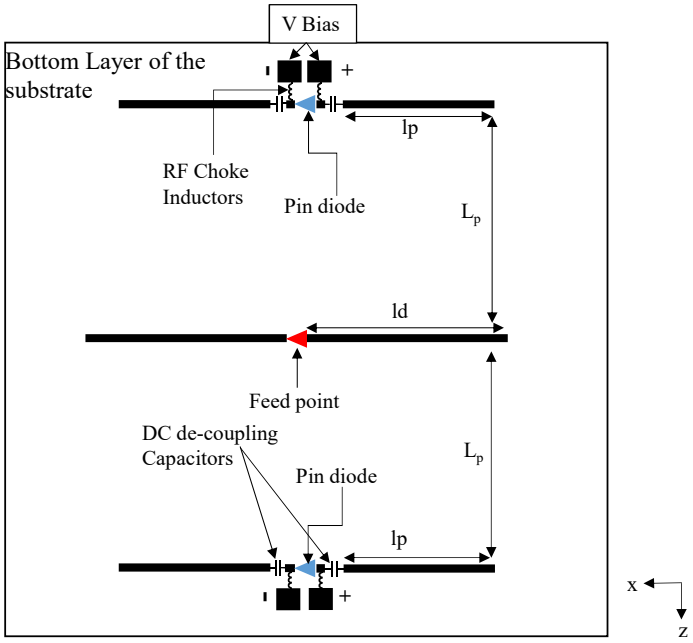

Fig. 6.9 Radiating antenna structure with parasitic strips, components and biasing allocation Bottom-Layer

has a crucial effect on the radiation pattern of the half wave length micro-strip dipole which is used as the radiating element for both planes. According to the findings discovered in the previous chapters, the lengths of the parasitics strips are adjusted to be shorter than the radiating element to attain the more of a capacitive behaviour for a better steering angle with a higher gain towards the endfire direction where as reducing the boresight gain with ON state PIN diodes. As represented in Figure 6.8 and Figure 6.9, a PIN diode (Infineon Technologies BAR64-02V) where the equivalent circuits has been examined previously in Section 5.4, is sufficient at high frequencies and has been included to attain a total length of a parasitic strip $2l_p = 25mm$ when forward biased ON state. With the OFF state PIN diodes the overal length of each strip can be stated as $l_p = 11.5mm$ respectively. However the biasing point of the PIN diodes has been changed to minimize the biasing currents affecting the currents induced on the strips by the radiating element. As represented high impedance inductors $22nH$ (Johanson Technology High impedance ceramic inductors with a $\pm 5\%$ tolerance) are implemented to limit the undesired RF flowing down the biasing cables. Low impedance capacitors $4pF$ are used as DC-decouplers placed at either side of the PIN diodes which in turn can be used as capacitive tuners to adjust the length of the parasitic strips for minimising the boresight radiation when the PIN diodes are switched ON.

6.4 Simulations for Dual-Polarized Full Structure Analysis

For evaluation purposes the model has been generated in the CST Microwave studio where Design Studio has been used to implement the biasing voltage and additional components to achieve the desired radiation pattern behaviour for both polarizations. Radiaton patterns will be studied extensively as well as the scattering parameters to reflect the matching losses where the efficiency of the system will be monitored for the verification of applicable fields of the model.

6.4.1 Cavity height adoption

Regarding the outcomes of the previous Chapter 5, the dual polarised antenna model has been placed a distance of $\lambda/4$ away from the PEC ground plane to generate in phase reflection which would increase the boresight radiation $\theta = 0°$. A partially reflecting sheet formed of periodic square patches illustrated in Section 6.2 is placed a distance of h_{cd} away from the ground plane. Allocating the PRS at a certain distance away from the ground plane as discussed previously in Section 5.5.1 a cavity is formed for further gain enhancement towards the boresight and a better steering angle towards the endfire where $\phi = 90°$. The cavity distance $h_{cd} \sim \lambda$ where $\lambda = 83.3mm$ is attained according to the evaluation process illustrated in Chapter 5. For the proof of the topology which is previously discussed the complete short circuit "ON" and open circuit "OFF" diode state analysis of far field radiation patterns with different cavity spacings height h_{cd} are illustrated in Figure 6.10 and Figure 6.11. According to the complete symmetry between the farfield results with the orthogonally polarized model allocated at the rear side of the substrate, single pair of results has been displayed to represent

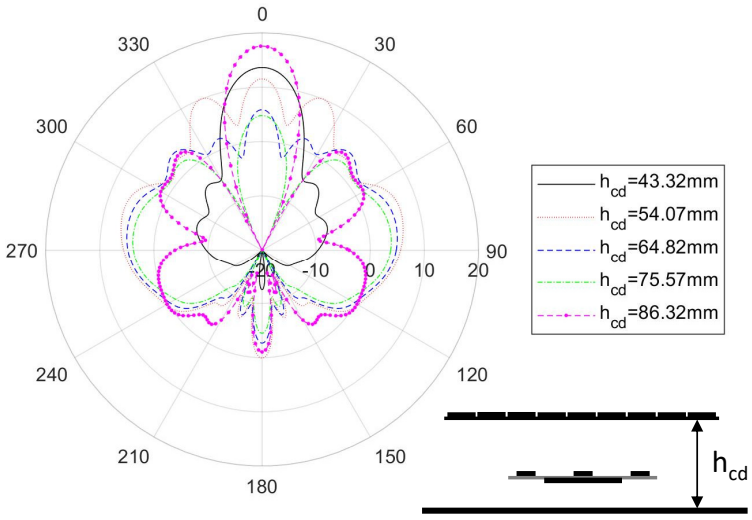

Fig. 6.10 Simulated realized gain patterns for dual polarized model with "OFF" State PIN diodes at the resonant frequency of 3.6GHz

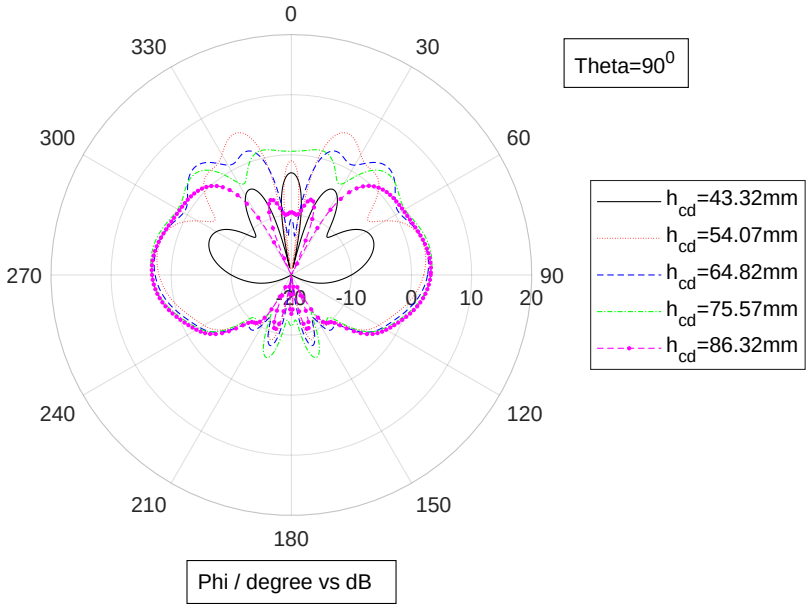

Fig. 6.11 Simulated realized gain patterns for dual polarized model with "ON" State PIN diodes at the resonant frequency of 3.6GHz

both versions. It can be observed from the far field gain plots with different cavity spacings which is varied between $\approx \lambda/2$ and $\approx \lambda$ that, Fabry Pérot resonance condition can be achieved with a cavity height of $h_{cd} = 43.3mm$ where the boresight $\phi = 0^\circ$ a realized gain of $13.63dBi$ can be attained with a very low side and back lobes Figure 6.10. However with ON state PIN diodes, since the affect of the parasitic strips to the current distribution is enhanced, it can be seen that the radiation pattern attained from the system can be referred as unacceptable due to the steering angle and magnitude as well as the high boresight radiation. As illustrated in Figure 6.11 , there has been multiple main lobes created within the short cavity distance achieving a Faby Pérot resonance, whereas according to the perfect symmetry the maximum beam direction can be noted as $\phi = 66^\circ$ and $\phi = 246^\circ$ with a magnitude of $-5.17dBi$. However increasing the cavity height h_{cd} different resonant modes have been attained where arbitrary farfield patterns have been achieved for both "ON" and "OFF" state PIN diodes with the cavity heights of $h_{cd} = 54.07mm$, $64.82mm$ and $75.57mm$. Increasing the distance between PEC ground plane and the partially reflecting surface where the cavity height up to $h_{cd} \approx \lambda$, as discussed in previous chapters, Fabry Pérot anti-resonance mode has been attained. It can be clearly seen from the relative "OFF" state plot that, maximum

realized gain towards the boresight direction where $\phi = 0^\circ$ is achieved to be $17.55dBi$ along the endifire direction $\phi = 10^\circ$ and $\phi = 170^\circ$ due to the perfect symmetry, gain of $-9.4dBi$ is attained. The formation of the nulls towards the endfire directions can be noticed clearly where with "ON" state PIN diodes with the full length of parasitic strips, the beam is radiated towards the endfire direction filling up the nulls and achieving a beam switching along the H-plane. Maximum steering angle with the application of latest adjustments can be stated as $\phi = 269^\circ$ and $\phi = 89^\circ$ where peak realized gain at the endfire direction is approximately $4.4dBi$. The boresight radiation with "ON" state PIN diodes can be noted as $\approx -10dBi$ resulting with a $27dB$ of switching towards the boresight direction with perfect conditions of open and short circuiting the parasitic strips. Generating the results within the Design Studio Suite where components with tolerances are implemented to the model, there has been a significant difference at the boresight switching. The results in Figure 6.12 illustrates "ON" and "OFF" state PIN diodes with a cavity height of $h_{cd} \approx \lambda$. With the "OFF" state PIN diodes where $0V$ biasing voltage has been applied to achieve reverse biasing where the parasitic strips are not connected, the boresight realized gain of $16.8dBi$ and endfire radiation of $-12.57dBi$ at $\phi = 84.8^\circ$ and $\phi = 264.8^\circ$ has been achieved. With the "ON" state PIN

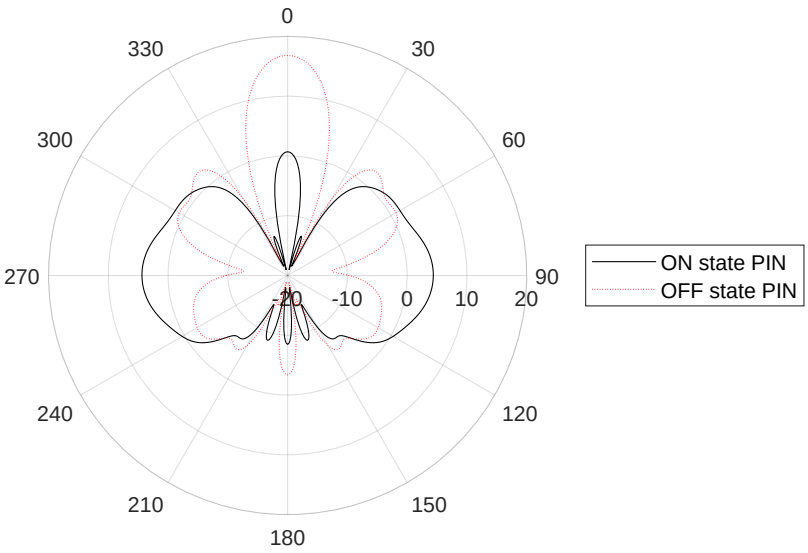

Fig. 6.12 Simulated realized gain patterns for dual polarized model with "ON" and "OFF" State PIN diodes at the resonant frequency of 3.6GHz

diodes where $1.5V$ of DC voltage is applied to the system, a boresight $\phi = 0^\circ$ gain of $0.7dB$ along with the $4.2dBi$ gain towards the endfire direction can be clearly observed. As a result where more losses are introduced to the model including the tolerances of the components as well as the effect of operating in high frequencies on components led to a boresight switching of $16.1dB$ as well as an endfire switching of $16.8dB$ respectively. For the completeness of the results, the configuration with "ON-OFF" PIN diode states are illustrated in Figure 6.13 with different cavity heights h_{cd} varying between $\lambda/2$ and λ. According to the biasing differences on each parasitic strip where parasitic lengths are adjusted, the "ON" state PIN parasitic side has a longer length as explained previously which is the resonating side and the "OFF" state side does not have a significant effect on the pattern therefore a boresight gain as well as an endfire radiation has been attained. Positioning the partially reflecting surface with an height of $86.32mm$, a peak radiation of $9.7dBi$ towards the boresight $\phi = 3^\circ$ as well as an endfire radiation $4.12dBi$ at $\phi = 260^\circ$ is observed in Figure (6.13).

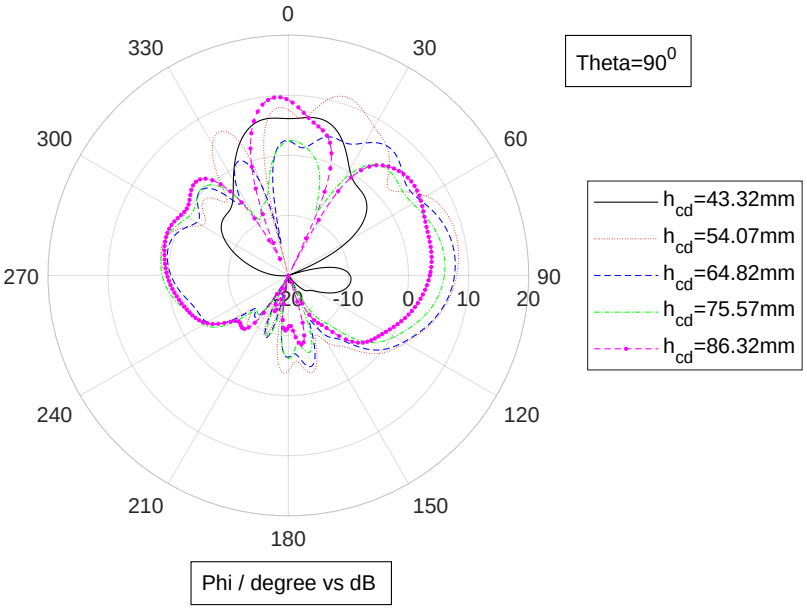

Fig. 6.13 Simulated realized gain patterns for dual polarized model with "ON-OFF" State PIN diodes at the resonant frequency of 3.6GHz

6.4.2 Simulations for verification of constructed model effectiveness

It has been discussed and explained previously in Section 3.1.3 and Section 5.5.3 that the efficiency of an antenna is directly related to the power usage of the antenna where the ratio of delivered and radiated power by the structure is considered. Radiation and total efficiency of the designed model over a range of frequencies have been plotted with "ON" and "OFF" state PIN diodes as illustrated in Figure 6.14. Considering the "OFF" PIN diode state, the radiation efficiency can be observed to be 90% over $1GHz$ frequency band. The losses are mainly due to the presence of the lossy substrate $FR-4$. However the total efficiency of the model has shown a considerable decrease where a total efficiency of 57% at the desired frequency has been achieved. This decrease on the efficiency is predominantly dependent to the miss match caused by the insertion of the PRS which is discussed in the previous Chapters (4 and 5). However a practical solution can be applied to improve the matching of the antenna at the desired frequency or over a range of frequencies with the aid of a matching circuit using passive components (capacitor and inductors). Switching

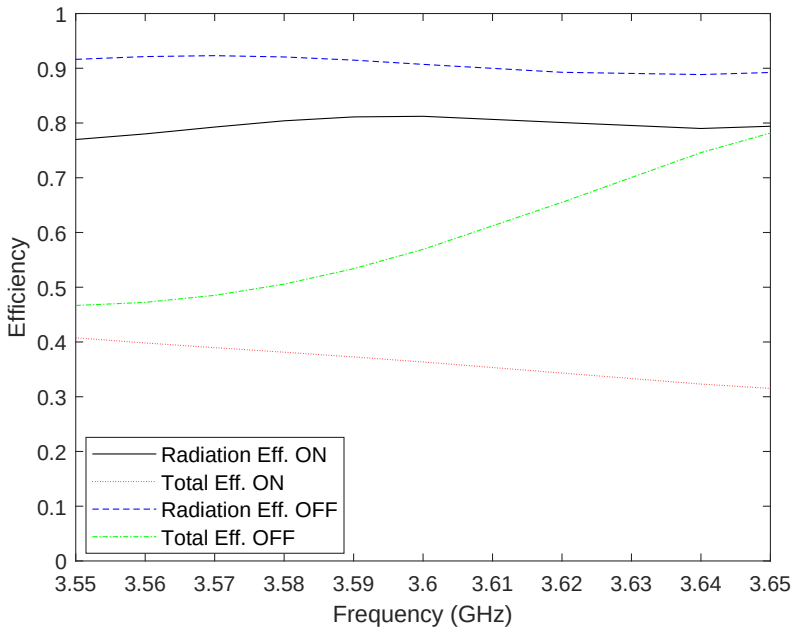

Fig. 6.14 Simulated total and radiation efficiency over frequency with "ON" and "OFF" state diodes for dual polarized model

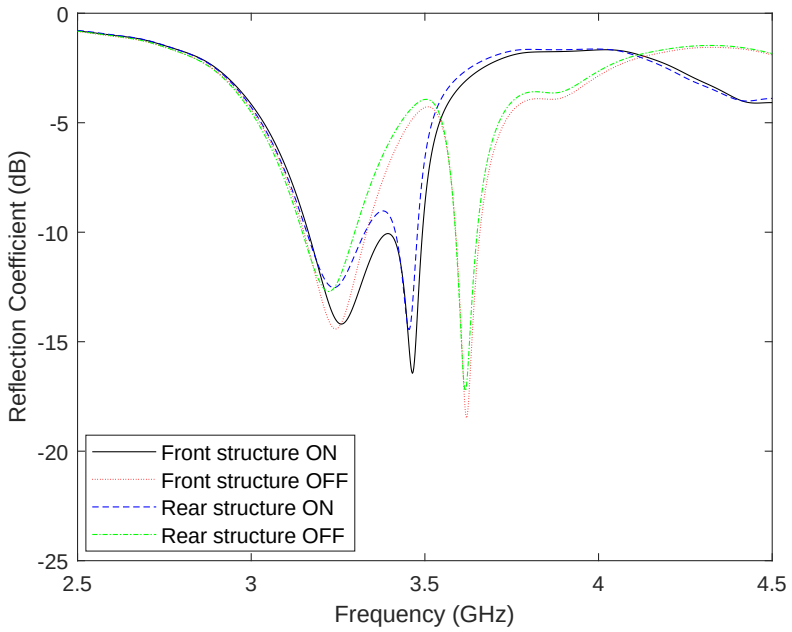

Fig. 6.15 Simulated reflection coefficients over frequency for both structures front and rear side of the dielectric substrate with "ON" and "OFF" PIN diodes states

"ON" the PIN diodes 81% of radiation efficiency has been achieved. Including the losses mentioned previously where PIN diode, inductor and capacitor resistance and tolerances dominate, a total efficiency of approximately 40% has been attained. The simulated reflection coefficients $S11$ for the "ON" and "OFF" state PIN diodes for the both the structures allocated at front and rear of the dielectric substrate are illustrated in Figure 6.15. Considering the reflection coefficient results, it can be clearly stated that the front and the rear radiating structures almost have identical reflection coefficients. With the "ON" state PIN diodes it has been observed that $3.37dB$ return loss has been achieved due to the large amount of mutual coupling between the full length parasitic strips as well as the reflecting waves from the PRS interfering with radiating dipole. However at the desired resonant frequency of $3.6GHz$, switching the PIN diodes to the "OFF" state, a larger return loss magnitude of $13.34dB$ is realized where only the PRS effect is seen meaning more of the power delivered to the antenna has been radiated and hence this ratio is directly related to the efficiency of the designed model. The data transfer within a channel requires a specific bandwidth depending on the use of applications where a typical communication system bandwidths are known to

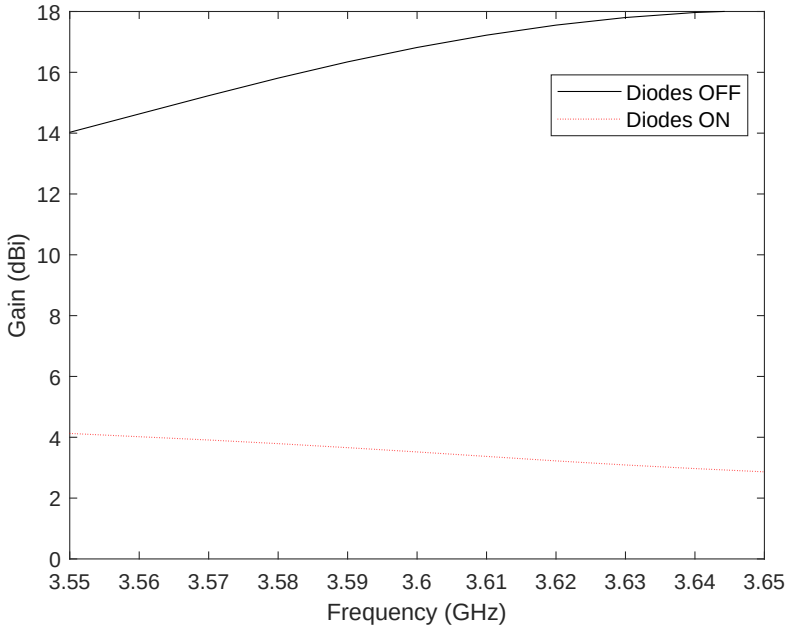

Fig. 6.16 Simulated realized gain over frequency with "ON" and "OFF" state diodes with dual polarized model towards the boresight

be 20MHz where predictions without being certain, up to 100MHz has been considered for the next generation communication systems where higher data rates are targeted. Therefore the gain over frequency plot within a 100MHz margin is illustrated in Figure 6.16. With the "ON" state diodes the variation over 100MHz frequency band with a center frequency of 3.6GHz which can be accepted as a wide bandwidth is achieved to be within 0.6dB. It is certain that over a 20MHz band the gain is stable where the variation is within 0.5dB which is applicable for many current and future communication applications.

6.5 Experimental Results for Dual Polarized Model

As stated previously in the high beam steering single polarized model, the prototype has been manufactured using PCB etching techniques where both sides of the $FR-4$ substrate have been used for different polarizations. In order to conduct the measurements a $\lambda/4$ balun with semi rigid coaxial cable with SMA connectors has been manufactured for the feeding mechanism of the prototype antenna. As illustrated in the Figure 6.17 two independent feeding mechanisms have been manufactured using flexible semi rigid coaxial cables for the ease of carrying out measurements for different radiating structures allocated on top and bottom layers of the dielectric substrate. The total length and width for the resonating structure can be defined as $60mm$ where the semi rigid coaxial lengths are adjusted for the installation of the system in the Anechoic chamber. Increasing the desired resonant frequency

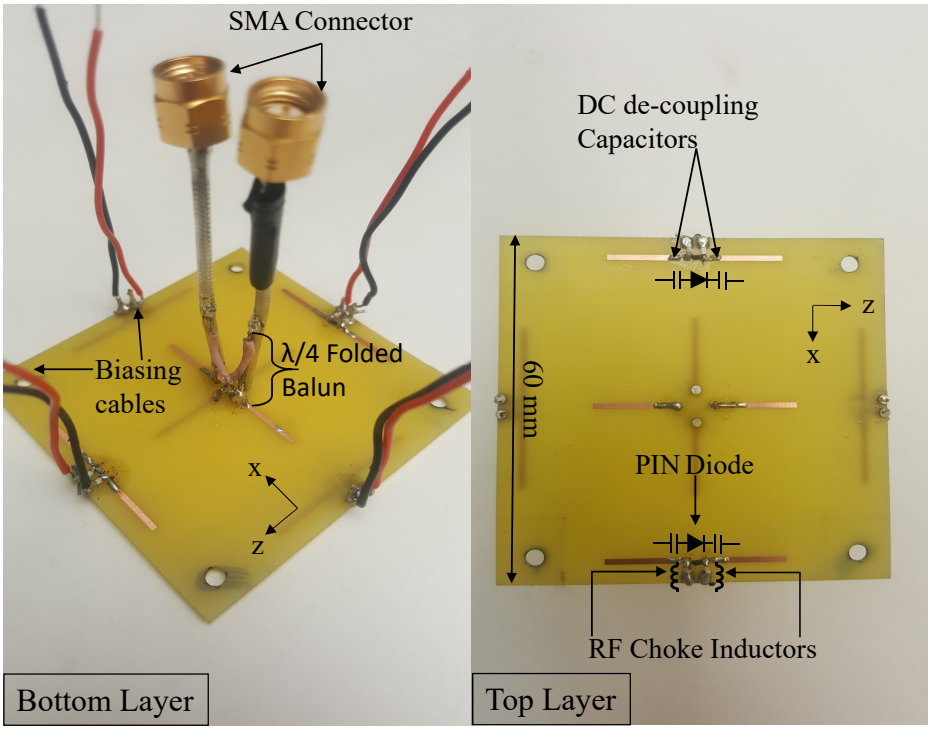

Fig. 6.17 Radiating dual polarized structure with top and bottom view including the feeding mechanisms

decreases the size of the radiating structure regarding to the relation between the operating frequency and the operational wavelength therefore the component sizes which have been soldered are relatively small which can be observed in Figure 6.17. In order to generate a better understanding, components are represented with their corresponding symbols and their allocations on the radiating structure. The two radiating structures are placed on each side of the dielectric substrate in order to minimize the surface currents and hence generate an isolation between the two adjacent structures which would reduce the interference and hence cross-polarization. The experimental set up of the dual polarized high gain beam reconfigurable model in the fully equipped anechoic chamber is illustrated in Figure 6.18 where the antenna under test is placed on the rotating platform which rotate both horizontally along azimuth and elevation planes. The transmitting antenna of (R&S® HF906 Horn) has been perfectly aligned with the receiver to achieve precise and accurate measurement results which is positioned a distance of 2.5m away from the AUT as previously discussed in Section 5.6. The system adjustments illustrated in Figures 6.18 and 6.19 has been applied whilst the front radiating structure is considered, however the 2D H-pattern plots for the rear

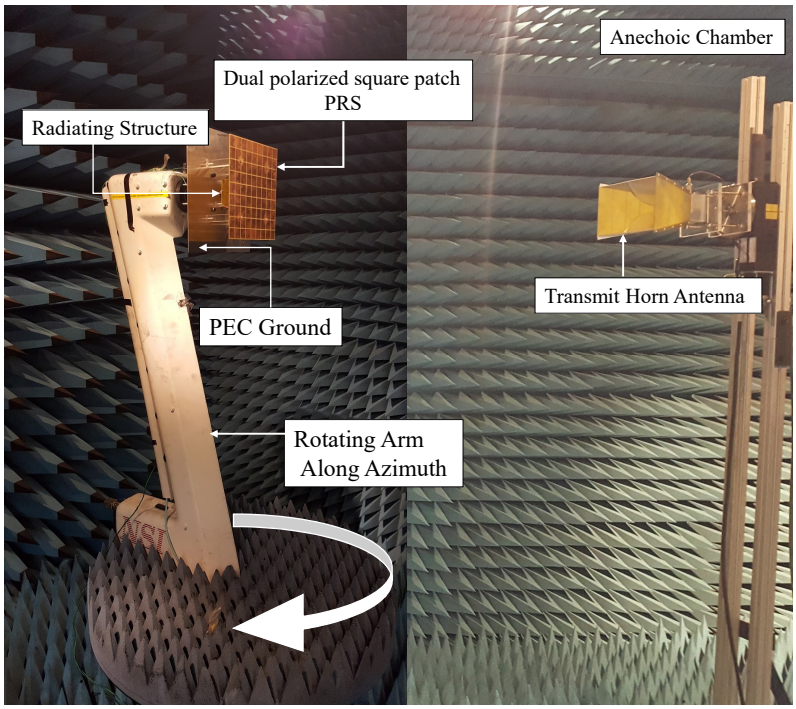

Fig. 6.18 Experimental configuration in the anechoic chamber for the dual polarized model

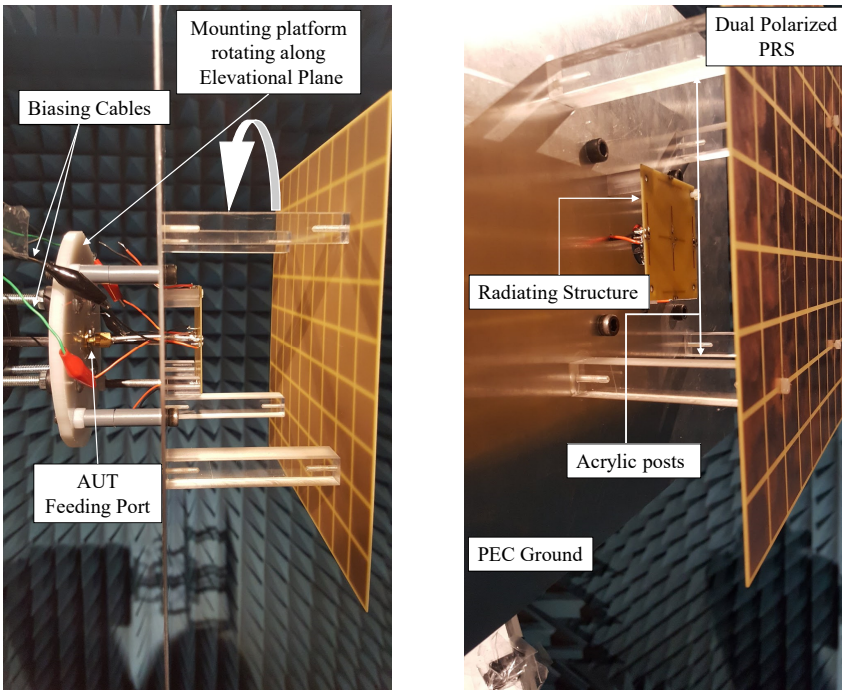

Fig. 6.19 A detailed capture of the experimental set up in the anechoic chamber for the dual polarized model

radiating structure is attained with a 90 rotation along the elevation plane of both the AUT and the transmitting horn antenna. In each case, with the aid of a VNA Agilent Technologies E5071C ENA Series vector network analyser connected to both ports (AUT and Transmit antenna) in the chamber, a range of angles within $\pm 180^{\circ}$ with 1° increments has been scanned and the scattering parameters have been measured where 2D H-Field radiation patterns are generated automatically with NSI 2000R system. Regarding the detailed explanations in Chapters (3, 4 and 5) where a reference horn antenna with a known gain is used to compare and ascertain the realized gain of the AUT using the Equation (3.11). Figure 6.19 illustrates a detailed and closer view of the AUT within the chamber mounted on the rotating arm where the biasing connections and the feeding mechanism can be observed clearly. Simulation and measurement results of the AUT has been carried out for the comparison where the return loss(S11) of the manufactured model was measured using a Rohde & Schwarz ZVL network analyzer. The set up for the S11 measurements are represented in Figure 6.20. The AUT has been connected to the VNA with a 50Ω coaxial cable where both structures at the front and rear side of the substrate has been tested separately with both "ON" and "OFF" PIN diode

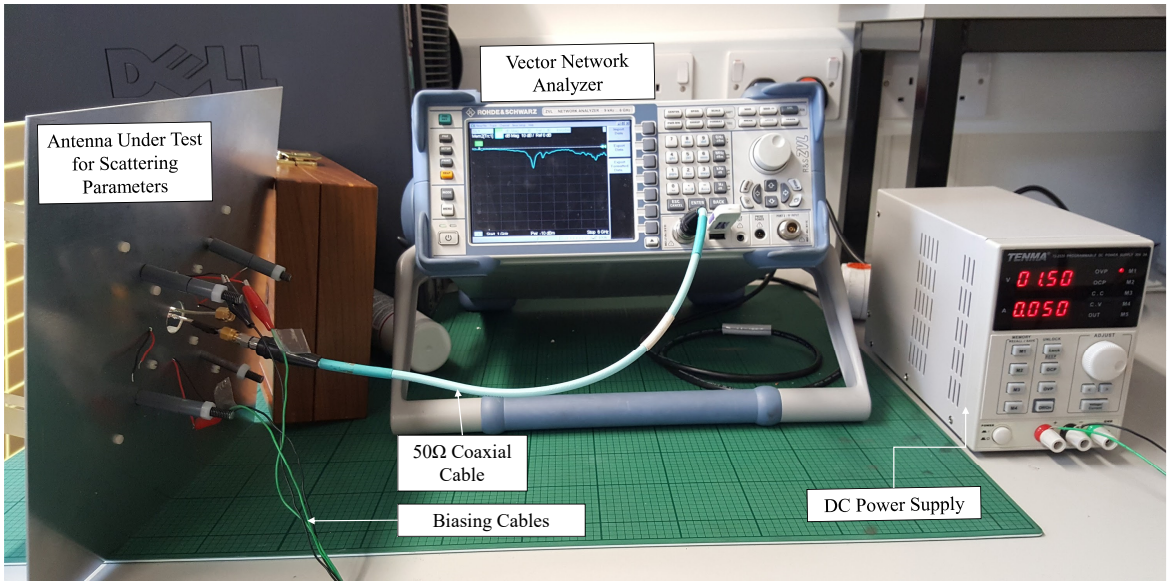

Fig. 6.20 A detailed capture of the experimental set up in the anechoic chamber for the dual polarized model

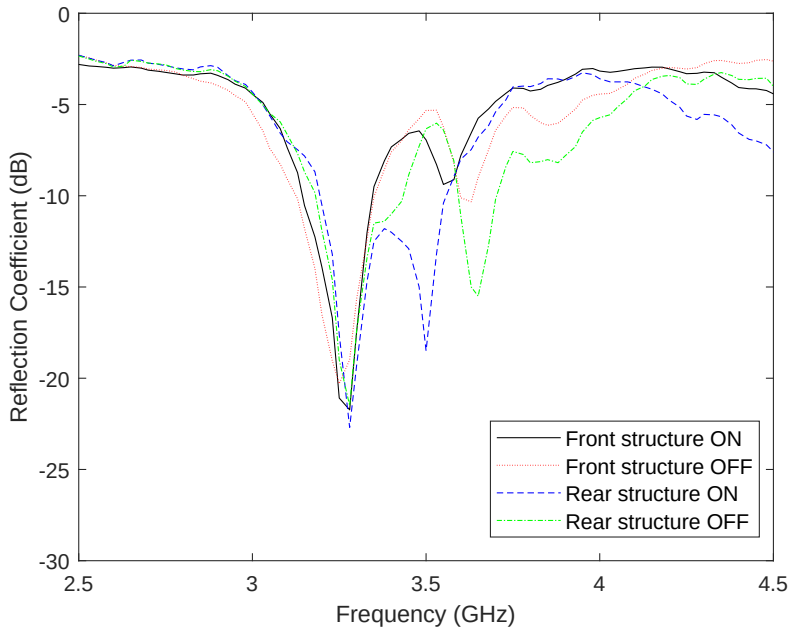

Fig. 6.21 Measured reflection coefficients over frequency for both structures front and rear side of the dielectric substrate with "ON" and "OFF" PIN diodes states

states which is controlled with a biasing voltage of $1.5V$ and $50mA$ from the DC power supply. Figure 6.21 represents the reflection coefficients $S11$ in dB versus a range of frequencies between $2.5GHz$ and $4.5GHz$. Examining the measured results attained from the VNA, it is revealed that the front and the rear radiating structures have almost identical reflection coefficients at the desired frequency of $3.6GHz$. With the "ON" state diodes, the reflection coefficient magnitude of $-7.8dB$ can be observed. Switching "OFF" the PIN diodes reduces the mutual coupling and hence the interference of the surface currents which are not in phase leading to a lower reflection coefficient of $-10.1dB$ for the front and $-11.1dB$ for the rear radiating structure respectively. Compared to the simulations results illustrated in Figure 6.15, a considerable difference as an improvement have been observed with the "ON" state PIN diodes where the impurities due to the soldering and component resistances reduced the miss match. However with the "OFF" state, the results achieved from both simulations and measurements attain a reflection coefficient magnitude below $-10dB$ which is accepted as a considerably good matching for the manufactured antennas. The simulated and measured co and cross polarized radiation patterns demonstrating the realized gain with "ON" and "OFF"

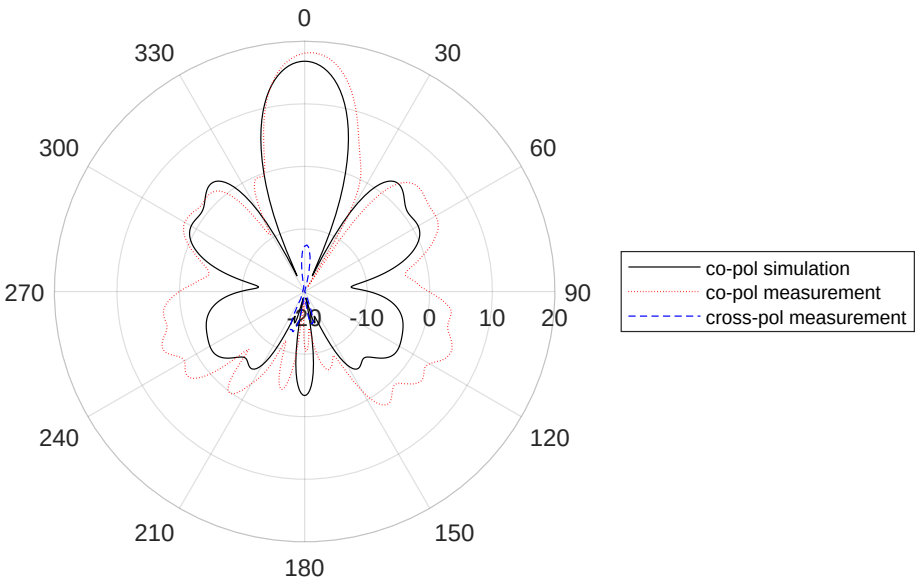

Fig. 6.22 Measured and simulated co and cross polarised OFF state H-plane radiation pattern for front radiating structure at $3.6GHz$ frequency

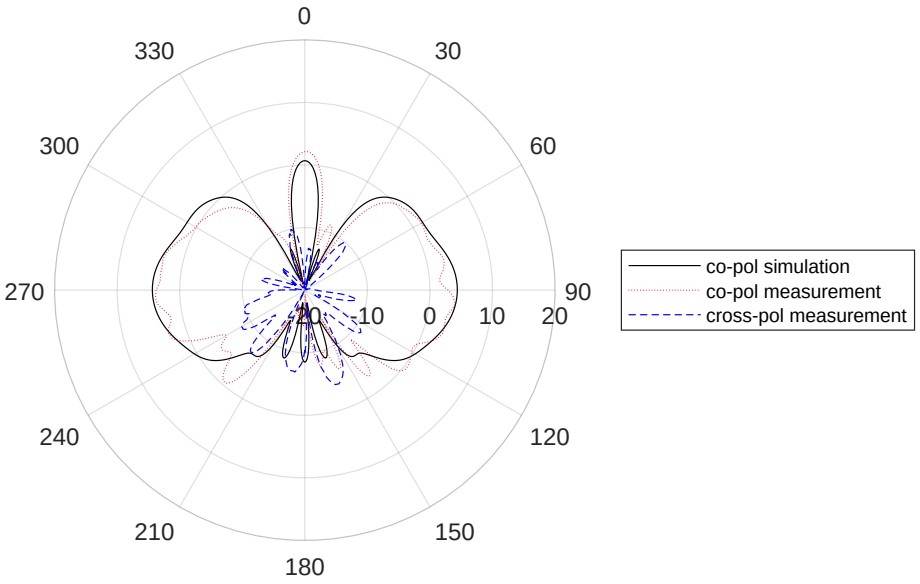

Fig. 6.23 Measured and simulated co and cross polarised ON state H-plane radiation pattern for front radiating structure at 3.6GHz frequency

PIN diode states for both of the structure allocated on the front and rear side are shown in Figures 6.22, 6.23, 6.24 and 6.25. The operational frequency for the structure is considered to be 3.6GHz. Evaluation of the results achieved from simulations and chamber measurements have been illustrated in Figures 6.22 and 6.23, it can be affirmed that a significant difference at the boresight direction where $\phi = 0^\circ$ is achieved by switching the PIN diode states "ON" and "OFF". There has been a good match between the simulation and measurement results. A peak gain of 18.1dBi is achieved at $\phi = 0^\circ$ with the "OFF" state PIN diodes which is compared to the 2.127dBi when the switches are "ON". This results with a 15.97dB beam switching at the boresight direction. The measured cross polarization levels are observed to have approximately $-20dB$ less power radiating with alternative polarizations which is too low to cause an interference. At endfire direction $\phi = 85^\circ$ and $\phi = 265^\circ$ due to the symmetry of the proposed model where the nulls are seen with "OFF" state diodes with a gain of $-3.70dB$, a 3.17dBi gain is achieved when switches are in "ON" state resulting with 6.87dB beam switching. Similarly analysing the Figures 6.24 and 6.25, it is clearly observed that with "ON" and "OFF" state diodes a considerable difference at the boresight direction

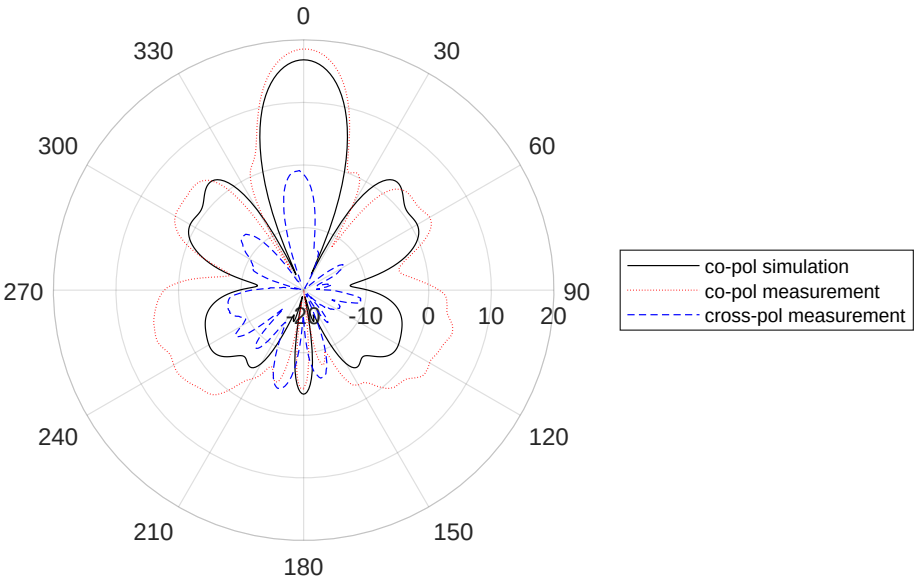

Fig. 6.24 Measured and simulated co and cross polarised OFF state H-plane radiation pattern for rear radiating structure at 3.6GHz frequency

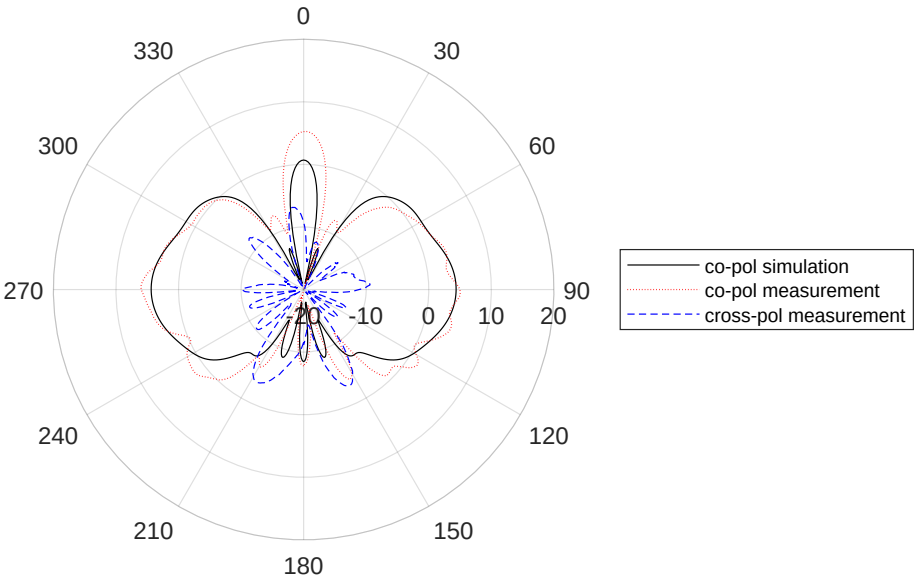

Fig. 6.25 Measured and simulated co and cross polarised ON state H-plane radiation pattern for rear radiating structure at 3.6GHz frequency

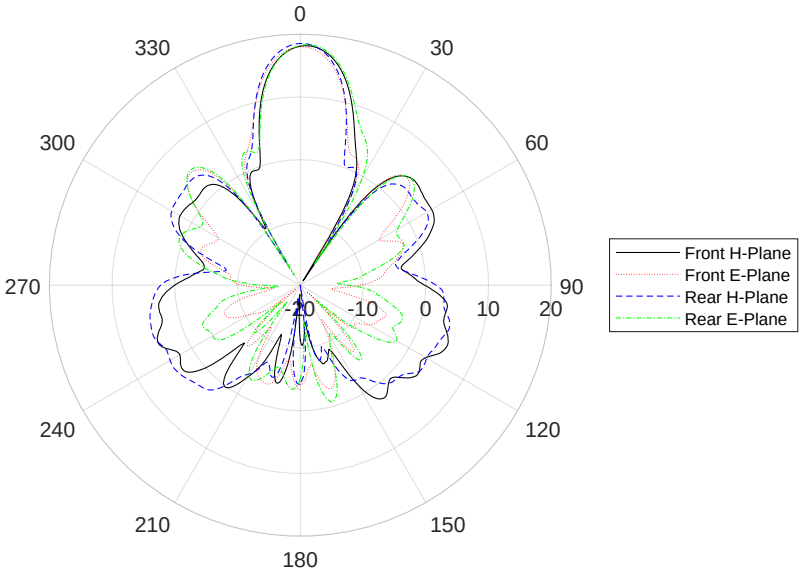

Fig. 6.26 Measured co-polarised ON state E-plane and H-plane radiation patterns for front and rear radiating structures at 3.6GHz frequency

is achieved with a magnitude of 13.3dB where realized gains of 5.23dBi and 18.53dBi is attained respectively. Towards the endfire direction the maximum beam switch is observed at the angle of 78° where "ON" and "OFF" state diode modes generate beam switching of 8.1dB which is reasonably high. Comparing the front and rear radiating structure results it can be visualised that, towards the boresight direction for both "ON" and "OFF" states, the boresight radiation is higher at the rear radiating structure where the dimensions for and parasitic strip allocations for both structures are exactly identical. This can be related to the parasitic strip component tolerances, soldering and impurities while the manufacturing process where the parasitics are made more inductive and higher amount of radiation is reflected with both states. Considering the cross polarization results for both modes, the radiating structure is highly isolated from the unnecessary alternative polarizations which is not desired and causes interference. For the comparison and the completeness of the results E-plane radiation patterns are illustrated in for ON and OFF state PIN diodes for front and rear structures. Considering the Figure 6.27 where the OFF state PIN diode state results were examined, it can be clearly inferred that a good comparison between the H-plane and E-plane patterns

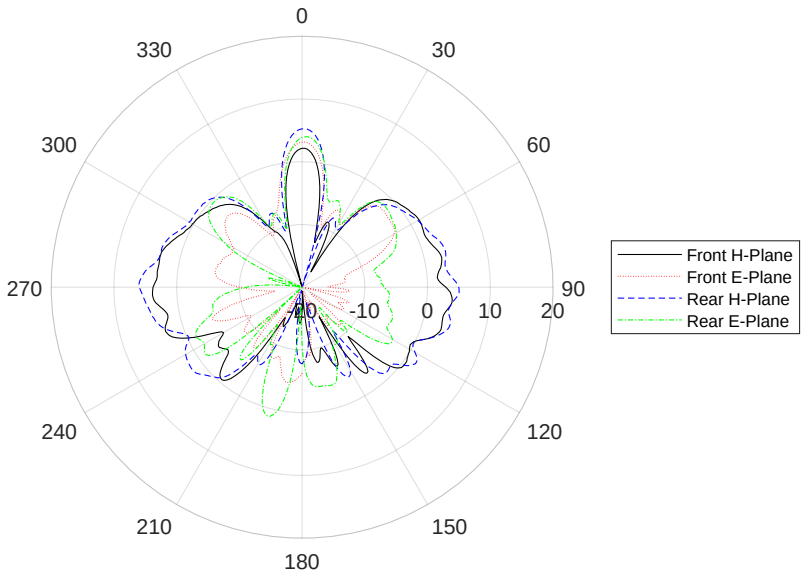

Fig. 6.27 Measured co-polarised OFF state E-plane and H-plane radiation patterns for front and rear radiating structures at 3.6GHz frequency

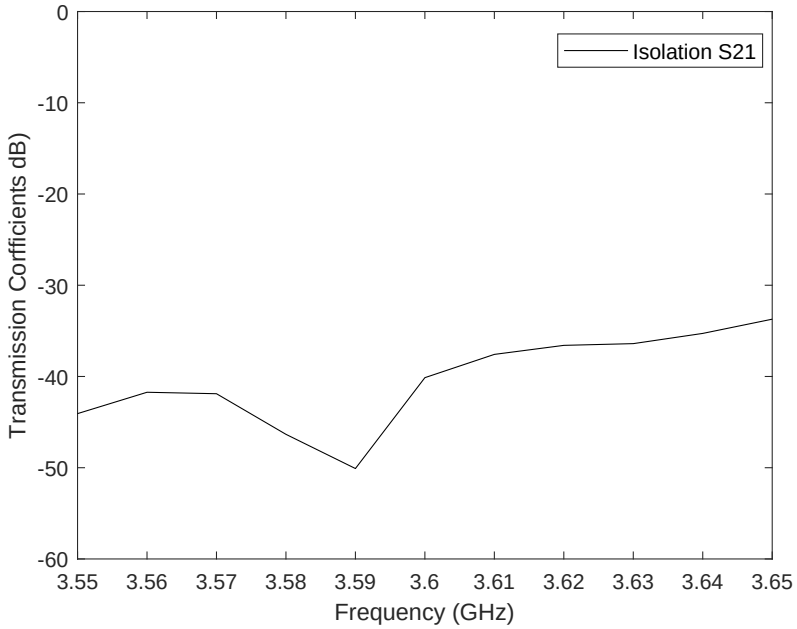

Fig. 6.28 Measured transmission coefficients S21 over frequency for dual polarized model isolation between two adjacent dipoles

for both the structures are achieved. The maximum boresight gains at $\phi = 0^{\circ}$, are almost identical and symmetric for both of the structures. However with the "ON" state results illustrated in Figure 6.26 it is observed that the front structures' E and H-plane radiation patterns attain the same magnitude of radiation towards the boresight where approximately $0.5dB$ difference is noticed. Similarly a good correlation between the rear structure "ON" diode state results are achieved where the difference between the boresight gain at $\phi = 0^{\circ}$ is less than $1dB$. Despite the fact that there is a slight discrepancy between the front and rear "ON" state radiation patterns towards the boresight direction, it is noticable that there is a good agreement between the simulation and measurement results for both polarizations. For the completeness of the results the isolation, between two adjacent dipoles oriented in two different polarizations, has been measured and the results shown in Figure 6.28 illustrates that there is a minimum of $-33dB$ isolation over a $100MHz$ band which is sufficient for the use in current and next generation communication systems.

6.6 Summary

A highly directive, pattern reconfigurable antenna with polarization switching capability is presented in this chapter. The use of Fabry Pérot topology which is introduced in previous chapters in combination with the parasitic elements for pattern reconfigurability has been presented. A single planar structure for both radiating structures which are allocated on each side of a dielectric substrate assured a low complexity and a reliable model at a low cost. As described previously the objective of the chapter has been set to achieve a dual polarised model with a good isolation with the alternative one and further increase in the boresight radiation magnitude with "OFF" state as well as minimizing it when the switches are at the "ON" state. The conventional methods of achieving beam steering with bulky structures such as [70] where excessive amount of active components (varicaps) are implemented to the reflecting surface of a cavity type antenna increasing the cost and the complexity. The complexity of a model is directly proportional with the chances of achieving a fault or an error where a considerable amount of time is needed to discover and resolve the issue within the bulky and complicated structure. Within this chapter the evaluated and measured results are substantial where a good correlation between the measurement and simulation results have been achieved. The amount of beam switching attained with only four PIN diodes for the whole structure to attain a boresight gain up to $18.5dBi$ at $\phi = 0^\circ$ as well as an endfire beam switching of $8.1dB$ at an angle of approximately $\phi = 80^\circ$ is achieved where the isolation between alternative polarizations are almost $20dB$ can be stated as a good achievement.

Chapter 7

Conclusion

This chapter will be concentrating on the milestones demonstrated throughout the thesis indicating the achievements including substantial comparison with the relative studies and proposals that has been conducted in the literature. It has been clearly documented in the literature that there have been an enormous amount of study that has been carried out in order to achieve high gain and also pattern reconfiguration where metasurfaces are widely considered due to their planar structures which in turn are used to create cavities generating the famous Fabry Pérot resonance condition. Despite the hard work of antenna and wireless systems engineers to establish robust networks with minimal errors, the real examples show that faults might occur at any stage of the wireless communication system.

There has been a lot of complicated designs introduced by various authors however the time management for the error or fault detection and maintenance have not been considered whilst improving their designs. In this thesis the importance of the usage of time has been considered as an important aspect which is both important for the suppliers and the customers. Therefore less complex systems are targeted for the ease of manufacturing and maintenance where the use of active components that can cause errors regarding to the presence of the high frequency signals have been minimised.

In the first technical chapter (4) of the thesis a continuous beam steering has been targeted where the use of parasitics elements. Regarding to the literature it can be clearly observed that, the similar topology of using parasitic elements were introduced in [22, 26, 29, 30] in order to achieve beam steering however the strip sizes are varied with the aid of PIN diodes in order to behave as a reflector or a director. Regarding the previous models proposed by many authors with different sized parasitic elements, the beam has been switched within couple of degrees attaining a maximum steering angle up to 40° along the H-plane. In spite of the conventional method the idea of maintaining a control over the currents along the parasitic elements have been generated and applied with the use of variable capacitors instead of PINs are proposed in [27]. A peak angle of $\pm 27^{\circ}$ has been achieved according to the symmetry of the proposed design where the lengths of the parasitics were adjusted to behave as directors. On the other hand with the same amount of components (capacitive loads) the proposed design with two sets of parasitic elements with the same lengths of the radiating dipole placed at a distance of $\lambda/2$ and $\lambda/4$ away from the dipole achieved a continuous steering within the angles of $\pm 30^{\circ}$ and $\pm 51^{\circ}$. The gain enhancement towards the intended direction has been achieved with the insertion of a PEC ground planed at the rear end of the radiating structure with a distance of $\lambda/4$. A peak gain of $7.5dBi$ has been achieved with the measurement results conducted in the anechoic chamber.

In order to achieve an improvement on the gain of the proposed structure with a further steering angle freedom, a partially reflecting surface of dipoles has been implemented at a distance of a wavelength away from the PEC ground, introducing a cavity exhibiting the Fabry Pérot anti-resonance condition. A radiating dipole antenna with two parasitic strips were implemented as a source of the cavity with a pattern reconfiguring property by utilizing only two active components of PIN diodes. With the evolved structure a maximum gain of $15.8dBi$ was recorded at the angle of $\theta = 0^{\circ}$. Varying the PIN diode states, beam switching has been observed reducing the boresight gain whilst enhancing the endfire radiation up to $8.6dBi$ with a steering angle of $\theta = 90^{\circ}$ respectively. In comparison with the related publications within the same field, it can be clearly observed that there is a significant

increase at the amount of active devices as well as phase shifters causing a proliferation in the complexity of the design [87] which in turn becomes costly ineffective.

Lastly due to the enormous congestion within the frequency bands which are commonly in use for current wireless communication systems for a degree of freedom within the allocated spectrum where low level of interference can improve the quality of the signals, polarization diversity has been discovered to be applied to the proposed model. There have been various studies about achieving polarization reconfiguration based on a Fabry Pérot model where complex feeding mechanisms as well as the use of excess amount of active components for loading the specially designed partially reflecting surface can be noticed significantly.A high gain, pattern and polarization reconfigurable structure has been proposed recently in [73]. The proposal includes a Fabry Pérot resonance condition to achieve the beam enhancement. As stated previously the reflecting surface has been equipped densely with active components for the reflection phase control of the surface. The maximum beam steering angle is limited with an angle of $\pm 10^{\circ}$ where an $\pm 8^{\circ}$ of steering has also been achieved with different PIN diode states. The peak gain towards the steered angles can be noted as $\approx 8.7 dBi$. However with the proposed design presented in Chapter 6, with the aid of only active components which are PIN diodes with basic biasing circuitry, a directive structure where measured gain reaching up to $18.5 dBi$ with both polarizations have been achieved respectively. An $\pm\theta = 80^{\circ}$ steering angle has been achieved by altering the relative two PIN diode states for different polarizations where a beam switching of $8.1 dB$ has been reported with the "ON" and "OFF" states. In spite sharing a common dielectric substrates it can be revealed that the isolation between the adjacent dipole configurations for different polarizations are approximately $20 dB$. It can be concluded that, a significant improvement has been been achieved with the proposed designs illustrated in this thesis compared to the relative literature. It is obvious that there is certain limitations with the model where the beam is either directed towards the boresight and the endfire directions.However with the aid of only four active elements, among previously proposed models it is clearly an achievement to attain a higher gain and steering angle with a dual polarized pattern reconfigurable antenna.

Chapter 8

Future Work

The summary of the work conducted within the thesis have been explained in the previous section including the areas of novelty and improvements regarding the previously proposed models within the literature. However further work can be conducted in order to improve the specifications broadening the targeted applications. One of the important approaches would be the use of slots as a source in order to achieve further gain enhancement where the configuration of the partially surface design would have a key role. However there could be drawbacks related to the unwanted back radiation as well as attaining the beam steering property due to the strong electromagnetic field within the cavity which would make it difficult to manipulate the pattern with parasitic strips where metallic loops could be an option to be placed at the edges of slots.

Another scope for future improvements would be to further enhance the bandwidth of the structure which could be achieved by generating positive gradients for the reflection phase of the PRS. Previously proposed models have introduced possible methods where inductive and capacitive layers were implemented at either sides of a dielectric in the PRS design and altered the behaviour of the reflection phase resulting with a bandwitdh enhancement. On the other hand matching circuits can be implemented for eliminating the reactive part of the input impedance and enabling a broad bandwidth. However with higher frequencies the presence of RF should be considered at the evaluation stages where unwanted resonances

and interference can be observed.This improvement would be useful for the next generation communication systems in which larger frequency bands might be needed for enhanced data transfers.

On the other hand the effectiveness of the prototype at higher operating frequencies (millimetre wavelength range) can be investigated in order to study the complications that can occur with a more compact model. It is known that the size of the structure decreases with increasing frequency which can give a raise to unwanted coupling and affect the radiating behaviour of the model. The impurities and tolerances have a great impact on the performance of the model especially at the millimetre wave where frequencies within $30GHz - 300GHz$ are considered the behaviour of the components should be examined attentively.

Furthermore, the endfire gain enhancement can be targeted with the inclusion of multiple directive parasitic strips which would be shorter in length where the currents over the strips can be controlled with the aid of PIN diodes. With the "ON" diode states the effect of the parasitics directing the beam towards the endfre direction is targeted which would enhance the distance with the neighbouring antenna.

The elevation angle of the radiation pattern towards the boresight can be adjusted with varying the density of the unit cell forming the partially reflecting surface. Where as pattern reconfigurability along the azimuth plane will still be available. Such improvement could be helpful for link quality especially towards the boresight direction communication with a base transceiver station.

Frequency reconfiguration would be another important field to be considered where modifications to the radiating element can be applied to make it shorter or longer in length using PIN diodes to switch between the frequency bands. The length of parasitic strips should be sectored with the same rate in order to attain pattern reconfigurability at each resonant frequency.

References

[1] J. Bae, Y. S. Choi, J. S. Kim, and M. Y. Chung, "Architecture and Performance Evaluation of MmWave Based 5G Mobile Communication System," *International Conference on Information and Communication Technology Convergence (ICTC)*, pp. 847–851, 2014.

[2] Y. J. Guo and P.-y. Qin, "Advances in Reconfigurable Antennas for Wireless Communications," in *9th European Conference on Antennas and Propagation (EuCAP), Lisbon,*, Lisbon, 2015, pp. 1–4.

[3] C. Cicconetti and P. Marques, "5G radio network architecture - Radio Access and Spectrum (RAS) FP7 Future Network Cluster," *RAS Cluster*, pp. 1–18, 2014.

[4] J. T. Bernhard, *Reconfigurable Antennas*. Morgan & Claypool Publishers, 2007, vol. 2, no. 1.

[5] C. A. Balanis, *Antenna Theory Analysis and Design.*, third edit ed. Hoboken, New Jersey: John Wiley & Sons, 2005.

[6] R. L. Haupt and M. Lanagan, "Reconfigurable antennas," *IEEE Antennas and Propagation Magazine*, vol. 55, no. 1, pp. 49–61, 2013.

[7] H. T. Friis, C. B. Feldman, and W. M. Sharpless, "The Determination of the Direction of Arrival of Short Radio Waves," *Radio Engineers, Proceedings of the Institute of*, vol. 22, no. 1, pp. 47–78, 1934.

[8] J. Ren, X. Yang, J. Yin, and Y. Yin, "A Novel Antenna with Reconfigurable Patterns Using H-Shaped Structures," *IEEE Antennas and Wireless Propagation Letters*, vol. 14, no. 1, pp. 915–918, 2015.

[9] D. Jiawei, L. Yongxiang, and Z. Biao, "A survey on radiation pattern reconfigurable antennas," *7th International Conference on Wireless Communications, Networking and Mobile Computing (WiCOM)*, pp. 1–4, 2011.

[10] Y. Y. Bai, S. Xiao, C. Liu, X. Shuai, and B. Z. Wang, "Design of pattern reconfigurable antennas based on a two - Element dipole array model," *IEEE Transactions on Antennas and Propagation*, vol. 61, no. 9, pp. 4867–4871, 2013.

[11] C. J. Panagamuwa, A. Chauraya, and J. C. Vardaxoglou, "Frequency and beam reconfigurable antenna using photoconducting switches," *IEEE Transactions on Antennas and Propagation*, vol. 54, no. 2, pp. 449–454, 2006.

[12] P. J. B. Clarricoats and H. Zhou, "The design and performance of a reconfigurable mesh reflector antenna," in *1991 Seventh International Conference on Antennas and Propagation, ICAP 91 (IEE)*, 1991, pp. 322–325 vol.1.

[13] P. J. B. Clarricoats, H. Zhou, and A. Monk, "Electronically controlled reconfigurable reflector antenna," in *Antennas and Propagation Society Symposium 1991 Digest*, 1991, pp. 179–181 vol.1.

[14] G. Washington, H.-S. Yoon, M. Angelino, and W. H. Theunissen, "Design, modeling, and optimization of mechanically reconfigurable aperture antennas," *Antennas and Propagation, IEEE Transactions*, vol. 50, no. 5, pp. 628–637, 2002.

[15] D. Sievenpiper, J. Schaffner, J. Lee, and S. Livingston, "A steerable leaky-wave antenna using a tunable impedance ground plane," *IEEE Antennas and Wireless Propagation Letters*, vol. 1, no. 1, pp. 179–182, 2002.

[16] J.-C. Chiao, Y. Fu, I. M. Chio, M. DeLisio, and L.-Y. Lin, "MEMS reconfigurable Vee antenna," *1999 IEEE MTT-S International Microwave Symposium Digest (Cat. No.99CH36282)*, vol. 4, pp. 1515–1518, 1999.

[17] R. Raj, B. Poussot, J. Laheurte, O. Vendier, N. Krismer, D. Silbernagl, M. Malfertheiner, and G. Specht, "Pattern reconfiguration of microstrip antenna using flip-chip mounted packaged MEMS," *Microwave and Optical Technology Letters*, vol. 52, no. 3, pp. 574–577, 2010.

[18] N. H. Chamok, M. H. Yilmaz, H. Arslan, and M. Ali, "High-Gain Pattern Reconfigurable MIMO Antenna Array for Wireless Handheld Terminals," *IEEE Transactions on Antennas and Propagation*, vol. 64, no. 10, pp. 4306–4315, 2016.

[19] Y. Cai and Z. Du, "A novel pattern reconfigurable antenna array for diversity systems," *IEEE Antennas and Wireless Propagation Letters*, vol. 8, pp. 1227–1230, 2009.

[20] J.-S. Row and C.-W. Tsai, "Pattern Reconfigurable Antenna Array With Circular Polarization," *Antennas and Propagation, IEEE Transactions on*, vol. 64, no. 4, pp. 1525–1530, 2016.

[21] Y.-F. Cheng, X. Ding, W. Shao, M.-X. Yu, and B.-Z. Wang, "A Novel Wide-Angle Scanning Phased Array Based on Dual-Mode Pattern-Reconfigurable Elements," *Antennas and Wireless Propagation Letters, IEEE*, vol. 16, pp. 396–399, 2017.

[22] R. Harrington, "Reactively controlled directive arrays," *IEEE Transactions on Antennas and Propagation*, vol. 26, no. 3, pp. 390–395, 1978.

[23] R. Schlub and D. Thiel, "Dual band six element switched parasitic array for smart antenna cellular communications systems," *in Electronics Letters*, vol. 36, no. 16, pp. 1437–1439.

[24] R. Schlub, J. Lu, and T. Ohira, "Seven-Element Ground Skirt Monopole ESPAR Antenna Design From a Genetic Algorithm and the Finite Element Method," *in IEEE Transactions on Antennas and Propagation*, vol. 51, no. 11, pp. 3033–3039.

[25] T. O. Gyoda and K., "Hand-Held Microwave Direction-of-Arrival Finder based on varactor tuned along aerial beamforming," *Microwave Conference*, vol. 2, pp. 585–588, 2001.

[26] S. Zhang, G. H. Huff, J. Feng, and J. T. Bernhard, "A pattern reconfigurable microstrip parasitic array," *IEEE Transactions on Antennas and Propagation*, vol. 52, no. 10, pp. 2773–2776, 2004.

[27] S. Zhang, G. H. Huff, G. Cung, and J. T. Bernhard, "Three Variations of a Pattern Reconfigurable Microstrip Parasitic Array," *Microwave and Optical Technology Letters*, vol. 45, no. 5, pp. 369–372, 2005.

[28] S. L. Preston, D. V. Thiel, J. W. Lu, S. G. O. Keefe, and T. S. Bird, "Electronic beam steering using switched parasitic patch elements," *in Electronics Letters*, vol. 33, no. 1, pp. 7–8.

[29] X. S. Yang, B. Z. Wang, W. Wu, and S. Xiao, "Yagi patch antenna with dual-band and pattern reconfigurable characteristics," *IEEE Antennas and Wireless Propagation Letters*, vol. 6, pp. 168–171, 2007.

[30] X. Yang, B. Wang, S. Xiao, and K. Fung Man, "Frequency and pattern reconfigurable Yagi patch antenna," *Microwave and Optical Technology Letters*, vol. 50, no. 3, pp. 716–719, 2008.

[31] M. Boti, L. Dussopt, and J.-M. Laheurte, "Circularly polarized antenna with switchable polarization sense," *Electronics Letters*, vol. 36, no. 18, pp. 1518–1519, 2000.

[32] F. Yang, S. Member, and Y. Rahmat-Samii, "A reconfigurable patch antenna using switchable slots for circular polarization diversity," *IEEE Microwave and Wireless Components Letters*, vol. 12, no. 3, pp. 96–98, 2002.

[33] F. Yang and Y. Rahmat-Samii, "Patch antennas with switchable slots (PASS) in wireless communications: concepts, designs, and applications," *IEEE Antennas and Propagation Magazine*, vol. 47, no. 2, pp. 13–29, 2005.

[34] Y. J. Sung, T. U. Jang, and Y. Kim, "A reconfigurable microstrip antenna for switchable polarization," *IEEE Microwave and Wireless Components Letters*, vol. 14, no. 11, pp. 534–536, 2004.

[35] H. Zhu, X. Li, Y. Yu, B. Ai, and L. Mattias, "Dual-polarized antenna array for WLANs application," pp. 86–87, 2015.

[36] B. Q. Wu and K.-M. Luk, "A Broadband Dual-Polarized Magneto-Electric Dipole Antenna With Simple Feeds," *Antennas and Wireless Propagation Letters, IEEE*, vol. 8, pp. 60–63, 2009.

[37] S. Genovesi, A. D. Candia, and A. Monorchio, "Compact and low profile frequency agile antenna for multistandard wireless communication systems," *IEEE Transactions on Antennas and Propagation*, vol. 62, no. 3, pp. 1019–1026, 2014.

[38] J. Kiriazi, H. Ghali, H. Ragaie, and H. Haddara, "Reconfigurable dual-band dipole antenna on silicon using series MEMS switches," *IEEE Antennas and Propagation Society International Symposium. Digest. Held in conjunction with: USNC/CNC/URSI North American Radio Sci. Meeting (Cat. No.03CH37450)*, vol. 1, pp. 403–406, 2003.

[39] J. L. Freeman, B. J. Lamberty, and G. S. Andrews, "Optoelectronically Reconfigurable Monopole Antenna," *in Electronics Letters*, vol. 28, no. 16, pp. 1502–1503, 1992.

[40] S. V. Hum and H. Y. Xiong, "Analysis and design of a differentially-fed frequency agile microstrip patch antenna," *IEEE Transactions on Antennas and Propagation*, vol. 58, no. 10, pp. 3122–3130, 2010.

[41] N. Behdad and K. Sarabandi, "A varactor-tuned dual-band slot antenna," *IEEE Transactions on Antennas and Propagation*, vol. 54, no. 2, pp. 401–408, 2006.

[42] ——, "Dual-band reconfigurable antenna with a very wide tunability range," *IEEE Transactions on Antennas and Propagation*, vol. 54, no. 2, pp. 409–416, 2006.

[43] A. Lizasoain, L. F. Tort, M. Garcia, M. Gomez, J. P. Leite, M. P. Miagostovich, J. Cristina, R. Colina, M. Victoria, A. Sarkar, S. Mukherjee, and A. Biswas, "Periodic leaky-wave array antenna on substrate integrated waveguide for gain enhancement," in *2015 IEEE 4th Asia-Pacific Conference on Antennas and Propagation (APCAP)*, vol. 119, no. 3, 2015, pp. 92–93.

[44] A. Dadgarpour, A. A. Kishk, and T. A. Denidni, "Gain enhancement of planar antenna enabled by array of split-ring resonators," *IEEE Transactions on Antennas and Propagation*, vol. 64, no. 8, pp. 3682–3687, 2016.

[45] H. Jiang, Z. Xue, W. Li, and W. Ren, "RCS reduction and gain enhancement for slot antenna array," *2017 IEEE Antennas and Propagation Society International Symposium, Proceedings*, vol. 2017-Janua, no. 5, pp. 2247–2248, 2017.

[46] L. Wang, C. C.-l. Zhao, R. Zhang, X. Chen, G. Fu, and X.-w. X. Shi, "Wideband Circularly Polarized Ellipse Antenna Array with Gain Enhancement," *Int. J. Antennas Propag.*, vol. 2018, 2018.

[47] G. Trentini, "Partially reflecting sheet arrays," *IRE Transactions on Antennas and Propagation*, vol. 4, no. 4, pp. 666–671, 1956.

[48] A. Feresidis and J. Vardaxoglou, "High gain planar antenna using optimised partially reflective surfaces," *IEE Proceedings - Microwaves, Antennas and Propagation*, vol. 148, no. 6, p. 345, 2001.

[49] K. Konstantinidis, A. P. Feresidis, and P. S. Hall, "Multilayer partially reflective surfaces for broadband fabry-perot cavity antennas," *IEEE Transactions on Antennas and Propagation*, vol. 62, no. 7, pp. 3474–3481, 2014.

[50] J. Qi, S. Xiao, and C. Liu, "A partial-reflective-metasurface-based Fabry-Pérot cavity antenna," *2015 International Symposium on Antennas and Propagation (ISAP)*, 2016.

[51] A. P. Feresidis, G. Goussetis, S. Wang, and J. C. Vardaxoglou, "Artificial magnetic conductor surfaces and their application to low-profile high-gain planar antennas," *IEEE Transactions on Antennas and Propagation*, vol. 53, no. 1 I, pp. 209–215, 2005.

[52] J. Qi, S. Xiao, and C. Liu, "A Partial-Reflective-Metasurface-Based Fabry-Pérot Cavity Antenna," *2015 International Symposium on Antennas and Propagation (ISAP)*, pp. 1–3, 2015.

[53] R. Gardelli, M. Albani, and F. Capolino, "Array thinning by using antennas in a Fabry-Perot cavity for gain enhancement," *IEEE Transactions on Antennas and Propagation*, vol. 54, no. 7, pp. 1979–1990, 2006.

[54] A. Refoyo, J. M. Arenas, S. Castillo, M. Avilés, A. P. Feresidis, J. C. Vardaxoglou, and G. K. Palikaras, "Advances in low-profile Fabry-Perot cavity base station antennas using passive periodic surfaces," *Antennas and Propagation in Wireless Communications (APWC), 2011 IEEE-APS Topical Conference on*, vol. 842, pp. 894–897, 2011.

[55] N. Wang, Q. Liu, C. Wu, L. Talbi, Q. Zeng, and J. Xu, "Wideband fabry-perot resonator antenna with two complementary FSS Layers," *IEEE Transactions on Antennas and Propagation*, vol. 62, no. 5, pp. 2463–2471, 2014.

[56] N. Wang, J. Li, G. Wei, L. Talbi, Q. Zeng, and J. Xu, "Wideband Fabry Perot Resonator Antenna With Two Layers of Dielectric Superstrates," *in IEEE Antennas and Wireless Propagation Letters*, vol. 14, pp. 229–232, 2015.

[57] N. Guérin, S. Enoch, G. Tayeb, P. Sabouroux, P. Vincent, and H. Legay, "A metallic Fabry-Perot directive antenna," *IEEE Transactions on Antennas and Propagation*, vol. 54, no. 1, pp. 220–223, 2006.

[58] D. Kim and J. Choi, "Analysis of Antenna Gain Enhancement with a New Planar Metamaterial Superstrate: an Effective Medium and a Fabry-Pérot Resonance Approach," *J. Infrared Milli. Terahz. Waves*, vol. 31, pp. 1289–1303, 2010.

[59] D. Germain, D. Seetharamdoo, S. N. Burokur, and A. De Lustrac, "Thin conformal directive fabry-pérot cavity antenna," *IEEE Antennas and Wireless Propagation Letters*, vol. 12, pp. 926–929, 2013.

[60] K. R. Jha and G. Singh, "Design of highly directive cavity type terahertz antenna for wireless communication," *OPTICS*, vol. 284, no. 20, pp. 4996–5002, 2011.

[61] A. Foroozesh and L. Shafai, "2-D truncated periodic leaky-wave antennas with reactive impedance surface ground planes," *2006 IEEE Antennas and Propagation Society International Symposium*, pp. 15–18, 2006.

[62] D. Kim, J. Ju, and J. Choi, "A broadband Fabry–Pérot cavity antenna designed using an improved resonance prediction method," *Microwave and Optical Technology Letters*, vol. 53, no. 5, pp. 1065–1069, 2011.

[63] Z. M. Razi, P. Rezaei, and A. Valizade, "A novel design of Fabry-Perot antenna using metamaterial superstrate for gain and bandwidth enhancement," *AEUE - International Journal of Electronics and Communications*, vol. 69, no. 10, pp. 1525–1532, 2015.

[64] A. R. Vaidya, R. K. Gupta, S. K. Mishra, and J. Mukherjee, "Effect of superstrate height on gain of MSA fed Fabry Perot Cavity antenna," *LAPC 2011 - 2011 Loughborough Antennas and Propagation Conference*, no. November, pp. 15–18, 2011.

[65] Z.-g. Liu, "Fabry-Perot Resonator Antenna," *Journal of Infrared, Millimeter, and Terahertz Waves*, vol. 4, no. November 2010, pp. 391–403, 2009.

[66] D. Kim, "Enhancement of antenna gain and a bandwidth using frequency selective reflectors," in *9th European Conference on Antennas and Propagation (EuCAP), Lisbon*, 2015, pp. 1–4.

[67] D. Kim and E. Kim, "A High-Gain Wideband Antenna With Frequency Selective Side Reflectors Operating in an Anti-Resonant Mode," *in IEEE Antennas and Wireless Propagation Letters*, vol. 14, pp. 442–445, 2015.

[68] F. Qin, S. Gao, C. Mao, G. Wei, J. Xu, and J. Li, "Low-profile high-gain tilted-beam Fabry-Perot antenna," *2015 9th European Conference on, Antennas and Propagation (EuCAP)*, pp. 1–5, 2015.

[69] H. Nakano, S. Mitsui, and J. Yamauchi, "Tilted-beam high gain antenna system composed of a patch antenna and periodically arrayed loops," *IEEE Transactions on Antennas and Propagation*, vol. 62, no. 6, pp. 2917–2925, 2014.

[70] A. Ourir, S. N. Burokur, and A. de Lustrac, "Electronic Beam Steering of an Active Metamaterial-Based Directive Subwavelength Cavity," in *The Second European Conference on Antennas and Propagation, EuCAP 2007*, vol. 0, 2007, pp. 1–4.

[71] Y. J. Guo, L. Y. Ji, P. Y. Qin, and S. X. Gong, "A Reconfigurable Partially Reflective Surface (PRS) Antenna for Beam Steering," *IEEE Transactions on Antennas and Propagation*, vol. 63, no. September 2016, 2015.

[72] P. Xie, G. Wang, T. Cai, H. Li, and J. Liang, "Novel fabry-pérot cavity antenna with enhanced beam steering property using reconfigurable meta-surface," *Materials Science & Processing*, vol. 123, no. 7, pp. 1–6, 2017.

[73] P. Xie, G. Wang, H. Li, and J. Liang, "A Dual-Polarized Two-Dimensional Beam-Steering Fabry–Pérot Cavity Antenna With a Reconfigurable Partially Reflecting Surface," *IEEE Antennas and Wireless Propagation Letters*, vol. 16, pp. 2370–2374, 2017.

[74] W. M.-b. Beamwidth, T. Debogovi, J. Bartoli, S. Member, T. Debogovic, J. Bartolic, and J. Perruisseau-Carrier, "Dual-Polarized Partially Reflective Surface Antenna With MEMS-Based Beamwidth Reconfiguration," *Antennas and Propagation, IEEE Transactions on*, vol. 62, no. 1, pp. 228–236, 2014.

[75] M. Wang, Q. Ye, W. Wu, and D. G. Fang, "A dual-polarized Fabry-Perot resonator antenna," in *Antennas and Propagation (APCAP), 2012 IEEE Asia-Pacific Conference on*. IEEE, aug 2012, pp. 31–32.

[76] B. A. Zeb and K. P. Esselle, "High-gain dual-band dual-polarised electromagnetic band gap resonator antenna with an all-dielectric superstructure," *IET Microwaves Antennas & Propagation*, vol. 9, no. 10, pp. 1059–1065, 2015.

[77] F. Qin, S. Gao, G. Wei, Q. Luo, and J. Xu, "Array-fed dual-polarized wideband fabry–perot antenna based on metasurface," *Microwave and Optical Technology Letters*, vol. 58, no. 10, pp. 2316–2321, 2016.

[78] R. J. Weber, *Introduction to microwave circuits : radio frequency and design applications [electronic resource]*, John Wiley & Sons and IEEE Xplore (Online service) et. al, Eds. Wiley IEEE Press Imprint, 2015, 2015.

[79] T. Weiland, M. Timm, and I. Munteanu, "A practical guide to 3-D simulation," *IEEE Microwave Magazine*, vol. 9, no. 6, pp. 62–75, 2008.

[80] P. G. Huray, "Static Electric Fields," in *Maxwell's Equations*. Wiley-IEEE Press, 2010, p. 275.

[81] M. Kanesan, D. V. Thiel, and S. O. Keefe, "A Robust Method of Calculating the Effective Length of a Conductive Strip on an Ungrounded Dielectric Substrate," *Progress In Electromagnetics Research M*, vol. 35, no. December 2013, pp. 57–66, 2014.

[82] M. G. Vigueras, J. R. Mosig, F. Mesa, R. R. Berral, F. Medina, and M. Garcia Vigueras, "Closed-form expressions for modeling diffraction at printed dipole-based FSS," *Microwave, Antenna, Propagation and EMC Technologies for Wireless Communications (MAPE), 2013 IEEE 5th International Symposium on*, no. 1, pp. 275–278, 2013.

[83] B. B. A. Munk, *Frequency selective surfaces : theory and design*. New York: New York : John Wiley, c2000, 2000.

[84] S. A. Kuznetsov, A. G. Paulish, M. Navarro-Ciá, and A. V. Arzhannikov, "Selective Pyroelectric Detection of Millimetre Waves Using Ultra-Thin Metasurface Absorbers," *Scientific Reports*, vol. 6, no. October 2015, pp. 1–11, 2016.

[85] S. B. Savia and E. Parker, "Equivalent circuit model for superdense linear dipole FSS," *IEE Proc.-Microw. Antennas Propag.*, vol. 150, no. 1, pp. 37–42, 2003.

[86] S. P. I. N. Diode, "Infenion Technologies BAR64," 2013.

[87] A. Ourir, S. N. Burokur, R. Yahiaoui, and A. de Lustrac, "Directive metamaterial-based subwavelength resonant cavity antennas – Applications for beam steering," *Comptes Rendus Physique*, vol. 10, no. 5, pp. 414–422, 2009.

[88] D. Sievenpiper, J. Schaffner, R. Loo, G. Tangonan, S. Ontiveros, and R. Harold, "A tunable impedance surface performing as a reconfigurable beam steering reflector," *IEEE Transactions on Antennas and Propagation*, vol. 50, no. 3, pp. 384–390, 2002.

[89] G. Ancans, V. Bobrovs, A. Ancans, and D. Kalibatiene, "Spectrum Considerations for 5G Mobile Communication Systems," *Procedia Computer Science*, vol. 104, pp. 509–516, 2016.

[90] F. Costa, A. Monorchio, and G. Manara, "An overview of equivalent circuit modeling techniques of frequency selective surfaces and metasurfaces," *Appl. Comput. Electromagn. Soc. J.*, vol. 29, no. 12, pp. 960–976, 2014.

[91] C. Lee and R. Langley, "Equivalent-circuit models for frequency-selective surfaces at oblique angles of incidence," *IEE Proceedings H Microwaves, Antennas and Propagation*, vol. 132, no. 6, p. 395, 1985.

[92] F. Costa, A. Monorchio, and G. Manara, "Efficient Analysis of Frequency-Selective Surfaces by a Simple Equivalent-Circuit Model," *Appl. Comput. Electromagn. Soc. J.*, vol. 54, no. 4, pp. 35–48, 2012.

[93] O. Luukkonen, C. Simovski, G. Granet, G. Goussetis, D. Lioubtchenko, A. V. Räisänen, and S. A. Tretyakov, "Simple and accurate analytical model of planar grids and high-impedance surfaces comprising metal strips or patches," *IEEE Transactions on Antennas and Propagation*, vol. 56, no. 6, pp. 1624–1632, 2008.